Recherche d'une violation de l'invariance sous le renversement du temps dans la désintégration du neutron

P. Gorel

Université de CAEN/BASSE NORMANDIE

UFR : **Science**

Ecole Doctorale : **SIMEM**

THESE
présenté par

Pierre GOREL

soutenue le

16 juin 2006

en vue de l'obtention du

Doctorat de l'UNIVERSITE DE CAEN
Spécialité : Consituants élémentaires

Arrêté du 25 avril 2002

Recherche d'une Violation de l'Invariance sous le Renversement du Temps dans la Désintégration du Neutron

Membres du JURY

M.	Kazimierz	Bodek	Professeur	Université Jagellon	Cracovie (Pologne)	(Rapporteur)
M.	Klaus	Kirch	Chercheur	PSI	Villigen (Suisse)	(Rapporteur)
M.	Roman	Kossakowski	Professeur	Université de Savoie	Annecy	
M.	Christian	Plonka	Chercheur	ILL	Grenoble	
M.	Dominique	Durand	DR CNRS	LPC	Caen	
M.	Oscar	Naviliat-Cuncic	Professeur	LPC	Caen	(directeur de Thèse)

Celui qui vit sans folie n'est pas si sage qu'il croit.
Proverbe chinois.

Remerciements

C'est un exercice difficile que celui auquel il me faut me livrer ici. Nombreuses sont les personnes qu'il me faut remercier, et j'ai peur d'en oublier.

Je tiens tout d'abord à remercier M. le directeur de l'Institut Paul Scherrer, R. Eichler, de m'avoir accueilli pendant un an et demi au sein de son centre de recherche, ainsi que MM. Jean-François Lecolley et Jean-Claude Steckmeyer, les directeurs successifs du Laboratoire de Physique Corpusculaire de Caen, où j'ai terminé cette thèse.

Merci également à Klaus Kirch pour les différents rôles qu'il a joué dans ma thèse : entre l'encadrement pendant mon séjour à PSI et son rôle de rapporteur, son aide et ses conseils m'ont été très précieux.

Il me faut également remercier Kazimierz Bodek, mon second rapporteur et le porte-parole de notre collaboration. Bien que nous ayons parfois été en désaccord, il m'a permis d'effectuer mon travail dans de bonnes conditions, notamment en me permettant de travailler trois mois à l'université Jagellon avec les autres membres la collaboration.

Merci à Oscar Naviliat-Cuncic, mon directeur de thèse, pour avoir encadré ma personne pendant près de quatre années. Les discussions que nous avons eu ont toujours été très constructives et j'ai pris beaucoup de plaisir (partagé je crois) à travailler avec lui.

Je veux également remercier Roman Kossakowski, Dominique Durand et Christian Plonka de bien avoir voulu faire partie de mon jury de thèse.

Ma gratitude va également à tous les membres de la collaboration nTRV avec qui ce fut un plaisir de travailler. Une mention spéciale à Adam Kozela et Jacek Pulut qui étaient à mes côtés au PSI. Je garderai longtemps le souvenir des parties d'"office-soccer" qui ont contribué à la bonne ambiance qui a régné.

Il ne faut pas que j'oublie mes "room-mates" de Brugg : Tomek et Peter, également thésards au PSI avec qui j'ai vécu une année et demi très agréable. Je regrette beaucoup la raclette au alentours de minuit, les excursions ski à Grindelwald ainsi que les discussions politiques.

Merci aux padawans du LPC : Alain, Anne-Marie, Benoit, Beyhan, Caroline, François, Gwendal, Hicham, Jeremy et Yves. Si une bonne ambiance règne au sein du labo, c'est en partie grâce à eux et aux pauses cafés entre thésards. Mes demoiselles, mes damoiseaux, je vous souhaites à toutes et à tous beaucoup de courage et une bonne continuation.

Puisque nous sommes dans les remerciements pour le LPC, je souhaite parler de Thomas Lefort et Xavier Fléchart. Le premier a partagé mon bureau pendant plus deux ans pour son malheur/bonheur (rayer la mention inutile), et le second occupait le bureau d'en face. Tous deux m'ont beaucoup aidé au fil de mon travail et je leur en suis reconnaissant. (Message personnel pour Xavier : "courage, un jour tu seras meilleur que moi !"). Je n'oublie par non plus Marc : s'il n'a pas joué un très grand rôle pour ma thèse elle même, j'ai pris un grand plaisir à grimper avec lui et il ne m'a jamais laissé tomber.

Mention spéciale (encore) pour Gilles Ban, celui par qui tout est arrivé : professeur à l'ENSICAEN, c'est lui qui ma proposé pour cette thèse. Malgré son côté peu sérieux, il fût un guide précieux pendant toutes ces années.

Gilles Iltis a été l'artisan de la fabrication des feuilles de Plomb utilisées dans notre expérience et j'ai eu beaucoup de plaisir à travailler avec lui. Je le remercie donc pour sa grande disponibilité et son amabilité.

Je suis reconnaissant en règle générale à toutes les personnes du LPC. Bien que peu d'entre elles aient réellement travaillé avec moi, elles m'ont pour beaucoup aidé à un moment ou l'autre de ma thèse. L'administration, par exemple, pour tous les paperasses diverses et variées. Merci donc à Michelle, Aurélie, Catherine et Eveline. La bibliothèque : vu la quantité papier que j'emmène en partant, j'ai beaucoup sollicité Sandrine qui a toujours répondu à mes demandes dans les plus bref délais. Le service informatique enfin : Lolo, Pimprenelle, Zwo et Thierry. Je fus, je pense, plutôt exigeant avec eux mais ils ont toujours été disponibles ; surtout pour des séances de "formation TCP/IP". Et puisque je suis dans l'informatique, j'en profite pour exprimer ma gratitude à "Momo le Hacheur" (il se reconnaîtra) pour les conseils avisés concernant l'utilisation de ROOT.

Enfin, merci également à mes parents, pour m'avoir toujours soutenu, et à Aleksandra (Kocham Ciebie). Merci aussi à mes amis, toujours présents pour me soutenir : Phuc, Nico, Zoboton, Naneuk, Tenia, Dodo,... (La liste est longue et j'ai peur d'en oublier).

Abstract

One of the unsolved fundamental questions in physics is why the universe is made mainly of matter. If the physical laws were symmetric for matter and anti-matter, the Big-Bang should have produced equal amounts of matter and anti-matter; followed by a total annihilation. In other words, protons should have cancelled with anti-protons, electrons with positrons, neutrons with anti-neutrons, and so on for all elementary particles. The result would have been a sea of photons in the universe without any matter left. Another possibility would be the separation, somehow mysterious, of matter and anti-matter in both parts completely separated, that is, the existence of a "symmetric" universe completely made of anti-matter. So far, no proof of the existence of such universe has been observed.

In 1967, Sakharov proposed few conditions to obtain the matter-antimatter asymmetry; amongst them the violation of the C- and CP-invariances within baryogenesis. While the CP-violation observed in the decay of K and B mesons is already implemented in the Standard Model with the Cabibbo-Kobayashi-Maskawa mixing matrix, its effect in the baryogenesis is too weak by several orders of magnitude to explain the observed matter asymmetry.

Since the effect of the mixing matrix in processes involving only u and d quarks is very small and in fact beyond the accuracy reachable by the present generation of experiments, the determination of CP-violating correlations in β-decay provides a large window to search for *Physic beyond the Standard Model*. So far no violation of the CPT invariance has been discovered and it can be assumed that CP- and T- invariance violation are equivalent.

In nuclear β-decay, it is possible to study several correlations to probe the violation of T-symmetry, especially the one related to the parameter R: the triple product between the decaying nucleon spin, the electron momentum and the electron spin. Since time reversal inverts the sign of velocities, this triple product changes its sign under this transformation. Therefore, after correction due to final-state interaction, this parameter is expected to be zero if time reversal invariance holds.

The experiment described in this document is dedicated to the measurement of this parameter in the neutron decay, together with the parameter N. The latter is related to the angular correlation between the neutron spin and the electron spin, and it is not T-violating. It will be used as an internal sensitivity monitor. These two parameters are determined using the transverse component of the electron polarization. The parameter R is sensitive to the component perpendicular to the plane defined by the neutron polarization and the electron momentum, whereas N is sensitive to the one along the neutron polarization.

The measurement was performed using the polarized cold neutrons beam delivered at the FUNSPIN beamline at the spallation source SINQ (Paul Scherrer Institute, Vil-

ligen, Switzerland). Neutrons decay in-flight and the electron transverse polarization is measured using a Mott polarimeter placed on both sides of the neutron beam.

The work made during this thesis can be divided in two parts. The first one, realized at the Paul Scherrer Institute (PSI), consisted in the improvement and optimization of the experimental setup, followed by the participation in two runs (2003 and 2004). The second part was not as well geographically localized as the first one since it took place at the Laboratoire de Physique Corpusculaire in Caen, at the PSI and at the Uniwersytet Jagielloński in Krakow. It consisted in the analysis of the data gathered in 2004.

When my work begun, in september 2002, a simplified prototype of the detector had been tested. It consisted of a light beam volume structure, a large ($500 \times 500\ mm^2$ active area) MultiWire Proportional Chamber and the associated scintillator wall. The results were mixed: contrary to the MWPC, the hodoscope did not give satisfactory results. Indeed, the photomultipliers showed a high sensitivity to the magnetic field used to guide the neutron spin and the signal amplitude was strongly dependent on the place where the light was emitted in the scintillators. After a careful study of these effects, two new hodoscopes were designed and built at the beginning of 2003. Meanwhile, the polarization of the neutron beam was measured to be in average $P = (89.75 \pm 1.0)\%$ with a maximum of $P = (95.25 \pm 0.04)\%$ around the center of the beam. The missing parts of the detector were constructed at the same time, amongst them the second multiwire chamber and the lead foils used as a Mott polarimeter target. In fall 2003, a commissionning run was performed, despite the fact that the device created to manipulate the calibration source was not yet ready. This run was globaly satisfactory. A few imperfections were discovered and analyzed; and some improvements were made before the data taking run performed in summer 2004: three months of acquisition supposed to give a precision of 1% in the measurement of R.

For the second part of the work I was involved in the data analysis using C++ software based on the ROOT class collections developed at CERN. It led to the elaboration of a method for the extraction of the parameters R and N from the million of interesting events recorded. Additionally, a thorough study of the background origin was provided, leading to suggestions of improvements for the next scheduled run, in 2006.

Contents

Première partie

En bref, dans la langue de Molière...

Chapitre 1

Motivations

1.1 Symétries et Univers

Selon la théorie actuelle du Big-Bang, l'univers se serait formé à partir d'énergie. Une symétrie parfaite des lois physiques aurait eu pour conséquence la création de matière et d'antimatière en quantités égales. Cependant, l'antimatière qui devrait faire pendant à notre existence n'a pour le moment pas été détecté. Il semble donc que les symétries des lois physiques doivent être remises en question.

Laporte introduisit en 1924 la notion de Parité : il classa les atomes selon la parité de leur fonction d'onde : paire (parité +1) ou impaire (parité −1). Il découvrit alors que si un atome se désexcite en émettant un photon, sa parité s'inverse. Le photon ayant une parité −1, la parité totale du système est alors conservée. Wigner démontra en 1927 que cette loi empirique était la conséquence de la symétrie gauche-droite des forces électromagnétiques, appelée symétrie P. Trois transformations discrètes furent alors développées : la parité (P) qui inverse les coordonnées de l'espace, la conjugaison de charge (C) qui transforme la matière en antimatière et vice-versa, et le renversement du temps (T). Des lois de symétries leur furent alors associées.

En 1949, deux nouvelles particules furent découverte par Powell dans les rayonnements cosmiques : les mésons θ et τ, se désintégrant respectivement en deux et trois pions. Les mesures de temps de vie et de masse donnèrent des résultats identiques pour les deux types de particules. On aurait donc déduit qu'elles étaient identiques si leur parité n'avait été différente[1].On parla de "l'énigme θ-τ".

Ce problème fut résolu en 1956 lorsque Lee and Yang découvrirent qu'aucune expérience ne démontrait la conservation de P dans le cadre de la désintégration β. Ils proposèrent alors plusieurs expériences dédiées à ce problème. La violation de la parité dans la désintégration β du Co^{60} fut établie par Wu *et al.*. Il fut démontré l'année suivante que cette expérience mettait également en évidence la violation de la symétrie C, c'est à dire une différence de comportement entre la matière et l'antimatière dans la désintégration β.

En 1964, l'étude de la désintégration des mésons K^0 mis en évidence la violation de la symétrie CP. Trois ans plus tard, Sakharov proposa plusieurs conditions nécessaires pour obtenir l'asymétrie matière-antimatière observée dans la genèse de l'univers, parmi

[1]Le pion a une parité -1 ; la conservation de la parité conduit à une parité +1 pour le θ et -1 pour le τ

lesquelles la violation de la symétrie CP. A l'heure actuelle, celle-ci a été établie pour deux processus : la désintégration des mésons K et B. Leurs effets dans la baryogénèse sont de plusieurs ordres de grandeur trop faibles par rapport aux conditions de Sakharov.

1.2 Le Modèle Standard

Le modèle standard (MS) est le cadre théorique actuel de la physique des particules. Son élaboration débuta dans les années 70. Il regroupe trois des quatre interactions fondamentales (Tab.1.1) : l'interaction forte (cohésion des noyaux), l'interaction faible (responsable de la désintégration β) et l'interaction électromagnétique.

Interaction	Amplitude relative	Portée
Force nucléaire forte	10^{40}	$1.4 \times 10^{-15} m$
Force électromagnétique	10^{38}	∞
Force nucléaire faible	10^{15}	$10^{-18} m$
Gravité	10^{0}	∞

Tab. 1.1: Interactions fondamentales

L'une des principales hypothèses du MS est le théorème CPT : un processus est invariant si on inverse simultanément les charges (C), les coordonnées spatiales (P) et le temps (T). A l'heure actuelle, ce théorème n'a jamais été mis en défaut et il est possible d'assimiler les violations de symétrie CP et T.

Deux sources de violation de CP ont été incorporées au MS. D'une part, la matrice de mélange de Cabbibo-Kobayashi-Maskawa (CKM) pour l'interaction faible, et d'autre part le terme θ dans le lagrangien de la chromodynamique quantique pour l'interaction forte. A l'heure actuelle, seule la matrice CKM possède un prolongement expérimental puisqu'elle rend compte de la violation de CP dans la désintégration des mésons K et B. Le terme θ est contraint par la mesure de la valeur du moment électrique dipolaire du neutron.

Plusieurs extensions du modèle standard permettant d'introduire des nouvelles sources de violation de la symétrie CP sont à l'étude.

1.3 Désintégration β du neutron et violation de la symétrie T

Le neutron a un temps de vie de 886 s : la transformation d'un quark d en quark u provoque l'émission d'un boson W^- qui se désintègre très vite en un électron et un anti-neutrino (Fig. 1.1).

L'effet de la matrice CKM sur des systèmes formés de quarks légers (u et d) est trop faible pour être détecté par la dernière génération de détecteurs. La mise en évidence d'une violation de la symétrie T dans la désintégration du neutron serait la preuve d'une physique *au delà du Modèle Standard*.

Nous considérons quatre observables (Fig. 1.2) :

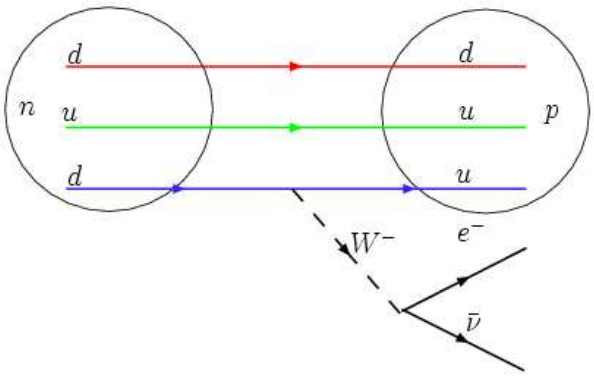

Fig. 1.1: Diagramme de la désintégration β du neutron.

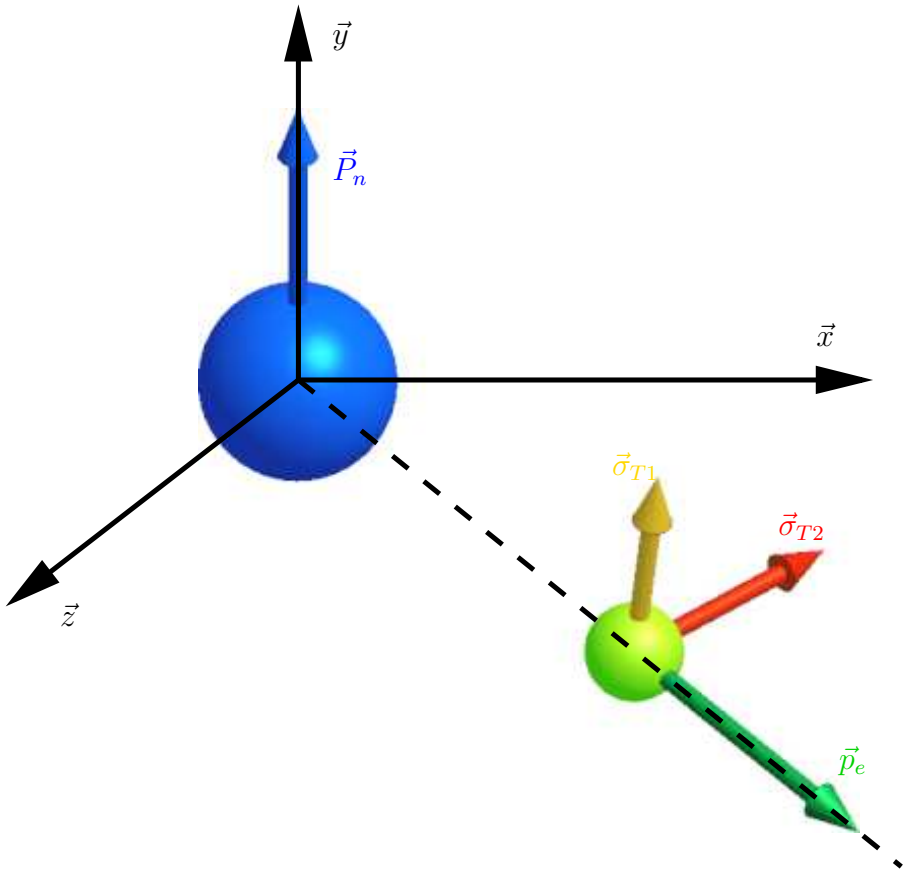

Fig. 1.2: Désintégration du neutron : observables utilisée par l'expérience nTRV.

- La polarisation des neutrons $\vec{P}_n$.
- L'impulsion des électrons $\vec{p}_e$.
- La polarisation transversale des électrons selon le plan formé par la polarisation des neutrons et l'impulsion des électrons $\vec{\sigma}_{T1}$.
- La polarisation des électrons selon une direction perpendiculaire à ce plan $\vec{\sigma}_{T2}$.

Ces observables étant liés à des vitesses[2], elles sont inversées par le renversement du temps. Comme nous pouvons le voir sur la Fig. 1.3, le système après renversement du temps n'est identique au système initial que si $\vec{\sigma}_{T2} = 0$.

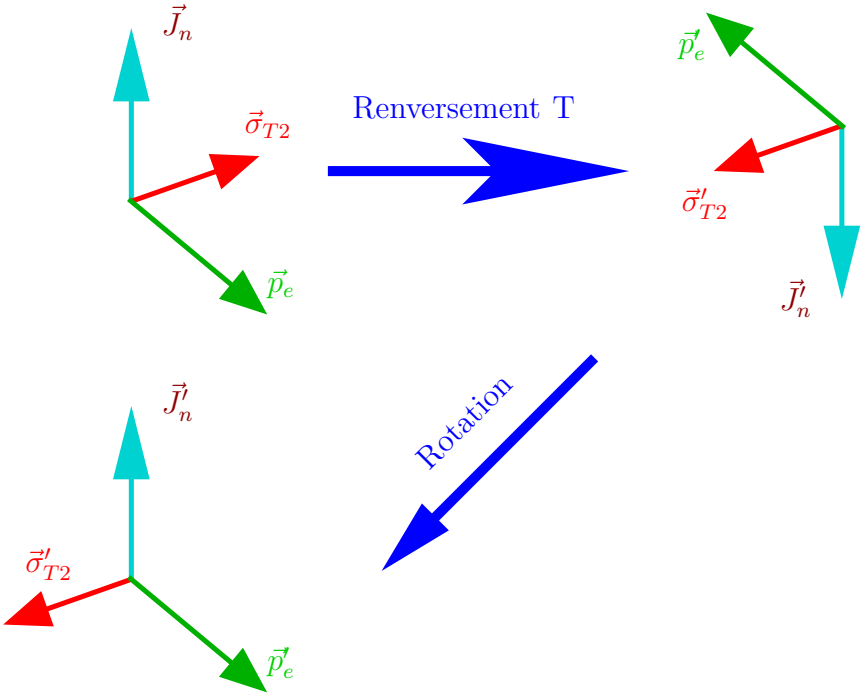

Fig. 1.3: Effet du renversement du temps sur les observables

Si les électrons sont polarisés selon la direction perpendiculaire à leur impulsion et à la direction de polarisation des neutrons, il y a alors violation de la symétrie par renversement du temps dans la décroissance du neutron.

1.4 Théorie sous-jacente : les paramètres R et N

En 1957, Jackson, Treiman et Wyld ont poursuivi les travaux de Lee et Yang en étudiant la violation de la symétrie sous renversement du temps. Ils ont alors paramétrisé l'influence des corrélations angulaires entre les différentes observables de la désintégration β. Dans le cas de noyaux orientés et d'une expérience sensible à la polarisation des électrons, le taux de désintégration est :

$$\begin{aligned}\omega(\vec{P}_n, \vec{\sigma}|E_e, \Omega_e)dE_e d\Omega_e = \frac{F(\pm Z, E_e)}{(2\pi)^4} p_e E_e (E_0 - E_e)^2 dE_e d\Omega_e \\ \times\xi\left\{1 + b\frac{m}{E_e} + \frac{\vec{p}_e}{E_e}\cdot\left(A\vec{P}_n + G\vec{\sigma}\right)\right. \\ \left. +\vec{\sigma}\cdot\left[\boldsymbol{N}\vec{P}_n + Q\frac{\vec{p}_e}{E_e+m}\left(\vec{P}_n\cdot\frac{\vec{p}_e}{E_e}\right) + \boldsymbol{R}\vec{P}_n\times\frac{\vec{p}_e}{E_e}\right]\right\}\end{aligned} \tag{1.1}$$

[2]La polarisation caractérise la façon dont sont disposés les spins des particules individuelles. Classiquement, le spin peut être assimilé à une vitesse de rotation

où $\langle\vec{J}\rangle/J$ est la polarisation des noyaux ; m, $\vec{p}_e$ et E_e sont respectivement la masse, l'impulsion et l'énergie de l'électron émis, et Z la charge du noyau de recul. $\vec{\sigma}$ peut être un vecteur unitaire, auquel cas l'Eq. 1.1 donne la probabilité d'émettre des électrons dont le spin est dans la direction $\vec{\sigma}$. La polarisation des électrons selon $\vec{\sigma}$, émis dans la direction $\vec{p}_e$, est alors

$$P(\vec{\sigma}) = \frac{\omega(\vec{\sigma}|\ldots) - \omega(-\vec{\sigma}|\ldots)}{\omega(\vec{\sigma}|\ldots) + \omega(-\vec{\sigma}|\ldots)} \tag{1.2}$$

D'autres observables telles l'impulsion du noyau de recul ou l'impulsion du neutrino n'apparaissent pas dans cette équation : le système expérimental n'y est pas sensible et leur influence est moyennée.

La polarisation des électrons selon $\langle\vec{J}\rangle$ est donc directement proportionnelle au paramètre N. De même, le paramètre R est lié à la polarisation des électrons selon la direction perpendiculaire à $\langle\vec{J}\rangle$ et à $\vec{p}_e$. Si R est non nul, le terme associé est maximal dans le cas où $\langle\vec{J}\rangle$ et à $\vec{p}_e$ sont perpendiculaires : le triple produit est maximum dans cette configuration.

Que ce passe-t-il au niveau de l'Eq. 1.1 si le temps est renversé ? Les vitesses sont transformées en leur opposé. Nous obtenons donc :

$$\begin{aligned}\omega'(\vec{P}_n, \vec{\sigma}|E_e, \Omega_e)dE_e d\Omega_e = \frac{F(\pm Z, E_e)}{(2\pi)^4} p_e E_e (E_0 - E_e)^2 dE_e d\Omega_e \\ \times\xi\left\{1 + b\frac{m}{E_e} + \frac{\vec{p}_e}{E_e}\cdot\left(A\vec{P}_n + G\vec{\sigma}\right)\right. \\ \left. +\vec{\sigma}\cdot\left[R\vec{P}_n + Q\frac{\vec{p}_e}{E_e+m}\left(\vec{P}_n\cdot\frac{\vec{p}_e}{E_e}\right) - R\vec{P}_n\times\frac{\vec{p}_e}{E_e}\right]\right\}\end{aligned} \tag{1.3}$$

Seule la contribution liée au paramètre R est modifiée, une valeur non nulle de R signifie donc une violation de la symétrie sous le renversement du temps, ce qui est cohérent avec l'explication qualitative donnée précédemment.

Le but final de l'expérience décrite ici est de déterminer les valeurs de R et de N dans le cas du neutron avec une précision attendue de 0,5 % sur le paramètre R.

Chapitre 2

Principes de la mesure

Quatre observables doivent donc être mesurées simultanément (Fig. 1.3) :
- La polarisation des neutrons $\vec{P}_n$.
- L'impulsion des électrons $\vec{p}_e$.
- La polarisation transversale des électrons selon le plan formé par la polarisation des neutrons et l'impulsion des électrons $\vec{\sigma}_{T1}$.
- La polarisation des électrons selon une direction perpendiculaire à ce plan $\vec{\sigma}_{T2}$.

2.1 Mesure de la polarisation des neutrons

Il est possible d'employer deux méthodes pour mesurer la polarisation du faisceau de neutron. La première utilise un polarimètre à super-miroirs et la deuxième se sert de l'anisotropie de l'émission d'électrons par un faisceau de neutrons polarisés.

2.1.1 Mesure directe en utilisant un polarimètre

2.1.1.1 Principe des super-miroirs

Lorsqu'un neutron entre en contact avec un matériau, il est réfléchi si sa vitesse perpendiculaire est inférieure à un seuil dépendant du matériau. Dans le cas de super-miroirs, les matériaux utilisés ont des seuils élevés. Les neutrons froids, ayant par définition une vitesse faible, ont donc une probabilité élevée d'être complètement réfléchis.

Le polarimètre utilise des super-miroirs ferromagnétiques. Le processus de réflexion fait alors intervenir à la fois une composante nucléaire et une composante magnétique dont le signe dépend de l'orientation du spin du neutron. Il est donc possible de choisir les matériaux de telle sorte que les deux composantes se compensent pour un état de spin. Les neutrons dans cet état traversent donc le super-miroir tandis que ceux dans l'état inverse sont réfléchis.

2.1.1.2 Mesure de la polarisation

Cette méthode nécessite l'utilisation du dispositif décrit par la Fig. 2.1. Le système d'analyse est formé de deux super-miroirs A1 et A2 reliés par un guide de neutron où est installé un inverseur de spin F2. Un autre inverseur de spin (F1) est placé en bout de la ligne de neutron, avant le dispositif d'analyse. Deux inverseurs additionnels, F1' et F2',

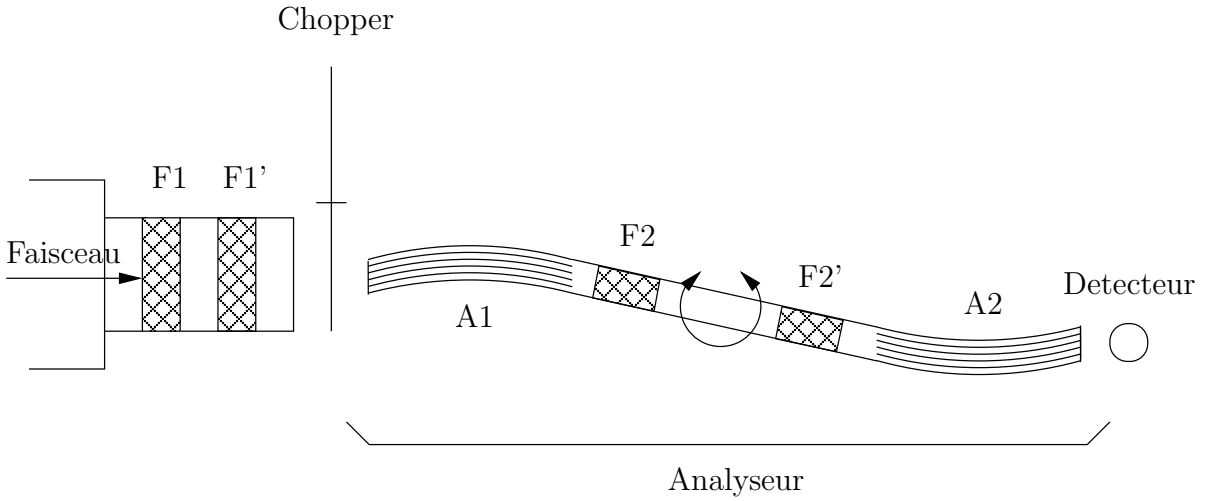

Fig. 2.1: Vue schématique du dispositif de mesure de la polarisation. Les inverseurs de spin F1 et F1' font partie intégrante de la ligne de neutrons polarisés. Le dispositif d'analyse contient deux super-miroirs et deux inverseurs de spin. Il peut être retourné de façon à inverser la séquence A1-F2-F2'-A2. Le détecteur permet de connaître le nombre de neutron traversant le polarimètre.

permettent la détermination de leurs efficacités respectives f1, f1', f2 et f2'. Le dispositif d'analyse peut être retourné, inversant ainsi la séquence A1-F2-F2'-A2.

Le protocole de mesure consiste à mesurer des spectres de temps de vol des neutrons $N_{F_1F_2}^{F_1'F_2'}$, pour 9 états des inverseurs de spins : N_{00}^{00}, N_{10}^{00}, N_{01}^{00}, N_{00}^{10}, N_{00}^{01}, N_{11}^{00}, N_{00}^{11}, N_{10}^{10} et N_{01}^{01} ("0" et "1" indique ici l'état, inactif ou actif, de l'inverseur de spin correspondant). Ces spectres sont collectés pour chaque position, normale ou inversée, du dispositif d'analyse ; notées $N_{F_1F_2}^{F_1'F_2'}$ et $\tilde{N}_{F_1F_2}^{F_1'F_2'}$ respectivement.

Les efficacités des inverseurs de spin sont alors déterminées par :

$$\begin{aligned} f_1 &= \frac{N_{10}^{10} - N_{10}^{00}}{N_{00}^{00} - N_{00}^{10}} \qquad & f_1' &= \frac{N_{10}^{10} - N_{00}^{10}}{N_{00}^{00} - N_{10}^{00}} \\ f_2 &= \frac{N_{01}^{01} - N_{01}^{00}}{N_{00}^{00} - N_{00}^{01}} \qquad & f_2' &= \frac{N_{01}^{01} - N_{00}^{01}}{N_{00}^{00} - N_{01}^{00}} \end{aligned} \tag{2.1}$$

La polarisation du faisceau de neutrons peut être déterminée en utilisant uniquement une paire d'inverseurs de spin F1/F2 ou F1'/F2'. Ainsi, avec F1 et F2 simultanément, nous avons quatre grandeurs indépendantes pour chaque position de l'analyseur : normale

$$\begin{aligned} N_{++} &= (N_{00}f_1f_2 + N_{10}f_2) + (N_{01}f_1 + N_{11}) \\ N_{+-} &= (N_{00}f_1 + N_{10}) - (N_{01}f_1 + N_{11}) \\ N_{-+} &= (N_{00}f_2 - N_{10}f_2) + (N_{01} - N_{11}) \\ N_{--} &= (N_{00} - N_{10}) - (N_{01}f1 - N_{11}) \end{aligned} \tag{2.2}$$

et inversée

$$\begin{aligned} \tilde{N}_{++} &= (\tilde{N}_{00}f_1f_2 + \tilde{N}_{10}f_2) + (\tilde{N}_{01}f_1 + \tilde{N}_{11}) \\ \tilde{N}_{+-} &= (\tilde{N}_{00}f_1 + \tilde{N}_{10}) - (\tilde{N}_{01}f_1 + \tilde{N}_{11}) \\ \tilde{N}_{-+} &= (\tilde{N}_{00}f_2 - \tilde{N}_{10}f_2) + (\tilde{N}_{01} - \tilde{N}_{11}) \\ \tilde{N}_{--} &= (\tilde{N}_{00} - \tilde{N}_{10}) - (\tilde{N}_{01}f1 - \tilde{N}_{11}) \end{aligned} \tag{2.3}$$

La polarisation du faisceau est alors donnée par le super-rapport :

$$P = \left[\frac{N_{-+}^2}{N_{++}N_{+-}} \cdot \frac{\tilde{N}_{-+}^2}{\tilde{N}_{++}\tilde{N}_{+-}} \right]^{1/4} \tag{2.4}$$

Cette méthode présente deux inconvénients majeurs. D'une part, elle nécessite un appareillage important qui ne peut pas être aisément intégré au dispositif de mesure des paramètres R et N. D'autre part, l'instrument de mesure ne permet d'analyser qu'une faible portion du faisceau de neutron. Un balayage sur l'ensemble du faisceau est donc nécessaire pour connaître la polarisation moyenne.

2.1.2 Mesure en utilisant l'anisotropie de l'émission d'électrons

Il est possible de déterminer la polarisation $\vec{P}_n$ du faisceau de neutrons en caractérisant l'anisotropie de l'émission des électrons. Selon Jackson, Treiman et Wyld, la probabilité qu'un faisceau de neutrons polarisé dans la direction $\vec{P}_n$ émette un électron avec une impulsion $\vec{p}_e$ est :

$$W(\vec{p}_e) \propto \left(1 + A\vec{P}_n \cdot \frac{\vec{p}_e}{E_e} \right) \tag{2.5}$$

L'asymétrie entre le nombre d'électrons émis "vers le haut" avec un angle $\theta = (\vec{P}_n, \vec{p}_e)$ et le nombre d'électron émis "vers le bas" avec un angle $\theta' = \pi - \theta$ est de la forme :

$$Asym(\theta) = \frac{\omega(\theta) - \omega(\theta')}{\omega(\theta) + \omega(\theta')} = \beta A P_n \cos(\theta) \tag{2.6}$$

avec $\beta = v/c$.

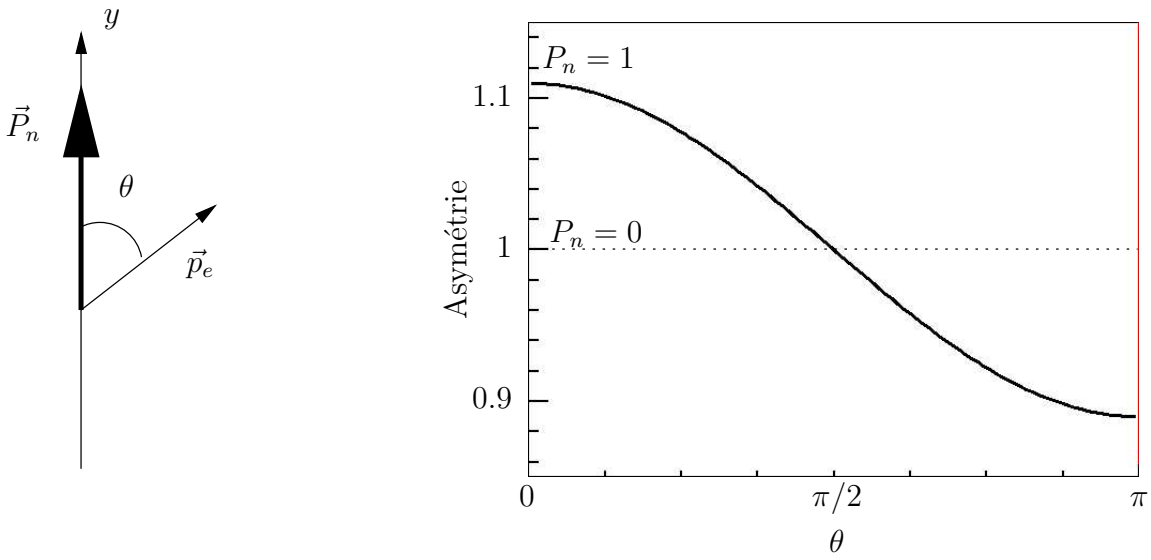

Fig. 2.2: Asymétrie haut-bas en fonction de l'angle θ formé par la direction de polarisation des neutrons et l'impulsion des électrons. La ligne continue représente une polarisation totale du faisceau de neutrons et la ligne pointillée une polarisation nulle.

La valeur de A est connue : $A = -0.1173 \pm 0.0013$. La dépendance entre l'asymétrie et l'angle θ, illustrée par la Figure 2.2, permet donc de déterminer la polarisation du faisceau de neutron.

Cette méthode présente l'avantage d'être non intrusive et de fournir une mesure de la polarisation moyenne du faisceau de neutrons à chaque instant. Il est donc possible de tenir compte d'une variation de la polarisation du faisceau de neutrons au cours du temps.

2.2 Mesure de la polarisation transversale des électrons

La polarisation transversale des électrons est la grandeur physique la plus difficile à déterminer. Pour ce faire, nous utilisons un phénomène appelé "diffusion de Mott".

2.2.1 La diffusion de Mott

Lorsqu'un électron se déplace au voisinage d'un noyau, le champ électrique généré par ce dernier attire la particule. Cette attraction a pour effet la transformation du mouvement de l'électron en orbite autour du noyau avec deux conséquences ; d'une part, une déviation de l'électron (diffusion coulombienne) et d'autre part la création d'un champ magnétique qui interagit avec le spin de l'électron ; on parle d'interaction spin-orbite, qui brise l'isotropie de la diffusion coulombienne.

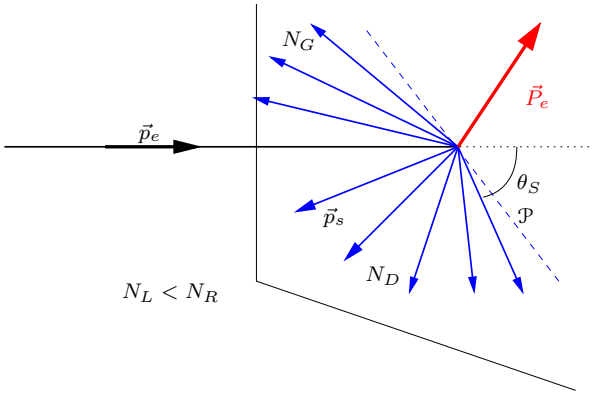

Fig. 2.3: Principe de la diffusion de Mott. Le faisceau d'électrons est diffusé par le matériau. Si on considère un plan de diffusion $\mathcal{P}$, et pour un angle de diffusion donné θ_S, l'asymétrie entre le nombre d'électrons diffusés à gauche $N_G(\theta_S)$ et diffusés à droite $N_D(\theta_S)$ est directement proportionnelle à la polarisation des électrons $\vec{P}_e$ selon la direction perpendiculaire au plan de diffusion.

Comme l'illustre la Fig. 2.3, si on considère un faisceau d'électrons diffusés par une cible et qu'on définit un plan de diffusion particulier, le nombre d'électrons diffusés à gauche et le nombre d'électrons diffusés vers la droite ne sont pas égaux.

Ainsi, on peut définir l'asymétrie gauche-droite par :

$$\begin{aligned} \epsilon &= \frac{N_D - N_G}{N_D + N_G} \\ \epsilon &= S(\theta_S) P_e \end{aligned} \tag{2.7}$$

où S est la fonction de Sherman (Fig. 2.4).

Cette asymétrie est donc proportionnelle à la polarisation des électrons perpendiculairement au plan de diffusion $\vec{P}_e$.

Plusieurs points doivent être précisés concernant cet effet. Tout d'abord, il n'est sensible que pour des électrons relativistes ; leur énergie étant alors suffisante pour traverser le cortège électronique des atomes. De plus, ce phénomène étant directement lié à la charge atomique, il est d'autant plus important que les atomes-cibles sont lourds. Enfin, comme le montre la Figure 2.4, le pouvoir d'analyse du phénomène de Mott est maximal pour des déviations importantes (de l'ordre de 140°).

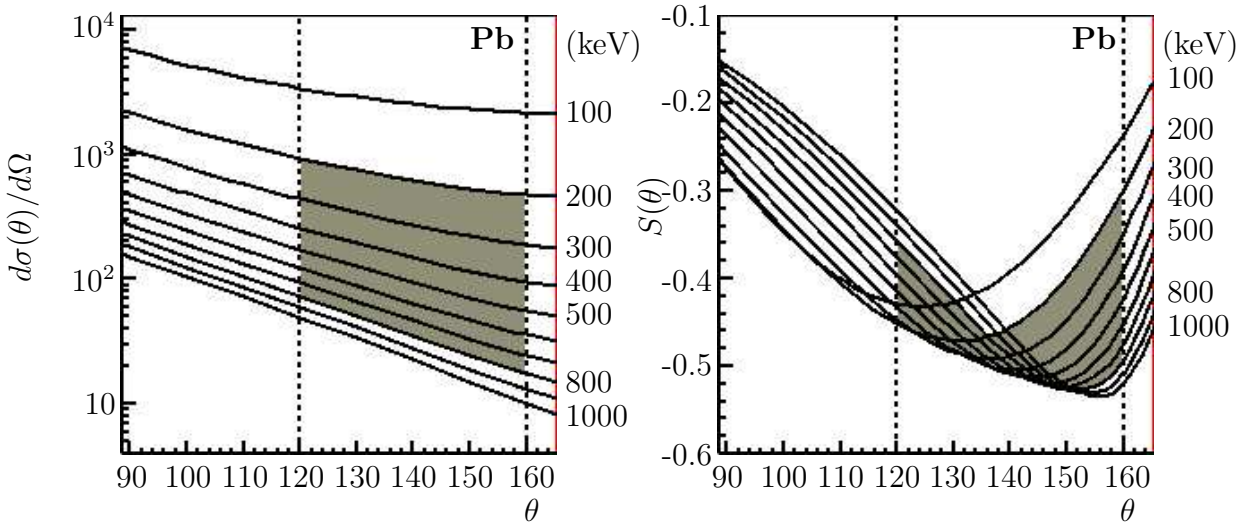

Fig. 2.4: Section efficace de diffusion et pouvoir d'analyse pour une cible de plomb (Z=82). La zone grisée représente les intervalles d'angle et d'énergie utiles à notre expérience.

2.2.2 Application à notre problématique

Pour déterminer le paramètre R nous devons mesurer la polarisation des électrons dans la direction perpendiculaire à l'impulsion $\vec{p}_e$ et à la polarisation des neutrons $\vec{P}_n$. Selon l'équation (1.1), l'influence de R est maximale si ces deux vecteurs sont orthogonaux. Le faisceau de neutrons étant polarisé verticalement, la mesure se fait idéalement avec des électrons émis horizontalement, et diffusés dans le plan porté par les vecteurs $\vec{p}_e$ et $\vec{P}_n$.

Dans le cas du paramètre N, il est nécessaire de déterminer la polarisation transversales des électrons dans la direction portée par le plan $(\vec{P}_n, \vec{p}_e)$. Etant donnée les contraintes sur la mesure de R imposant la détection d'électrons émis quasi-horizontalement, la sensibilité maximale vis-à-vis de N est obtenue en mesurant les diffusions dans le plan horizontal.

En théorie, la mesure des deux paramètres revient donc à mesurer, pour des électrons émis quasi-horizontalement, les asymétries entre les électrons diffusés à gauche et à droite (N) et diffusés vers le haut et vers le bas (R). Malheureusement, les contraintes statistiques ne nous permettent pas de nous contenter d'un dispositif aussi simple. Nous avons donc opté pour un détecteur étendu, analysant une large portion du faisceau de neutron. Plutôt que de se limiter aux azimuts de diffusion précédemment évoqués, nous enregistrons toutes

les directions de rétro-diffusions. La polarisation mesurée est donc en règle générale le résultat de l'effet conjugue de R et de N.

Le dispositif expérimental utilisé, schématisé figure 2.5, est constitué de deux ensembles symétriques, situé de part et d'autre du faisceau de neutrons. Chaque partie comprend une chambre à fils, une feuille de plomb et un mur de scintillateurs.

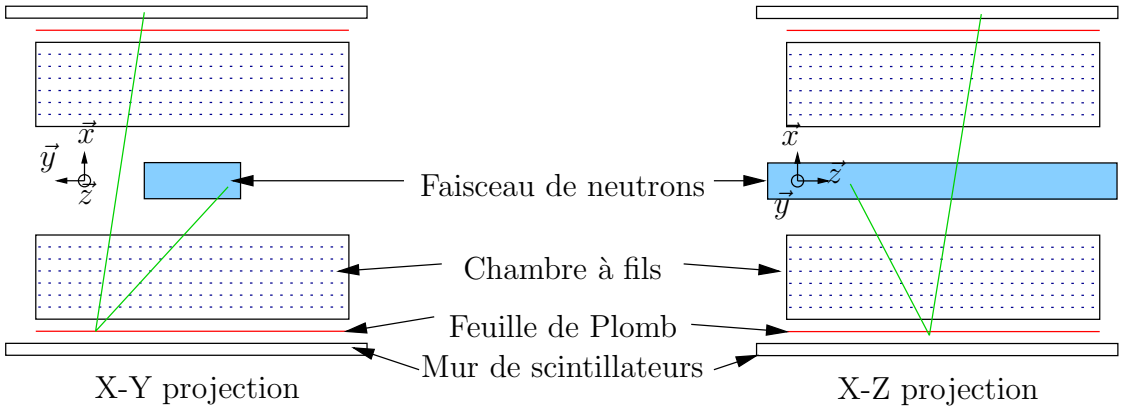

Fig. 2.5: Vue schématique du dispositif expérimental, constitué de deux ensembles symétriques placés de part et d'autre du faisceau de neutrons et comprenant une chambre à fils, une feuille de plomb et un mur de scintillateurs. Un évènement typique est représenté en vert : un électron traverse une chambre, est diffusé par la feuille et retraverse le dispositif expérimental avant de s'arrêter dans le mur de scintillateurs opposé.

Les chambres à fils permettent de détecter les trajectoires des électrons, les feuilles de plomb servent de cible de Mott et les murs de scintillateurs mesurent l'énergie des électrons.

Chapitre 3

Travaux effectués durant la thèse

Il est possible de diviser le travail effectué au cours de cette thèse en deux parties.

Tout d'abord, l'aspect pratique, majoritairement effectué à l'Institut Paul Scherrer (Villigen, Suisse), qui a consisté à améliorer le dispositif expérimental existant et à participer aux campagnes de prises de données effectuées en 2003 et 2004.

La deuxième partie consista à analyser les données récoltées en vue d'extraire les valeurs des paramètres R et N. Cette partie du travail s'est effectuée à la fois au Laboratoire de Physique Corpusculaire (Caen) et à l'Université Jagellon (Cracovie, Pologne)

3.1 Aspect pratique

3.1.1 Améliorations du dispositif expérimental

3.1.1.1 Statut fin 2002

A mon arrivée au PSI en septembre 2002, le dispositif expérimental était à mi-chemin entre le prototype et l'état final (Fig. 3.1) :

- L'enceinte remplie d'hélium ("HeBox") où les neutrons se désintègrent en vol avait été testée.
- Un dispositif magnétique permettant de maintenir la polarisation des neutrons le long de la ligne avait été construit à l'université Catholique de Leuven et installé peu de temps auparavant.
- Une version simplifiée de la chambre à fil ("MWPC") était opérationnelle et avait permis la validation du concept de cathodes actives pour détecter la trajectoire des électrons selon une projection horizontale. Les parties manquantes de cette chambre, ainsi que la deuxième chambre à fils étaient en construction à l'université Jagellon.
- Les feuilles de plomb devant servir de cible pour la diffusion de Mott étaient en construction au Laboratoire de Physique Corpusculaire.
- Un mur de scintillateurs ("Hodoscope") avait également été construit et testé conjointement avec la chambre à fils.

3.1.1.2 Travail sur les scintillateurs

Le mur de scintillateurs présentait plusieurs défauts :

- une perte de signal de l'ordre de 70% observée lors de l'activation du champ magnétique.
- une forte atténuation du signal lumineux au sein des scintillateurs.

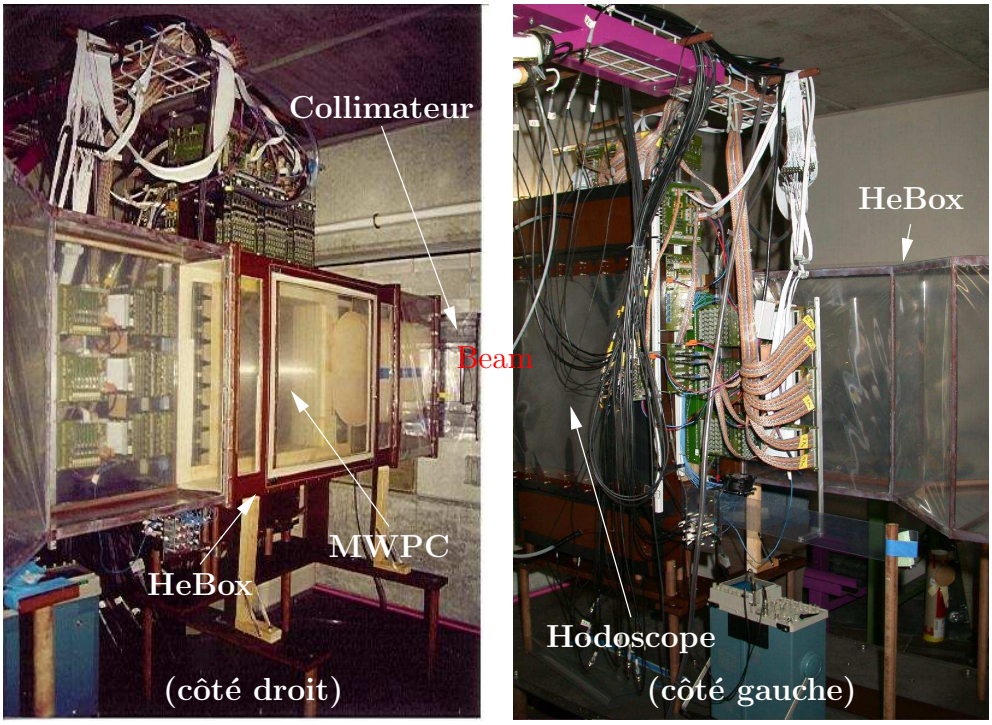

Fig. 3.1: Vue du dispositif expérimental à l'été 2002. La partie magnétique a été montée quelques mois plus tard.

L'influence du champ magnétique fut résolue en optimisant la position du blindage de μ-métal autour des photomultiplicateurs. La perte de signal due au champ magnétique fut réduite à moins de 10% sans ajout de blindage supplémentaire, ce qui a été jugé acceptable.

Le deuxième problème était dû à l'enrobage des scintillateurs : le Téflon utilisé se collait à la surface des scintillateurs en dégradant les conditions de réflection totale de la lumière. Nous avons alors remplacé ce matériau par du Mylar aluminisé qui ne présente pas ce défaut.

3.1.1.3 Manipulateur de la source de calibration

Afin de calibrer les scintillateurs, nous utilisons une source ponctuelles de Bi^{207}. Ce matériau se désintègre en Pb^{207} par capture électronique. Le noyau ainsi créé se désexcite en émettant des électrons suivant des énergies déterminées. (Table 3.1). En plaçant la source au centre du dispositif expérimental, il est donc possible de calibrer les scintillateurs.

Cette calibration utilise les chambres à fils, pour deux raisons. D'une part la coïncidence chambre à fils/scintillateur permet de rejeter le bruit de fond produit par des particules non chargées ainsi que par les particules chargées ne traversant pas la chambre (contamination, rayons cosmiques...). D'autre part, les informations délivrées par les chambres permettant la reconstruction des traces et il est possible de déterminer la quantité d'énergie perdue par les électrons avant leur détection.

Afin de manipuler la source radioactive dans l'enceinte du faisceau (remplie d'hélium), j'ai mis au point un bras manipulateur. Le système, commandé par une interface sous LabView, permet de déplacer la source à une vitesse donnée au milieu du dispositif

Energie (keV)	Electrons (pour 100 désint.)
5-16	53.8
56-62	
68-75	2.8
80-88	
482	1.52
554-557	0.44
566-567	0.15
810	0.003
976	7.03
1048-1051	1.84
1060-1061	0.54
1682	0.02

Tab. 3.1: Energies et intensité relative des électrons émis par le Pb^{207} crée par capture électronique à partir Bi^{207}. Les valeurs en rouges sont les énergies utilisées pour notre calibration.

expérimental de façon à simuler une source d'électron quasi-homogène .

3.1.1.4 Autres éléments conçus pendant la thèse

Une partie du dispositif expérimental ayant été modifiée ou rajoutée, son support a du être intégralement reconstruit. Le problème majeur fut ici de le concevoir de telle manière que le dispositif puisse être transporté sans démontage.

3.1.2 Campagnes de prises de données

Au cours de l'été 2004 a eu lieu de la première campagne d'acquisition de données. Le but était d'obtenir assez d'évènements pour déterminer la valeur de R avec une précision de 1%. Cette campagne s'est déroulée, sans interruption, entre le 15 août et le 26 octobre ; les arrêts faisceau hebdomadaires étant utilisés pour procéder à une calibration des scintillateurs.

Chaque cible de plomb pouvait être escamotée, ce qui permettait de détecter des électrons diffusés selon quatre configurations :

- Les deux feuilles insérées
- La feuille 1 sortie, la 2 insérée
- Les deux feuilles sorties
- La feuille 1 insérée, la 2 sortie

Ces quatre états se succédaient dans un cycle d'une douzaine d'heures, pour une durée relative de 58%, 19%, 4% et 19% respectivement. Les configurations avec une feuille escamotée servaient à estimer le nombre d'électrons diffusés par l'entourage de la cible.

Les deux inverseurs de spin (spin flippers) présents permettaient d'effectuer la mesure pour quatre états de la polarisation $\vec{P}$ des neutrons :

- les deux flippers sont éteint. $\vec{P} = \vec{P}_0$
- le premier flipper est allumé. $\vec{P} = -\eta_1 \vec{P}_0$
- les deux flippers sont allumés $\vec{P} = \eta_1 \eta_2 \vec{P}_0$

– le deuxième flipper est allumé. $\vec{P} = -\eta_2 \vec{P}_0$

où η_1 et η_2 sont les efficacités respectives des deux inverseurs de spin et $\vec{P}_0$ la polarisation du faisceau.

3.2 Analyse des données expérimentales

3.2.1 Reconstruction des évènements

La première étape de l'analyse des données est la reconstruction des évènements enregistrés. Les données provenant de l'acquisition sont de deux types :

– des mesures de temps provenant des chambres à fils et des photomultiplicateurs
– des mesures d'amplitude provenant des photomultiplicateurs

Ces informations permettent au programme appelé NPRun de reconstruire les traces des électrons, et conjointement avec les mesures de calibration, de déterminer leur energie. Nous avons alors deux types d'évènements reconstruits :

– Les traces directes (Single Tracks) sont les plus simples. Ce sont des électrons qui ont traversé la feuille sans être sensiblement diffusés. Ils laissent alors une trace unique dans une des chambres et sont arrêtés dans le mur de scintillateurs correspondant 3.2.

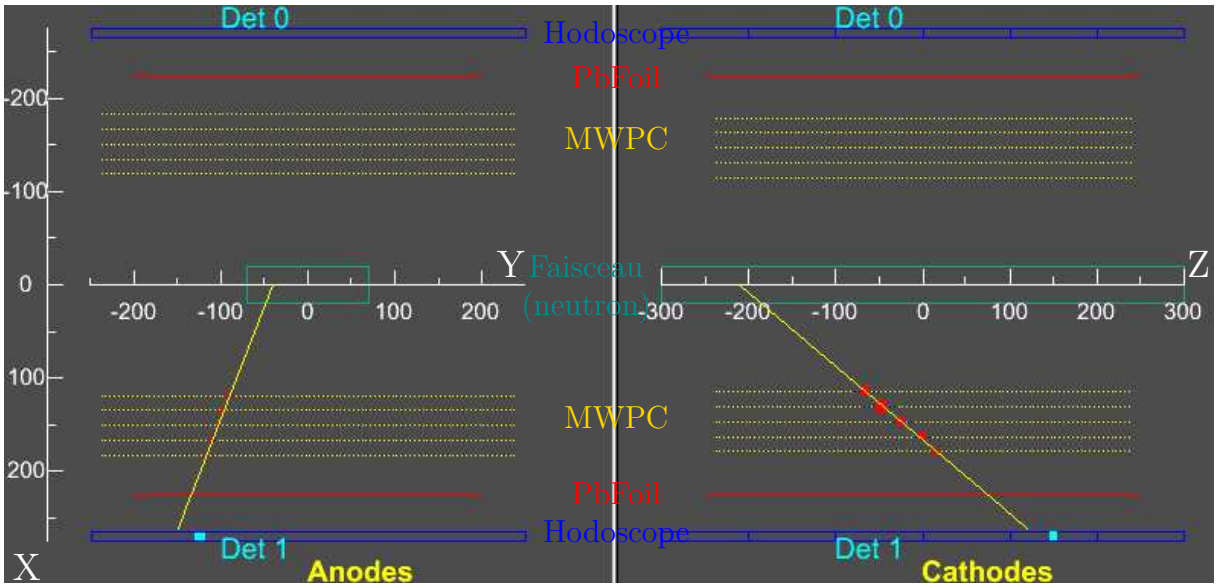

Fig. 3.2: Evènement "Single Track" reconstruit par le programme d'analyse. Chacune des deux types d'électrodes donne une projection de la trajectoire : (XY) pour les anodes et (XZ) pour les cathodes. Ici, la particule chargée est vraisemblablement émise par le faisceau de neutron, traverse une chambre avant d'être détectée par un scintillateur.

– Plus intéressant mais plus rares, les traces en "V" (V-Tracks) sont caractéristiques de la rétro-diffusion d'électrons. Nous observons alors deux traces dans une chambre, une trace dans l'autre chambre, et un signal provenant des scintillateurs correspondants 3.3.

Le programme NPRun a été conçu avant mon entrée dans la collaboration. Mon rôle ici a consisté majoritairement à trouver et résoudre les "bugs" de ce programme ainsi qu'à ajouter quelques améliorations.

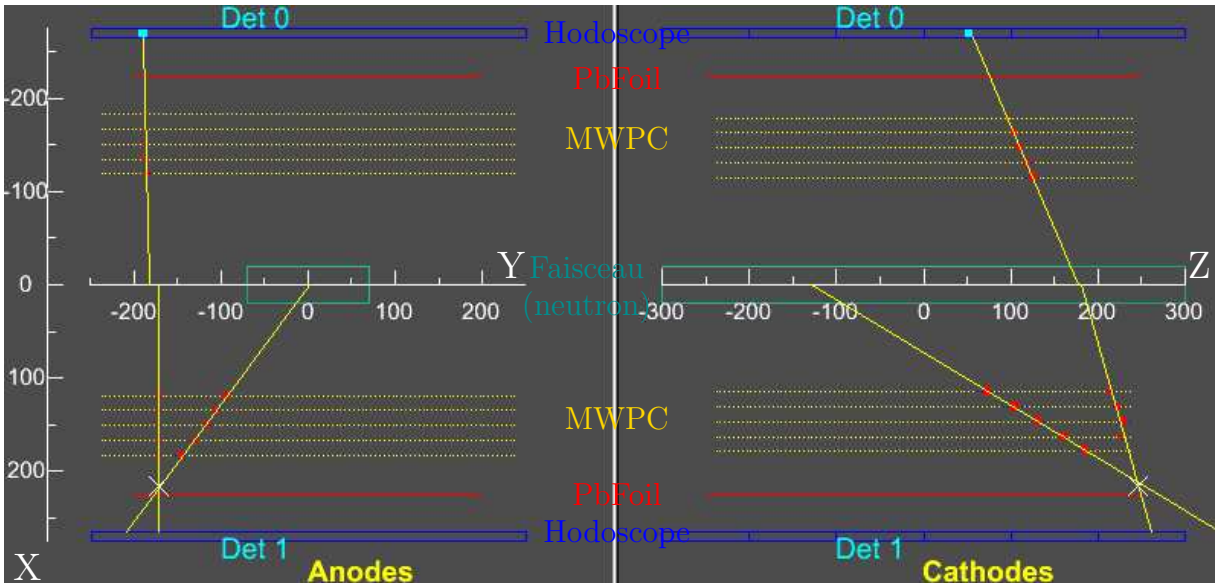

Fig. 3.3: Evènement "V-Track" reconstruit par le programme d'analyse. La particule est émise par le faisceau, traverse une chambre, est rétro-diffusé par la feuille de plomb et retraverse le détecteur avant d'être détectée par un scintillateur.

3.2.2 Extraction des paramètres R et N

A l'issue de l'étape de reconstruction des évènements, nous disposons d'une liste de V-Tracks définis par leurs caractéristiques :

- la position d'émission.
- l'impulsion à l'émission.
- l'impulsion après diffusion.
- la polarisation du faisceau de neutron.

Ces caractéristiques nous permettent de regrouper les évènements. Il est alors possible de construire les asymétries nécessaires à l'extraction des paramètres R et N. La mise au point de la méthode a été une partie importante de mon travail d'analyse que je ne développerai pas ici. Elle est traité de manière exhaustive au chapitre 8.

3.2.3 Etude du bruit de fond

Toutes les méthodes d'extractions des paramètres R et N nécessitent des données exemptes de bruit de fond ou dont ses caractéristiques sont connues, ce qui m'a poussé à étudier son origine.

Ces évènements laissent une trace dans les chambres à fils ; ce sont donc des particules chargées. N'ayant pas de preuve de la présence de positron, nous avons considéré que ces évènements sont des électrons. Leur origine peut alors être de deux types : soit ils résultent d'une désintégration de type β^- autre que celle des neutrons, soit ils ont été émis par interaction d'une rayonnement électromagnétique avec la matière. En particulier, une quantité importante de rayonnements γ provient de la ligne de neutron et peuvent générer des électrons par diffusion Compton.

3.2.3.1 Tomographie

Chaque électron traversant une chambre à fils laisse une trace qui peut être reconstruite. Pourtant, ce dispositif ne fournit qu'une indication sur la trajectoire de la particule ; son origine reste inconnue. Nous considérons alors l'ensemble des traces observées de façon à déterminer des zones de convergence.

Si le principe peut sembler simple, son implémentation est plus délicate. Il n'est en effet pas possible d'observer en trois dimensions ces zones de convergence. Aussi est il nécessaire de choisir des plans d'observation afin d'étudier la façon dont les trajectoires les traversent.

Deux méthodes d'études ont été utilisées. D'une part nous pouvons définir une série de plans parallèles et étudier la convergence des trajectoires sur chacun d'eux (Fig. 3.4(a)). Le plan pour lequel la zone de convergence est la plus petite est celui où la source est localisée. Cette méthode présente l'avantage de ne pas diviser la statistique disponible. Elle est très efficace pour l'étude de sources petites et intenses. Elle devient au contraire très imprécise dans le cas de sources étendues. La deuxième méthode consiste, pour un plan donné, à sélectionner les angles d'incidence et à étudier le déplacement de l'image de la source sur le plan sélectionné (Fig. 3.4(b)). Si le plan est bien choisi en fonction de la source étudiée, l'image de la source aura la même position pour chaque angle d'incidence.

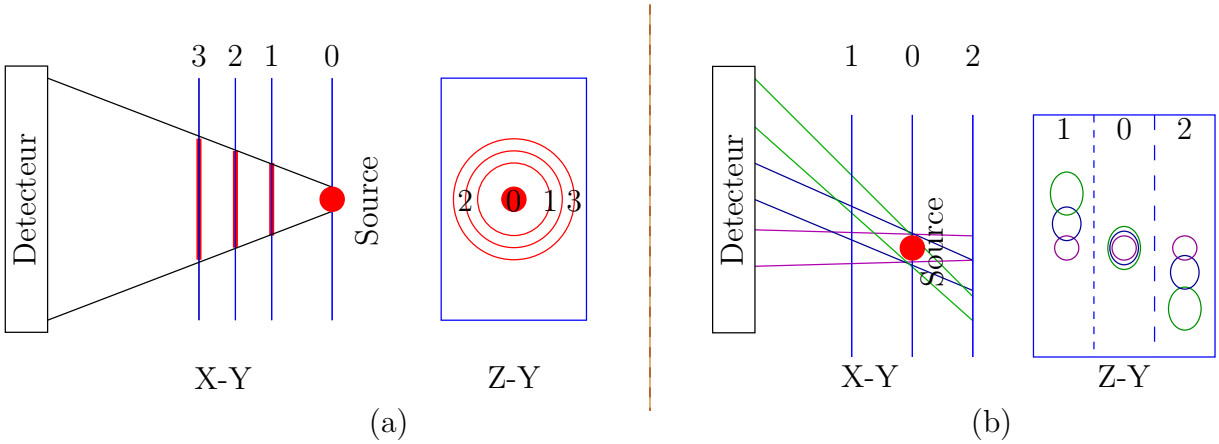

Fig. 3.4: Tomographie : (a) Localisation de la source en utilisant plusieurs plans d'étude ; (b) Localisation par sélection de différents angles d'incidence.

3.2.3.2 Les chambres à fils

Une des deux sources remarquables de bruits de fond est formée par l'intérieur des chambres à fils, plus précisément par les cadres qui supportent les fils. Ce bruit de fond est émis en plus grande quantité sur les faces horizontales : en haut et en bas.

L'étude des électrons émis juste lors d'un arrêt du faisceau tend à montrer que ce bruit de fond est majoritairement produit par effet Compton. Néanmoins des éléments supplémentaires doivent être vérifié avant de pouvoir conclure. Il est également possible que ce bruit de fond ne provienne pas réellement des cadres de Stesalit des chambres ; mais des supports des fils. Seule une etude plus complète avec des échantillons de matériau

placés à l'intérieur de l'HeBox pourrait nous permettre d'obtenir une conclusion définitive sur cette source.

3.2.3.3 Le collimateur

L'intérieur du volume contenant le faisceau de neutrons est tapissé de feuilles de polymère contenant du fluorure de Lithium (LiF). Le Lithium est composé à 90 % de Li^6, matériau ayant une très grand section efficace de capture neutronique selon la réaction :

$$n + Li^6 \rightarrow He^4 + T$$

La capacité d'absorption de ce polymère permet de capturer 97% des neutrons par millimètre de polymère.

La deuxième source remarquable de bruit de fond est localisée sur deux morceaux de polymère dopé au Li^6 placé en avant des chambres à fils et servant à absorber les neutrons diffusés hors du faisceau. De la même façon que précédemment, la majeure partie du bruit de fond provenant de cette source est probablement à due des électrons Compton émis par les γ provenant du faisceau de neutron.

Chapitre 4

Conclusion

Dans l'introduction, nous avons montré l'importance d'une mesure précise des corrélations angulaires au sein de la désintégration β du neutron pour sonder le modèle standard. L'expérience décrite dans ce document a pour but la détermination simultanée des paramètres R et N, définis par Jackson *et al.*, pour la désintégration du neutron libre. Une valeur non nulle du paramètre R serait le signe du violation de la symétrie sous le renversement du temps, non prévue par le modèle standard, et ouvrirait la voie à ses extensions. La mesure du paramètre N permet de caractériser la sensibilité de notre détecteur.

Quatre observables sont requises par cette mesure :

- la polarisation des neutrons.
- l'impulsion des électrons.
- les deux composantes transversales de la polarisation des électrons.

La polarisation des neutrons est déterminée en utilisant un polarimètre à super-miroirs ainsi qu'en se servant de l'anisotropie de l'émission des électrons. La polarisation transversales électrons est mesurée grâce à un polarimètre de Mott.

Durant cette thèse j'ai travaillé à la fois sur le dispositif expérimental et sur l'analyse des données accumulées. La partie pratique a consisté tant à l'amélioration du dispositif et à la création de nouveaux éléments qu'à la participation aux campagnes de prises de données. L'analyse a principalement porté sur deux aspects : d'une part la façon d'utiliser les V-Tracks pour en extraire les valeurs des paramètres R et N, et d'autre part l'étude de l'origine du bruit de fond.

Part II

More detailled, with Shakespeare's language...

Chapter 5

Introduction

5.1 Historical background

Observed by Becquerel in 1896, the β-decay was identified by Rutherford in 1899. In 1911, Meitner and Hahn discovered that the energy of the emitted electrons had a continuous spectrum, in apparent contradiction with energy conservation. To explain that problem, Pauli suggested in 1930 that an extremely light neutral particle called *neutrone* ("neutron") was emitted during β-decay and had simply not yet been observed. In 1931 Fermi renamed Pauli's "neutron" *neutrino*, and published in 1934 a very successful model of β-decay involving the neutrino, making the first step towards the construction of a weak force theory.

Laporte introduced in 1924 the notion of parity for atomic systems: he classified the atoms as either "even" (parity $+1$) or "odd" (parity -1), depending on the symmetry of their wavefunction. He discovered that when an atom state changes with a photon emission, the atom parity is inverted and the photon has an odd parity. The parity of a system is thus conserved by the atomic transition. Wigner proved in 1927 that this empirical rule is a consequence of the left-right symmetry of the electromagnetic forces. Since this symmetry was unquestioned in other interactions, the parity (P) conservation was assumed for the newly discovered β-decay.

In 1949, two new particles were discovered by Powell within the cosmic rays: the τ- and θ-meson decaying respectively into three pions and two pions. Thorough studies of these particles gave identical life-times and masses. They could have been the same particle without the odd-parity of the pion inducing a different parity for the τ and the θ. The "$\theta - \tau$ puzzle" lasted up to 1956 when Lee and Yang, after a careful check of the experiments about the weak interaction, discovered that there was no experimental proof of parity conservation in the weak force. They proposed a list of experiments dedicated to this issue [1]. Following those ideas, Wu *et al.* "drank to the overthrow of the law of parity" [2] in 1957: the parity was not conserved in the β-decay of ^{60}Co [3]. This experiment was also a proof of a charge conjugation invariance violation [4]. Since both P- and C-invariances were violated, the process was invariant under CP. The CP-symmetry was considered as conserved up to 1964 when Christenson *et al.* discovered a CP-violation in the decay of the K^0 meson [5].

5.2 Standard Model and fundamental symmetries

Interaction	Relative Magnitude	Range
Strong nuclear force	10^{40}	$1.4 \times 10^{-15} m$
Electromagnetic force	10^{38}	∞
Weak nuclear force	10^{15}	$10^{-18} m$
Gravity	10^{0}	∞

Table 5.1: Fundamental Interactions

The current theoretical framework of particle physics is the Standard Model (SM). Developed from the 70's, it gathers the electroweak theory of Glashow, Weinberg and Salam [6] with quantum chromodynamics. It describes three of the four fundamental forces (Table 5.1): the weak interaction, related to the β-decay ; the strong interaction responsible for the cohesion of the nuclei and the electromagnetic interaction.

A SM cornerstone is the so-called CPT theorem which states that a process is invariant under the combined reversal of charges, spatial orientation and arrow of time. So far, no evidence of CPT violation has been detected and we can thus assume that CP-violation and T-violation are equivalent.

In contrast to CPT, the existence of CP-violation is firmly established in the decay of the neutral meson K [5] and B [7, 8]. It was also pointed out that the CP-violation is a *sine qua non* condition to explain the high asymmetry between matter and anti-matter in the universe [9]. Several frameworks exist to introduce the CP-violation in the models: the Cabibbo-Kobayashi-Maskawa (CKM) mixing of the quark states [10, 11], a θ term in the QCD Lagrangian [12], the superweak interaction [13], models involving left and right-handed gauge bosons [14], multiplets of Higgs particles or leptoquarks. The θ interaction term and CKM mixing matrix are already embedded into the SM, but the latter is the only one that arises within the context of known physics: the CP-violation in the decay of the K and B is a natural consequence of the mixing states. The θ term introduces a CP-violation in the strong interaction and the best observable related to this parameter is the neutron electric dipole moment. So far the best accuracy reached limits the value of θ to 10^{-9}.

However these mechanisms are too weak by several orders of magnitude to explain the baryon asymmetry of the universe. One must also notice that since they predict only small effects for systems built of the lightest quarks (u and d), inaccessible with the precision of the present generation of experiment, the neutron decay is a good probe to search for physics beyond the Standard Model.

5.3 Influence of the electron polarization on the β-decay of oriented nuclei

Following the confirmation of Lee and Yang's hypothesis, Jackson, Treiman and Wyld questioned the possibility of time reversal invariance violation [15], not addressed by the

experiment made by Wu *et al.*. The Lee and Yang's interaction Hamiltonian density has the form

$$\begin{aligned} H_{int} &= (\bar{\psi}_p\psi_n)(C_S\bar{\psi}_e\psi_\nu + C_{S'}\bar{\psi}_e\gamma_5\psi_\nu+) \\ &+(\bar{\psi}_p\gamma_\mu\psi_n)(C_V\bar{\psi}_e\gamma_\mu\psi_\nu + C_{V'}\bar{\psi}_e\gamma_\mu\gamma_5\psi_\nu) \\ &+\frac{1}{2}(\bar{\psi}_p\sigma_{\lambda\mu}\psi_n)(C_T\bar{\psi}_e\sigma_{\lambda\mu}\psi_\nu + C_{T'}\bar{\psi}_e\sigma_{\lambda\mu}\gamma_5\psi_\nu) \\ &-(\bar{\psi}_p\gamma_\mu\gamma_5\psi_n)(C_A\bar{\psi}_e\gamma_\mu\gamma_5\psi_\nu + C_{A'}\bar{\psi}_e\gamma_\mu\psi_\nu) \\ &+(\bar{\psi}_p\gamma_5\psi_n)(C_P\bar{\psi}_e\gamma_5\psi_\nu + C_{P'}\bar{\psi}_e\psi_\nu) \\ &+\text{Hermitian conjugate} \end{aligned} \tag{5.1}$$

where C_i are the coupling constants labeled according to their transformation properties under the Lorentz transformation (Vector, Axial-vector, Scalar, Tensor and Pseudo-scalar); ψ_α is the Dirac spinor associated to the fermion α and $\sigma_{\lambda\mu} = -\frac{1}{2}i(\gamma_\lambda\gamma_\mu - \gamma_\mu\gamma_\lambda)$ with $\gamma_5 = \gamma_1\gamma_2\gamma_3\gamma_4$. Using this hamiltonian, Jackson, Treiman and Wyld determined the distribution function related to the electron energy, the emission angle and the nuclear polarization for allowed β-decay from oriented nuclei [4]:

$$\begin{aligned} \omega(\langle\vec{J}\rangle, \vec{\sigma}|E_e, \Omega_e)dE_e d\Omega_e = \frac{F(\pm Z, E_e)}{(2\pi)^4} p_e E_e (E_0 - E_e)^2 dE_e d\Omega_e \\ \times\xi\left\{1 + b\frac{m}{E_e} + \frac{\vec{p}_e}{E_e}\cdot\left(A\frac{\langle\vec{J}\rangle}{J} + G\vec{\sigma}\right)\right. \\ \left. +\vec{\sigma}\cdot\left[\boldsymbol{N}\frac{\langle\vec{J}\rangle}{J} + Q\frac{\vec{p}_e}{E_e+m}\left(\frac{\langle\vec{J}\rangle}{J}\cdot\frac{\vec{p}_e}{E_e}\right) + \boldsymbol{R}\frac{\langle\vec{J}\rangle}{J}\times\frac{\vec{p}_e}{E_e}\right]\right\} \end{aligned} \tag{5.2}$$

where $\langle\vec{J}\rangle$ is the expectation value of the angular momentum vector of the decaying nucleus, $\vec{p}_e$ and E_e are respectively the momentum and energy of the emitted electron, m is the mass of the emitted electron and Z the charge of the recoil nucleus. $\vec{\sigma}$ can be either the 2×2 Pauli spin matrix or a unit vector $\vec{n}$ along the electron polarization. In the first case, the expression Eq.(5.2) gives the density matrix of the spin states referred to the rest system of the moving electron. In the latter case, $\omega(\vec{n}|\ldots)$ gives the probability of emission of electrons whose spins are in the direction $\vec{n}$. The polarization of the emitted electrons in the direction $\vec{n}$ is then:

$$P(\vec{n}) = \frac{\omega(\vec{n}|\ldots) - \omega(-\vec{n}|\ldots)}{\omega(\vec{n}|\ldots) + \omega(-\vec{n}|\ldots)} \tag{5.3}$$

The coefficients ξ, b, A, G, N, Q and R depend on the coupling constants C_i and C_i' [4].

In Eq.(5.2), the other observables (recoil nucleus momentum, neutrino momentum,...) have been integrated out and their contributions cancelled. Thus, the influence of other parameters (D, V, L,...) is not visible.

5.4 Time reversal invariance violation

The time reversal transformation inverts the velocities, that is the momenta (linear velocity) and spins (angular velocities). In Eq.(5.2) it concerns the decaying nucleus polarization $\langle\vec{J}\rangle$, the electron momentum $\vec{p}_e$ and the electron polarization $\vec{\sigma}$. R is the parameter

related to the triple product $\vec{\sigma} \cdot (\langle \vec{J} \rangle \times \vec{p}_e)$, so a non-zero value of R would mean that the emitted electrons are polarized in the direction perpendicular to the plane spanned by the parent polarization and the electron momentum. This polarization would be inverted by the T-transformation, and thus the process would have a different behavior: *If $R \neq 0$, the neutron β-decay violates the T-invariance.*

Another T-violating parameter in the β-decay of polarized nuclei is D, related to the triple product of the decaying nucleus polarization $\langle \vec{J} \rangle$, the electron momentum $\vec{p}_e$ and the neutrino momentum $\vec{p}_\nu$.

To summarize:

- $R \rightarrow \vec{J} \cdot (\vec{p}_e \times \vec{\sigma})$ T-violating, P-violating
- $D \rightarrow \vec{J} \cdot (\vec{p}_e \times \vec{p}_\nu)$ T-violating, P-conserving

with $\vec{p}_\nu$ the momentum of the emitted anti-neutrino[1]. If the parameters are expressed as functions of the coupling constants C_i and C'_i, R and D become [15]

$$\begin{aligned} R\xi &= |M_{GT}|^2 \lambda_{J'J} \left[\pm 2Im(C_T C'^*_A + C'_T C^*_A) - \frac{\alpha Zm}{p_e} 2Re(C_T C'^*_T - C_A C'^*_A) \right] \\ &+ \delta_{J'J} M_F M_{GT} \sqrt{\frac{J}{J+1}} \left[2Im(C_S C'^*_A + C'_S C^*_A - C_V C'^*_T - C'_V C^*_T) \right. \\ &\pm \left. \frac{\alpha Zm}{p_e} 2Re(C_S C'^*_T + C'_S C^*_T - C_V C'^*_A - C'_V C^*_A) \right] \qquad (5.4) \\ D\xi &= \delta_{J'J} M_F M_{GT} \sqrt{\frac{J}{J+1}} \left[2Im(C_S C^*_T - C_V C^*_A + C'_S C'^*_T - C'_V C'^*_A) \right. \\ &\pm \left. \frac{\alpha Zm}{p_e} 2Re(C_S C^*_A - C_V C^*_T + C'_S C'^*_A - C'_V C'^*_T) \right] \qquad (5.5) \end{aligned}$$

where M_F and M_{GT} are respectively the Fermi and Gamow-Teller matrix elements, α is the fine structure constant, J is the spin of the decaying nucleus and

$$\begin{aligned} \xi &= |M_F|^2 (|C_S|^2 + |C_V|^2 + |C'_S|^2 + |C'_V|^2) \\ &+ |M_{GT}|^2 (|C_T|^2 + |C_A|^2 + |C'_T|^2 + |C'_A|^2) \qquad (5.6) \end{aligned}$$

The imaginary parts of the parameters R and D correspond to the T-violating contribution. The real parts are the corrections due to the final-state interactions (FSI) between the particles. In the case of R, it can be approximated by:

$$R_{FSI} = \frac{\alpha Zm}{p_e} A \qquad (5.7)$$

One can see that D and R are sensitive to different types of interactions. To first order, the scalar and tensor interactions can be considered as very small, therefore, the product $C_S C_T$ is negligible, and D is sensitive to a phase differing from 0 or π between the vector and the axial-vector interactions. In contrast, the R parameter is directly sensitive

[1]Since the neutrino is very difficult to detect, its momentum is deduced from the measurement of the momenta of the recoil nucleus and of the electron.

to admixture of exotic scalar and tensor interactions with the vector and axial-vector interactions.

The most recent values of the D parameter have been obtained by the emiT collaboration [16]

$$D = [-6 \pm 12(\text{stat}) \pm 5(\text{syst})]10^{-4}$$

and by the TRINE collaboration [17]

$$D = [-2.8 \pm 6.4(\text{stat}) \pm 3.0(\text{syst})]10^{-4}$$

Two other parameters are related to a T-odd triple product in the β-decay and therefore T-violating [15, 18]:

- $V \rightarrow \vec{J} \cdot (\vec{\sigma} \times \vec{p}_\nu)$
- $L \rightarrow \vec{\sigma} \cdot (\vec{p}_e \times \vec{p}_\nu)$

They can be written in terms of the coupling constants:

$$\begin{aligned} V\xi &= \delta_{J'J} M_F M_{GT} \sqrt{\frac{J}{J+1}} 2Im\Bigg[\pm\frac{m}{E_e}(C_S C_T'^* + C_S' C_T^* + C_V C_A'^* + C_V' C_A^*) \\ &\quad +(C_S C_A'^* + C_S' C_A^* + C_V C_T'^* + C_V' C_T^*)\Bigg] \\ L\xi &= |M_F|^2\Bigg[2Im(C_S C_V^* + C_S' C_V'^*) \pm \frac{\alpha Z m}{P_e}(|C_S|^2 - |C_V|^2 + |C_S'|^2 - |C_V'|^2)\Bigg] \\ &\quad \frac{|M_F|^2}{3}\Bigg[-2Im(C_T C_A^* + C_T' C_A'^*) \pm \frac{\alpha Z m}{P_e}(|C_T|^2 - |C_A|^2 + |C_T'|^2 - |C_A'|^2)\Bigg] \end{aligned} \quad (5.8)$$

The measurement of these two parameters requires the simultaneous measurement of the neutrino momentum and the electron transverse polarization. The measurement of each observable is already a diffult task, performed in the experiments measuring the D- and R-parameters. At the moment, no experiment has been designed to measure both simultaneously.

5.5 N and R parameters in neutron β-decay

Contrary to R, the parameter N is not T-violating. It is related to the scalar product of the neutron spin and the electron spin, and thus to the electron polarization in the direction of the neutron polarization. It can be written in terms of the coupling constants as :

$$\begin{aligned} N\xi &= 2Re\Bigg\{|M_{GT}|^2 \lambda_{J'J}\Bigg[\frac{1}{2}\frac{\gamma m}{E_e}(|C_T|^2 + |C_A|^2 + |C_T'|^2 + |C_A'|^2) \pm (C_T C_A^* + C_T' C_A'^*)\Bigg] \\ &+ \delta_{J'J} M_F M_{GT}\sqrt{\frac{J}{J+1}}\Bigg[(C_S C_A^* + C_V C_T^* + C_S' C_A'^* + C_V' C_T'^*) \\ &\pm \frac{\gamma m}{E_e}(C_S C_T^* + C_V C_A^* + C_S' C_T'^* + C_V' C_A'^*)\Bigg]\Bigg\} \end{aligned} \quad (5.9)$$

with $\gamma = (1 - \alpha^2 Z^2)^{\frac{1}{2}}$.

For neutron decay, $M_F = 1$, $M_{GT} = \sqrt{3}$, and the ratios $|C_S/C_V|$, $|C'_S/C_V|$, $|C_T/C_A|$ and $|C'_T/C_A|$ can be assumed small relative to unity. Additionally, $Z = 0$ so $\gamma = 1$, $C_V = C'_V = 1$ and $C_A = C'_A = -1.26$ To first order, N becomes

$$N_n \approx -\frac{m}{E_e} A \tag{5.10}$$

Since the N-parameter value is predicted by the SM, it is suitable to test the sensitivity of the experimental setup.

With the previous assumptions, the R-parameter becomes

$$R_n = \frac{Im[(C_V^* + 2C_A^*)(C_T + C'_T) + C_A^*(C_S + C'_S)]}{|C_V|^2 + 3|C_A|^2} + R_{FSI} \tag{5.11}$$

In order to compare the experimental value of R, it is convenient to write it as a linear combination of scalar and tensor interactions using the parameters:

$$S = Im\frac{C_S + C'_S}{C_A} \qquad \text{and} \qquad T = Im\frac{C_T + C'_T}{C_A} \tag{5.12}$$

then R becomes:

$$R_n = 0.28 \cdot S + 0.33 \cdot T + R_{FSI} \tag{5.13}$$

The purpose of the experiment described in this document is to measure the parameter R_n with a precision of $5 \cdot 10^{-3}$. To first order, the final state interaction term can be approximated by:

$$R_{FSI} \approx \frac{\alpha Z m}{p_e} A \tag{5.14}$$

The value of A is -0.1173 ± 0.0013 [19], thus it is possible to estimate $R_{FSI} \approx 0.001$, which is below the expected precision of the experiment. Therefore R_{FSI} can be neglected in the measured value of the R parameter.

Figure 5.1 shows the results of the experiments performed before the beginning of the nTRV project in 1996 together with the expected contribution of the neutron R-parameter. The ^{8}Li [20] and ^{19}Ne [21] are both experiments measuring the R-parameter of the β-decay. On the other hand, the experiments about Ar [22] were dedicated to the measurement of the a-parameter ($e - \nu$ angular correlation).

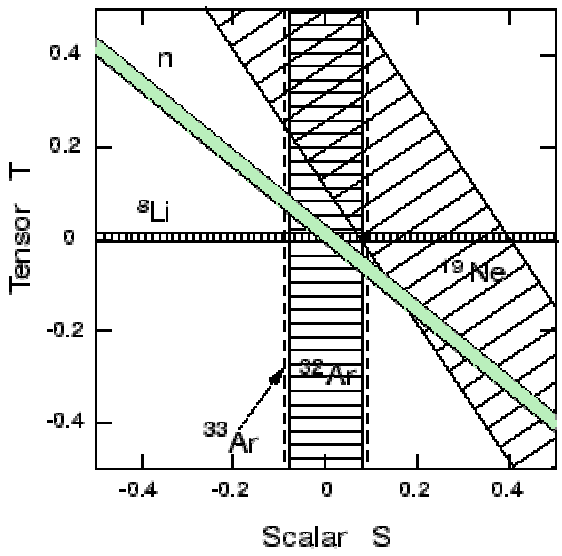

Figure 5.1: Results from the experiments investigating a time reversal invariance violation in the scalar and tensor sector. The quantities S and T are defined in the text. The bands indicate $\pm 1\sigma$ limits. The so-called "n" is an expectation of the R-correlation experiment result with $R = 0$ and an accuracy of ± 0.005

Chapter 6

Measuring principle

As shown in the previous chapter, N is related to the component of the polarization, collinear with the direction of the neutron polarization, and R is related to the component along the unit vector $(\langle\vec{J}\rangle \times \vec{p}_e)/\|\langle\vec{J}\rangle \times \vec{p}_e\|$. They are called respectively σ_{T1} and σ_{T2}. In order to determine these terms, four observables must be measured:

- The polarization of the neutron beam
- The momenta of the emitted electrons
- For each momentum, the polarization components σ_{T1} and σ_{T2} of the corresponding electron

The measurement of the neutron beam polarization is performed using two independent methods :

- a super-mirror polarimeter
- the angular correlation related to the A parameter

Both methods will be described in the first part of this chapter. The electron momentum is measured using MultiWire Proportional Chambers (MWPCs) for tracking and scintillator hodoscopes for the energy measurement. These detectors are also used as a part of a Mott polarimeter for the measurement of the electron polarization.

6.1 Neutron beam polarization

Two methods can be used to determine the neutron beam polarization; either with the use of a super-mirror analyzer or by the analysis of the electron emission anisotropy.

6.1.1 Polarization measured with a supermirror analyzer

This method is described by Serebrov *et al.* [23] and requires a system showed on Fig. 6.1. The analyzing system consists of two analyzers (A1 and A2) installed on a platform that can be rotated by 180°, allowing the two analyzers to be effectively interchanged. A1 and A2 are connected by a neutron guide containing a spin flipper (F2). Another spin flipper (F1) is placed before the analyzing system. Two additional flippers (F1' and F2')

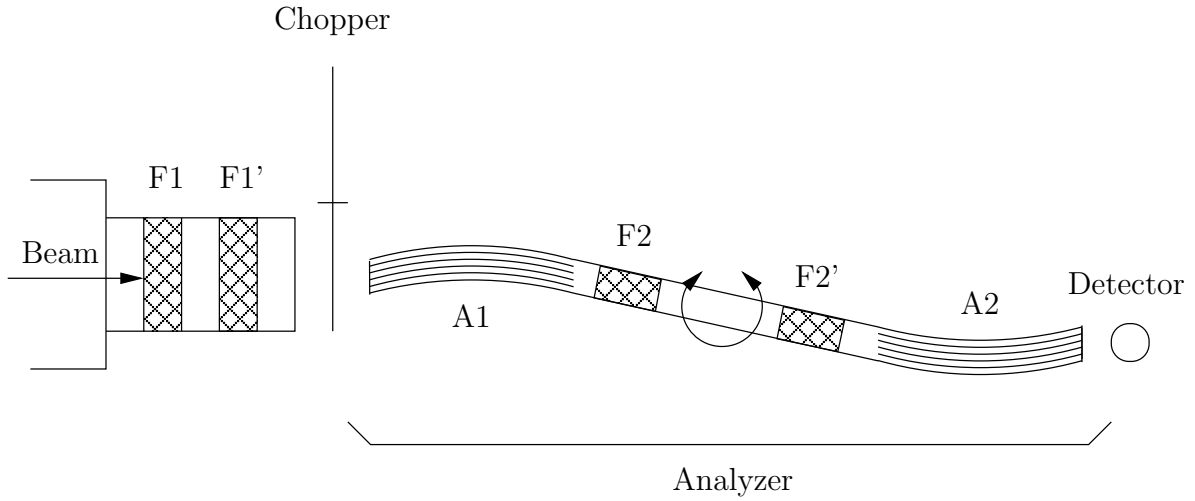

Figure 6.1: Practical scheme of the measurement method using supermirror analyzer. F1, F1', F2 and F2' are the spin flippers, A1 and A2 the supermirrors. The analyzer can be rotated by 180° in order to invert the sequence $A_1F_2F_2'A_2$ [23].

are available for decreasing the systematic uncertainties and for determining the flippers efficiencies. This protocol allows the measurement of the beam polarization without any knowledge about the super-mirrors analyzing powers[1].

The measurement protocol was to measure a time-of-flight (TOF) spectra $N_{F_1F_2}^{F_1'F_2'}$, normalized to the neutron beam intensity, for 9 states of flippers: N_{00}^{00}, N_{10}^{00}, N_{01}^{00}, N_{00}^{10}, N_{00}^{01}, N_{11}^{00}, N_{00}^{11}, N_{10}^{10} and N_{01}^{01} ("0" and "1" indicate the state "off" and "on" of the given flipper). These spectra are collected for both normal and inverted position of the analyzing section, noted $N_{F_1F_2}^{F_1'F_2'}$ and $\tilde{N}_{F_1F_2}^{F_1'F_2'}$ respectively. The spin-flipper efficiencies f are calculated for each flipper according to:

$$
\begin{aligned}
f_1 &= \frac{N_{10}^{10} - N_{10}^{00}}{N_{00}^{00} - N_{00}^{10}} \qquad & f_1' &= \frac{N_{10}^{10} - N_{00}^{10}}{N_{00}^{00} - N_{10}^{00}} \\
f_2 &= \frac{N_{01}^{01} - N_{01}^{00}}{N_{00}^{00} - N_{00}^{01}} \qquad & f_2' &= \frac{N_{01}^{01} - N_{00}^{01}}{N_{00}^{00} - N_{01}^{00}}
\end{aligned}
\tag{6.1}
$$

The polarization can be then calculated using only one pair of flippers: F_1/F_2 or F_1'/F_2'. For instance, eight linearly independent quantities are calculated for the pair of flippers F_1F_2[2]:

$$
\begin{aligned}
N_{++} &= (N_{00}f_1f_2 + N_{10}f_2) + (N_{01}f_1 + N_{11}) \\
N_{+-} &= (N_{00}f_1 + N_{10}) - (N_{01}f_1 + N_{11}) \\
N_{-+} &= (N_{00}f_2 - N_{10}f_2) + (N_{01} - N_{11}) \\
N_{--} &= (N_{00} - N_{10}) - (N_{01}f1 - N_{11})
\end{aligned}
\tag{6.2}
$$

[1]It is assumed that the analyzing power if a given analyzer is the same for both normal and reversed position

[2]The superscripts corresponding to the second pair of flippers are omitted

with the corresponding ones in "inverted" configuration:

$$\begin{aligned}
\tilde{N}_{++} &= (\tilde{N}_{00}f_1f_2 + \tilde{N}_{10}f_2) + (\tilde{N}_{01}f_1 + \tilde{N}_{11}) \\
\tilde{N}_{+-} &= (\tilde{N}_{00}f_1 + \tilde{N}_{10}) - (\tilde{N}_{01}f_1 + \tilde{N}_{11}) \\
\tilde{N}_{-+} &= (\tilde{N}_{00}f_2 - \tilde{N}_{10}f_2) + (\tilde{N}_{01} - \tilde{N}_{11}) \\
\tilde{N}_{--} &= (\tilde{N}_{00} - \tilde{N}_{10}) - (\tilde{N}_{01}f1 - \tilde{N}_{11})
\end{aligned} \tag{6.3}$$

The beam polarization is given by the superratio of the results obtained for the direct and inverted positions of the analyzing section:

$$P = \left[\frac{N_{-+}^2}{N_{++}N_{+-}} \cdot \frac{\tilde{N}_{-+}^2}{\tilde{N}_{++}\tilde{N}_{+-}}\right]^{1/4} \tag{6.4}$$

6.1.2 Anisotropy of the electron emission

In order to measure the neutron beam polarization, it is also possible to measure the angular correlation between the neutron polarization and the direction of the electron emission. This is the correlation used by Wu *et al.* to prove the violation of the P-invariance in the β-decay, and it is related to the parameter A

The idea is to measure the asymmetry between the number of electrons emitted with an angle $\theta = (\langle\vec{J}\rangle, \vec{p}_e)$ and with an angle $\theta' = \pi - \theta$ respectively. According to Eq.(5.2), the respective rates are :

$$\begin{aligned}
\omega(\theta) &\propto 1 + \beta A P_n \cos(\theta) \\
\omega(\theta') &\propto 1 - \beta A P_n \cos(\theta)
\end{aligned} \tag{6.5}$$

with $\beta = v/c$ and $\vec{P}_n = \langle\vec{J}\rangle/J$.

It is possible to define the asymmetry $Asym$ with:

$$Asym = \frac{\omega(\theta) - \omega(\theta')}{\omega(\theta) + \omega(\theta')} = \beta A P_n \cos(\theta) \tag{6.6}$$

The advantage of this method is that the neutron polarization can be measured together with the other observables, and it is possible to detected some polarization variations. The problem is that an experimental setup designed to maximize the sensitivity to N and R is not ideal for this measurement. Nevertheless, the achieved precision over the neutron polarization is expected to be high enough [24].

6.2 The Mott Polarimetry

6.2.1 History

Proposed by Goudsmith and Uhlenbeck in 1925 to explain the fine structure of certain atomic spectra, the intrinsic spin angular momentum and the associated spin magnetic moment were successfully incorporated into the quantum theory. Up to 1929, the experimental evidences of its existence, although compelling, were using electrons bound in atomic systems and were thus indirect.

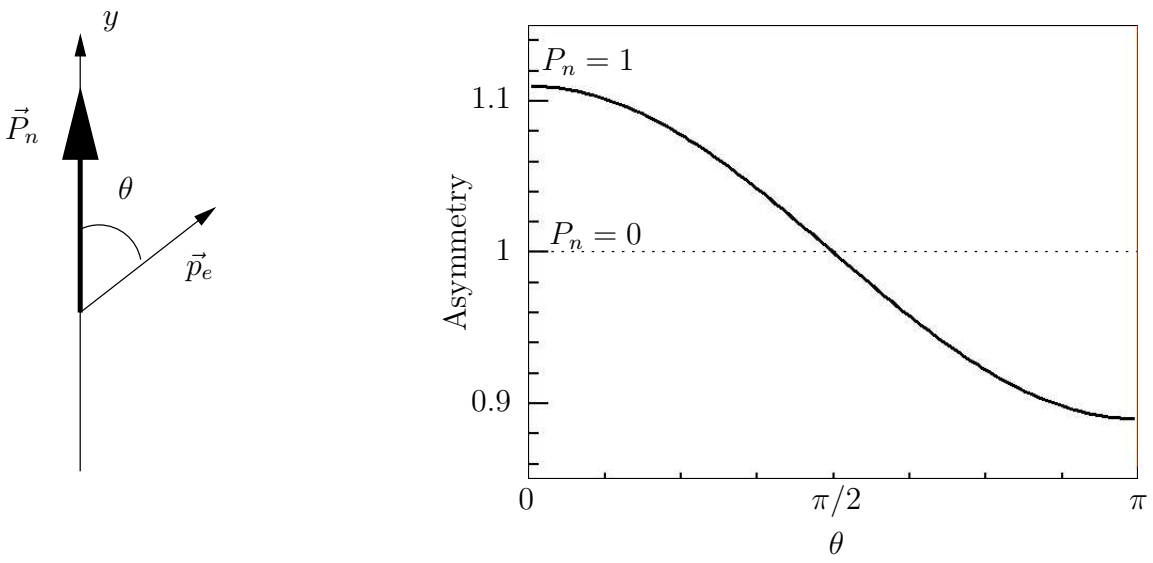

Figure 6.2: Up-Down asymmetry as a function of θ, the angle between the neutron polarization axis and the electron momentum. The full line corresponds to completely polarized neutron beam, and the dotted line to an unpolarized beam.

In 1929, Mott pointed out the impossibility of using a Stern-Gerlach experiment to measure directly the spin of a charge particle due to the uncertainty principle [25]. Instead, he proposed a double scattering experiment. An initially unpolarized electron beam will be scattered on a target made with high-Z nuclei. A scattering direction is then selected and the electrons are directed on a second high-Z nuclei target. Because of the spin-orbit interaction, the electrons coming from the first target have a significant polarization in the direction perpendicular to the scattering plane. For the same reason, the electrons will not be scattered isotropically on the second target, producing a left-right scattering asymmetry proportional to this polarization.
In 1942, Shull *et al.* successfully applied this idea to show the first direct evidence of the electron spin existence [26]. Then, the Mott polarimetry shifted from confirmation of fundamental theory to the production and/or measurement of the electron polarization.

6.2.2 Simplified principle

According to Mott [27], the asymmetry of the scattering effect is noticeable only if three conditions are satisfied :

- The velocity of the electrons must be comparable with c.
  The Mott scattering is due to an interaction between the nucleus and the electron, and occurs with a small impact parameter. Since the nucleus is surrounded with electrons, the electron must have enough energy to go through this cloud without being disturbed.

- The atomic number of the scattering atoms must be large, so that $(Z/137)^2 \sim 1$.
  The Mott scattering depends on the electric field created by the nucleus. This electric field is proportional to the charge of the nucleus and thus, the larger Z, the larger the effect.

- The angle of scattering θ must be large.
  This is an effect of the analyzing power, represented on the Fig. 6.3, together with the scattering cross section. One can notice that the analyzing power is quite large for angles between 120 and 160 degres.

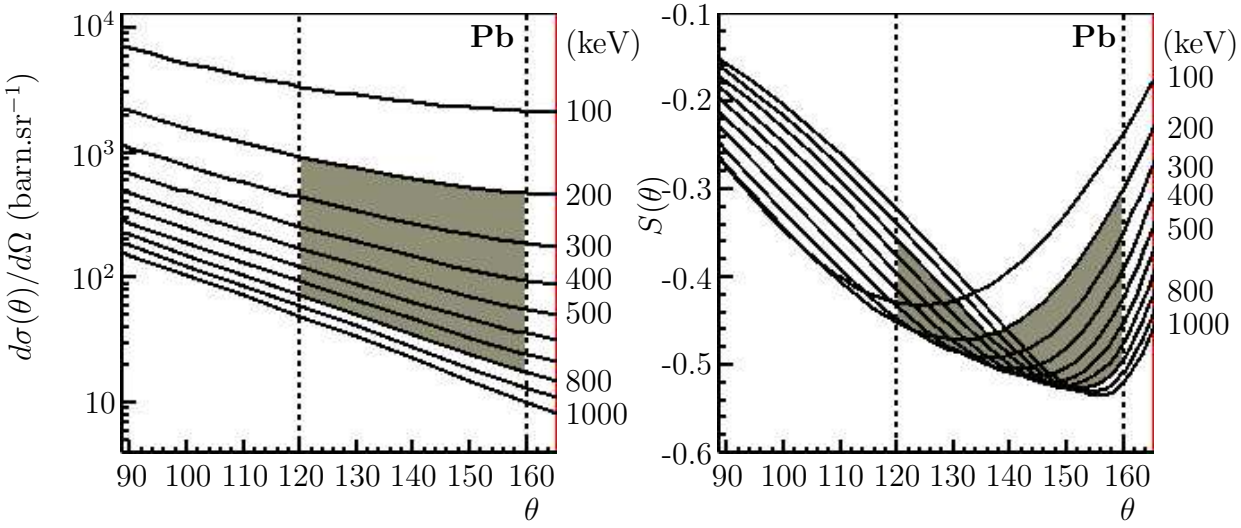

Figure 6.3: Cross section $d\sigma/d\Omega(E,\theta)$ and analyzing power $S(\theta)$ for a 1μm Pb target, obtained by interpolation of the Sherman tables [28]. The shadowed area represents the angular and energy ranges relevant for the described experiment.

The Mott scattering is based on spin-orbit interaction but this process can be described qualitatively using a classical picture [29]. The scattering of high-energy electrons by high-Z atoms can occur only with a small impact parameter. Thus, the atom can be seen as a bare nucleus of charge Ze. The impinging electron flies in the electric field generated by the nucleus $\vec{E}$ and this motion produces a magnetic field $\vec{B}$:

$$\vec{B} = -\frac{1}{c}\vec{v} \times \vec{E} \tag{6.7}$$

where $\vec{v}$ is the electron velocity. If $\vec{r}$ is the electron nucleus separation, the electron orbital momentum $\vec{L}$ is defined by :

$$\vec{L} = m\vec{r} \times \vec{v} \tag{6.8}$$

Therefore

$$\vec{B} = \frac{Ze}{mcr^3}\vec{L} \tag{6.9}$$

The interaction between this magnetic field and the electron magnetic moment $\vec{\mu}_s$ introduces an additional term $V_{so} = -\vec{\mu}_s \cdot \vec{B}$ in the scattering potential. The relation between the magnetic moment $\vec{\mu}_s$ and the electron spin $\vec{S}$ is $\vec{\mu}_s = -(ge/2mc)\vec{S}$ where $\vec{S}$ is the electron spin and g the g-factor ($g \sim 2$). V_{so} is therefore given by

$$V_{so} = -\frac{Ze^2}{2m^2c^2r^3}\vec{L} \cdot \vec{S} \tag{6.10}$$

An additional factor 1/2 has been added in order to account for the Thomas precession [30].

One can now consider a beam of electrons, polarized in the direction $\vec{P}_e$ (Fig. 6.4). $\vec{p}_e$ and $\vec{p}_s$ are the momenta associated respectively with the incident and scattered electrons and $\hat{n}$, the normal to the scattering plane, can be defined as

$$\hat{n} = \frac{\vec{p}_e \times \vec{p}_s}{|\vec{p}_e \times \vec{p}_s|} \tag{6.11}$$

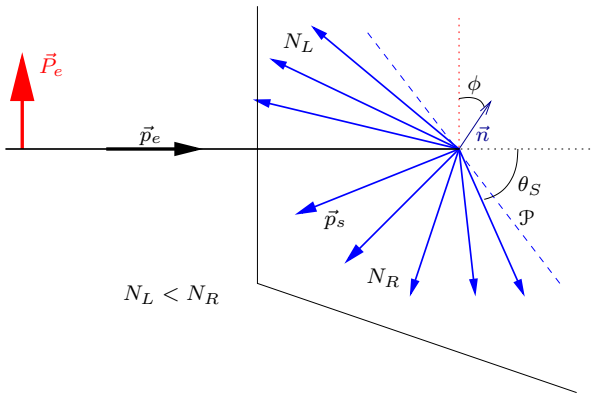

Figure 6.4: Principle of the Mott scattering. The polarized electron beam is scattered on the material. Because of the spin-orbit interaction, more electrons are scattered to the right (N_R) than to the left (N_L). If one considers the electrons scattered on the plane $\mathcal{P}$, the asymmetry is proportional to the polarization $\vec{P}_e$.

The spin-orbit term in the scattering potential for a scattering angle θ_S leads to a spin dependence in the scattering cross-section [31]:

$$\sigma(\theta_S) = I(\theta_S)[1 + S(\theta_S)\vec{P}_e \cdot \hat{n}] \tag{6.12}$$

where S is the analyzing power of the Mott scattering and I is the scattering cross section for unpolarized electrons. For one plane $\mathcal{P}$, and one scattering angle θ_S, the left-right asymmetry is defined by:

$$\begin{aligned} \epsilon &= \frac{N_R - N_L}{N_R + N_L} = \frac{\sigma(\theta_S) - \sigma'(\theta_S)}{\sigma(\theta_S) - \sigma'(\theta_S)} \\ &= \frac{[1 + S(\theta_S)\vec{P}_e \cdot \hat{n}] - [1 + S(\theta_S)\vec{P}_e \cdot -\hat{n}]}{[1 + S(\theta_S)\vec{P}_e \cdot \hat{n}] + [1 + S(\theta_S)\vec{P}_e \cdot -\hat{n}]} \\ \epsilon &= S(\theta_S)\ \vec{P}_e \cdot \vec{n} \end{aligned} \tag{6.13}$$

Thus, the asymmetry is proportional to the **polarization of the beam along** $\vec{n}$

6.2.3 Typical setup

A typical Mott polarimeter is presented on Fig. 6.5: it consists of a point like source, a small and thin Mott target, and two symmetrical detectors counting the electrons. If the

electron beam is not mono-energetic, these detectors must also measure the energy of the incoming electrons.

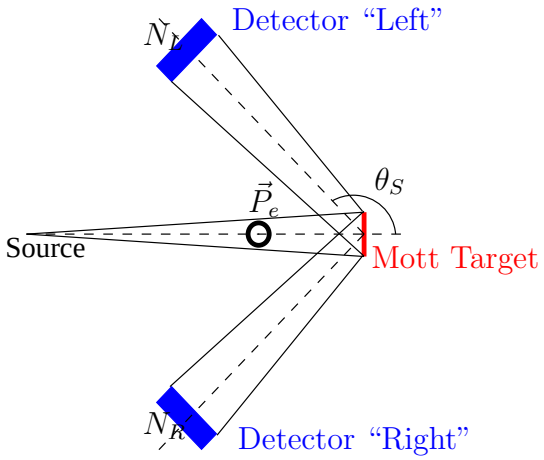

Figure 6.5: Typical setup for Mott polarimetry : The asymmetry between N_L and N_R is directly proportional to the electron polarization ($\vec{P}_e$) perpendicular to the scattering plane

The asymmetry measured between both detectors will be proportional to the polarization of the electron beam perpendicular to the scattering plane. This can also be performed with only one detector and an inversion of the beam polarization. It is also possible to do both; to have two detectors, and to measure with both, normal and inverted polarization. The advantage of this method is the use of a *super-ratio* instead of the normal asymmetry, more efficient to get rid of systematic effects. This point will be developed in the chapter 8.

In this simple setup, the calculation of the polarization is straightforward, but the disadvantage is that the statistics will be low, considering the limitation of the solid angle.

6.3 Implementation

The main goal of this experiment is to measure the parameter R related to the correlation $\langle\vec{J}\rangle\cdot(\vec{p}_e\times\vec{\sigma})$. In order to have the best sensitivity, it is necessary to measure the transverse polarization component of electrons which maximize this triple product, that is σ_{T2}. The best events are then those emitted perpendicularly to the neutron polarization direction. Since the Mott scattering asymmetry is directly proportional to the electron polarization in the direction perpendicular to the scattering plane, the best sensitivity is obtained with events scattered in the plane defined by the neutron polarization and the emission momentum.

The additional goal of the setup is the measurement of the parameter N related to the correlation $\langle\vec{J}\rangle\cdot\vec{\sigma}$. Since the Mott polarimeter is sensitive to the transverse component of the electron polarization, the most sensitive events are those scattered in the plane perpendicular to the neutron polarization.

If it was possible to concentrate the polarized neutrons in a very small volume, it would be enough to have two pairs of detector and one Mott scatterer set in the best way

in order to measure the parameters R and N. Since it is not possible to do this easily with a high number of neutrons, the electron source used is a beam of cold polarized neutrons, decaying in flight. This source is therefore large, with a typical visible volume of $1000 \times 80 \times 170\ mm^3$. Additionally, the measurement requests high statistics in order to reach the aimed precision, so the Mott scatterer and the detectors cannot be the "small" ones described previously. In order to obtain a good precision on the measurement, a characterization of the scattering is then needed, using tracking detectors before and after the process.

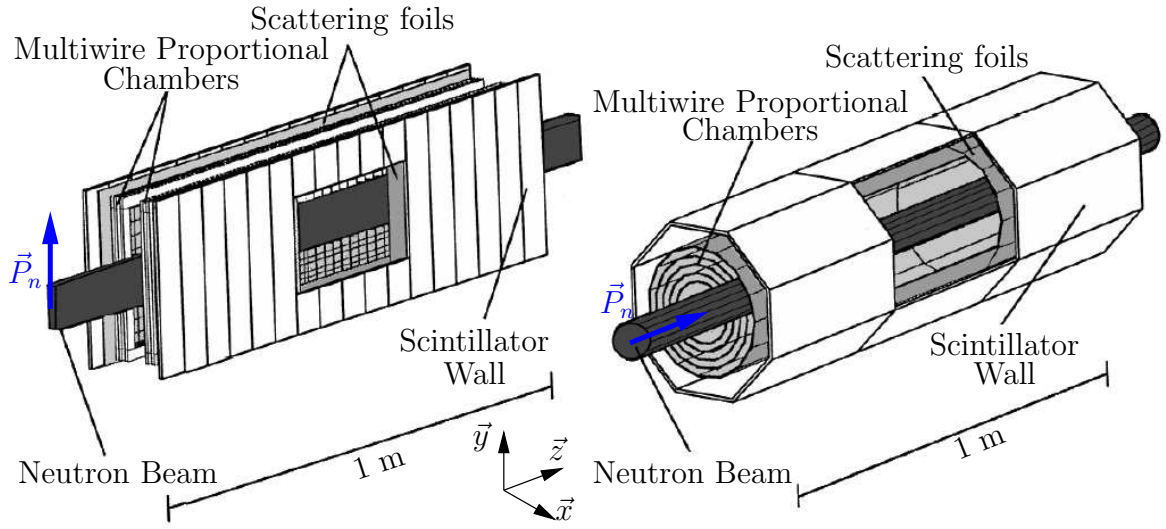

Figure 6.6: Possible designs elaborated to measure the R-parameter. One should notice that the direction of the neutron polarization is different for both designs.

Two designs were studied [32, 33, 34]. The first one, using a vertically polarized neutron beam between two symmetrical detectors (Fig. 6.6(left)) and the second one, taking advantage of an axially polarized beam surrounded by an axially symmetric detector (Fig. 6.6(right)).

Both designs use:

- MultiWire Proportional Chambers as tracking detectors.
- Thin lead-foils (Pb-foils) acting as a Mott scatterer.
- Hodoscopes to measure the energy of the electrons.

The advantages of the second setup are its acceptance and its axial-symmetry around the neutron polarization direction. Thus, it would have provided larger statistics than the first design, and the data would have been easier to analyze. However, such setup is much more complicated to implement and the first design was constructed.

The details of the setup will be described in the next chapter. The MWPCs, using both horizontal anodes and vertical active cathodes give two projections of the electron trajectories allowing a 3-dimensional reconstruction of the events. The Pb-foils are the Mott scattering target, made with high-Z material in order to maximize the cross section. Their thickness is a compromise between the maximization of the probability of scattering and the minimization of the probability of multiple-scattering. The scintillators measure

the energy of the electrons and they must be thick enough, not only to stop any electrons coming from the neutron decay but also to allow the distinction between these electrons and the ones from background, coming with a higher energy. Figure 6.7 shows a typical "good" event: an electron is emitted from the beam, goes through the MWPC and is scattered on the Pb-Foil before reaching the scintillator wall on the other side. This kind of event gives a V-shaped track (called *V-Track*) on **both** projections.

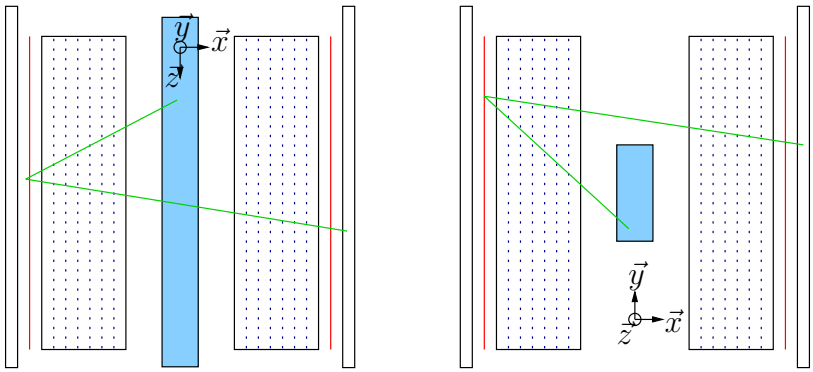

Figure 6.7: Typical "good" event : an electron is emitted from the beam (blue), scattered on the lead foil (red), and stopped in one scintillator. Tracks are reconstructed in both projections X-Y and X-Z.

Chapter 7

The experimental setup

This chapter is divided in two parts. The first one is a description of the cold neutron source SINQ (PSI, Switzerland) and the polarized beam FUNSPIN, followed by an overview of the neutron polarization measurement. The second part consists in a thorough description of the detector used to measure the parameters R and N. Particular attention is given to the sections concerning the hodoscopes and the device created to manipulate the calibration source, since their conceptions were part of the thesis work.

7.1 The Beam line

7.1.1 The neutron source: SINQ

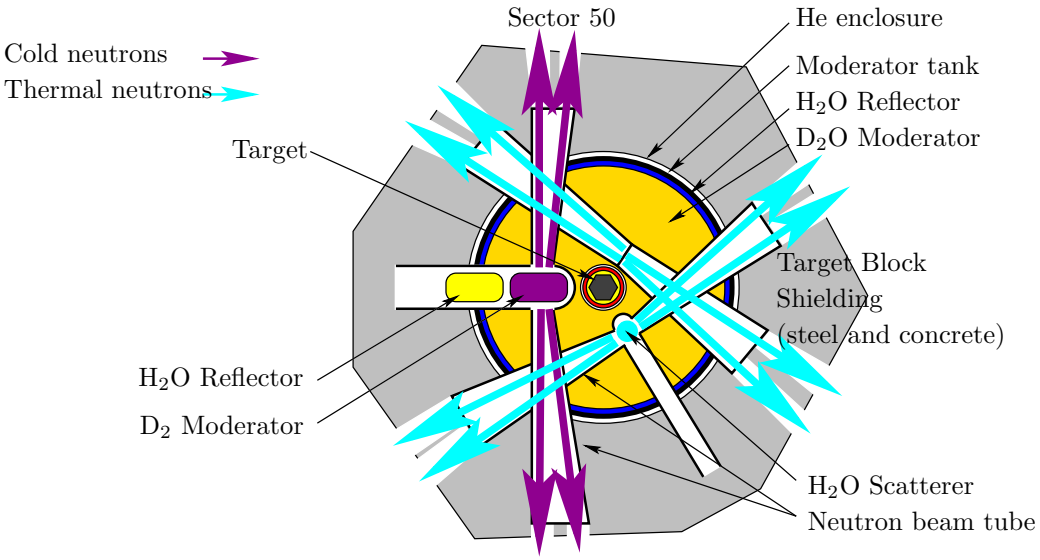

Figure 7.1: Horizontal cut view of SINQ

Constructed in 1996 at the Paul Scherrer Institute (PSI), SINQ is a spallation source. It is located at the end of the PSI proton beam line. The lead target (see Fig. 7.1)receives typically 1.2mA of 590 MeV protons [35]. It produces $(3-6)\times 10^{16}$ high energy spallation neutrons per second, moderated in a heavy water tank down to "thermal" energies.

Neutrons are extracted in horizontal inserts and, in our case, moderated once again by liquid deuterium (25K) to "cold" energies.

7.1.2 FUNSPIN

In 1999, a new neutron beam line was constructed in the sector 50 of SINQ, dedicated for fundamental physics with cold polarized neutrons [36].

7.1.2.1 Overview of the beam line

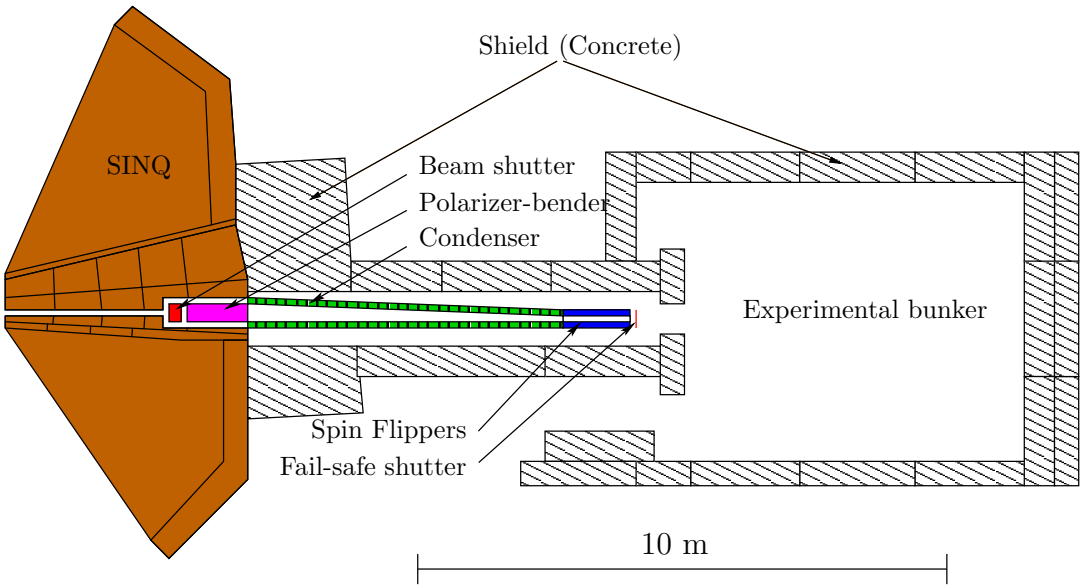

Figure 7.2: Schematic view of FUNSPIN.

A schematic view of the FUNSPIN beamline is shown on Fig. 7.2. The neutrons are extracted from the cold neutron source (D_2 moderator), and fly in a straight one-channel neutron guide up to the so called "polarizer-bender", described below. The polarized neutron beam is then spatially compressed in a 5.5m long condenser equipped with both magnetic and non-magnetic supermirrors[1]. Two radio-frequency spin flippers [37] are placed in the last 1.4m of the line. From the polarizer to the end of the beam line, a vertical magnetic field is used to keep the neutron polarization. The line, under vacuum, is closed by a 125 μm thick zirconium window. The fail-safe shutter is situated a few centimeters away.

7.1.2.2 The "polarizer-bender"

The polarizer uses 29 ferromagnetic supermirrors (CoFe/TiN and FeCo/TiZr) on which cold neutrons are reflected. This process has two components; a nuclear and a magnetic. The sign of the latter depends on the neutron spin orientation in the direction perpendicular to the incident trajectory and tangent to the supermirror surface. By a careful choice

[1]The vertical super-mirrors are magnetic in order to keep the neutron polarization whereas the horizontal ones are non-magnetic to prevent depolarization.

of the materials (nature and thickness), it is possible to produce destructive interferences between both components for one spin orientation and therefore reflect only the other one. The bend obviously increases the efficiency of the polarizer and allows in addition a good separation of the fast neutrons as well as a protection against the γ-rays coming from SINQ.

7.1.2.3 The dedicated collimator

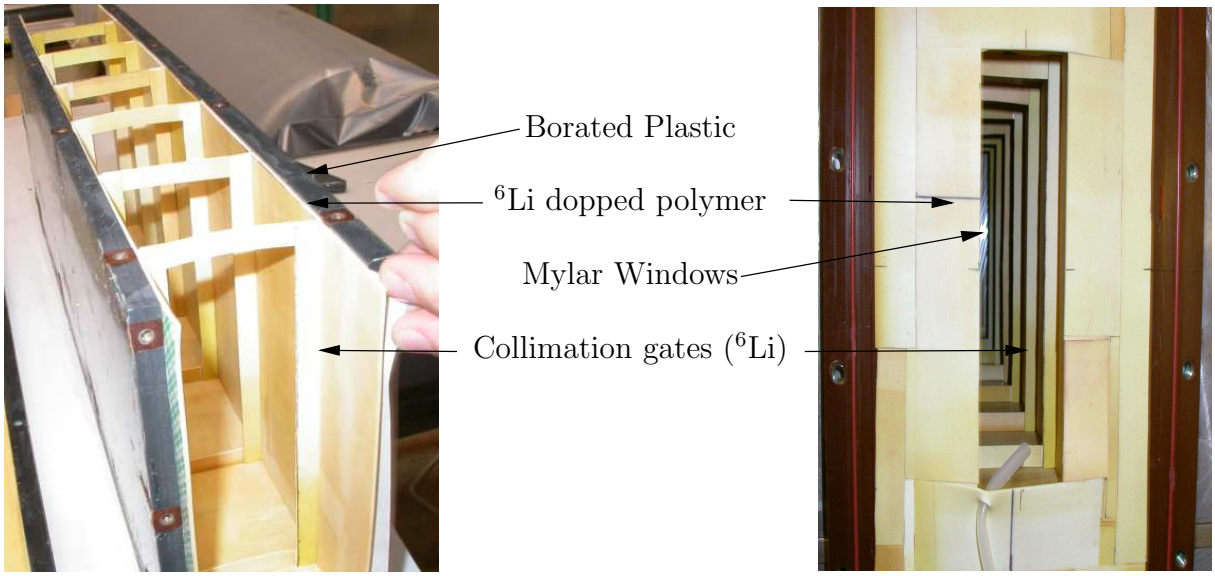

Figure 7.3: Two views of the collimator. Left: collimator open. Right: collimator in position. In the background, the Mylar window is visible. In the foreground, a portion of the flange covered with Li-polymer is visible. During normal operation it is tightly connected to the Helium Box.

Just behind the (open) fail-safe shutter, neutrons enter a collimator through a 2.5 μm-Mylar window. The collimator consists of a channel of borated plastic with a 1.2mm-thick layer of 6-lithium fluoride loaded polymer [38] (Fig. 7.3). Both borated plastic and Li-doped polymer are design to capture neutrons. The polymer linear absorption coefficient of this material is 28.5 cm^{-1} ($\lambda = 1.8$Å) with the reaction :

$$n +^6 Li \longrightarrow T + \alpha + 4.78MeV \tag{7.1}$$

Both tritium and α are heavy particles and are fast stopped by surrounding material. Therefore, they will not be detected and the neutron are efficiently absorbed without detectable background production[2]. The "gates", made also with that polymer, are designed to remove the diverging neutrons.

When the experiment is mounted, the collimator is filled with pure helium, and connected with the beam chamber described later. It is surrounded with an electromagnet producing a vertical magnetic field of approximately 15G to prevent a depolarization of the neutron beam.

[2]The emission of 3 γ per 10^4 neutron captures was considered negligible

7.1.3 Intensity and geometric properties of the neutron beam

The neutron beam was characterized twice. In 2001, by Schebetov *et al.* [36, 34] and in 2003 by our collaboration. The full description and the results can be found in Ref. [39].

7.1.3.1 Distribution of the beam intensity

The intensity of the neutron beam is proportional to the current of the proton beam received by the spallation source target. Therefore the neutron flux will be quoted per 1 mA of the proton beam current. The typical proton beam intensity during 2003 and 2004 was 1.2mA. The neutron beam intensity was measured using irradiation method. Thin gold foils ($\sim 10\mu m$) with a diameter of 25mm were placed few centimeters behind the fail-safe shutter and irradiated for few minutes. The time of irradiation was defined by the opening and closing of the shutter with an accuracy of 1s. Because the cross-section for cold neutron capture is proportional to the reciprocal of the neutron velocity, and the gold foils are almost transparent to the neutron beam, the measured activity of ^{198}Au is directly proportional to the spatial neutron density.

The characteristics of the neutron beam are:

- Cold neutron spatial density $\rho_0 = (2.95 \pm 0.04) \times 10^3$ cm^{-3}mA^{-1} (center of the beam).
- Neutron flux density $\Phi = (2.46 \pm 0.04) \times 10^8$ cm^{-2}s^{-1}mA^{-1}
- Thermal-equivalent flux $\Phi_{eq} = (6.49 \pm 0.10) \times 10^8$ cm^{-2}s^{-1}mA^{-1}

These values are significantly higher than the ones measured in 2001 [36, 34]. It can be explained by the upgrade of the SINQ target in spring 2003.

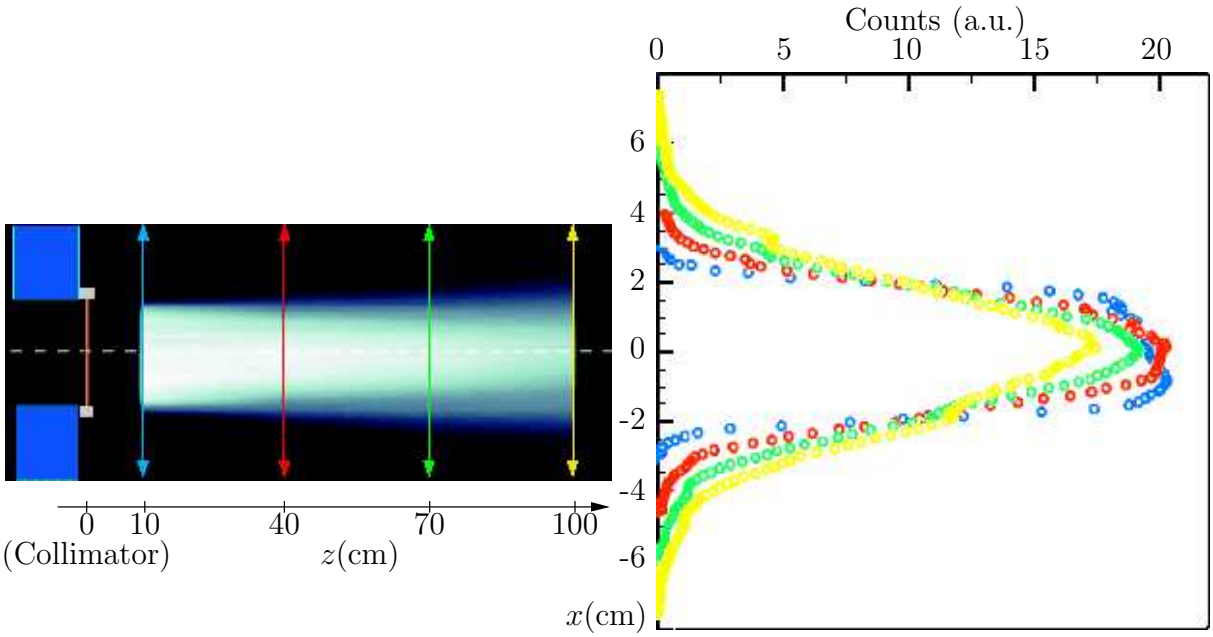

Figure 7.4: Horizontal divergence of the neutron beam obtained with irradiated gold foils set at several places along the z-axis. $z = 0$ corresponds to the end of the beam line [34].

This method can also be used to study the divergence of the neutron beam. It is an important issue since the neutrons can activate the surrounding of the beam, producing an important background of charged particles. The shape of the beam was then measured at several places after the failsafe shutter (Fig. 7.4).

One can notice that the beam is not perfectly collimated. Its divergence was calculated to be 0.8° [39]. The vertical divergence was estimated to be 1.6° (upward) and 1.3° (downward). These measurements were performed before the construction of the collimator and no additional tests were done since. The detector for the measurement of the R-parameter is set typically between 55 cm and 105 cm after the end of the collimator; the beam width can be assumed to be less than 10 cm in total (5cm FWHM).

7.1.3.2 Wavelength distribution of the beam intensity

The wavelength distribution was determined using a time-of-flight method [39]. A chopper creates a burst of neutrons, detected by a ^{3}He detector located 1.7m downstream. Every 10 ms the chopper opens and simultaneously a "start" signal is sent to the Multiscaler Analyzer (MAS). The pulses from the neutron detector are counted in the corresponding times channels (511 channels of 17.5 μs wide). The whole apparatus is placed just after the end of the collimator. The results are shown on Fig. 7.5.

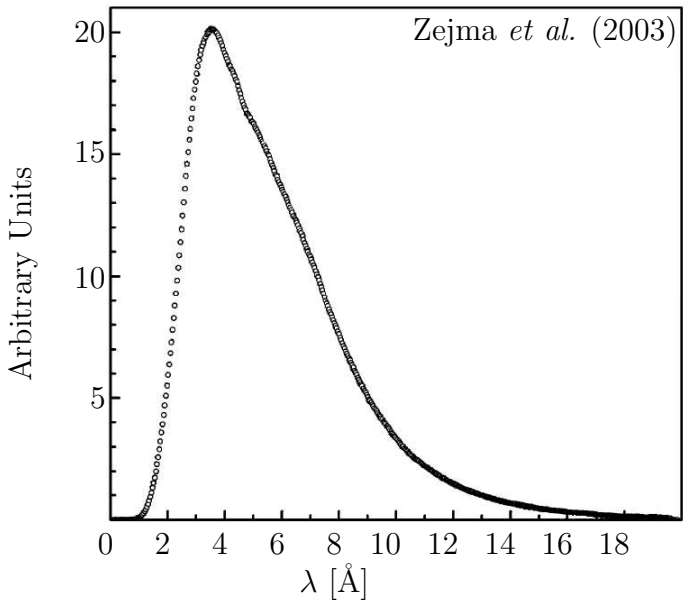

Figure 7.5: Wavelength distribution of the neutron beam. The measurement was made in the middle of the beam [39].

7.1.4 Polarization measurement

In 2003, a new polarization measurement was performed before the R-parameter measurement. Full results and discussion can be found in [39]. The main conclusions about the polarization measurement are:

- The polarization in the center of the beam is larger than 95%.

- The average polarization over the whole beam cross section is $(89.75 \pm 0.01 \pm 1.0)\%$.
- The spin flippers efficiencies are very close to 100%.

7.2 Experimental setup

7.2.1 Overview of the complete setup

The status of the setup by mid-2002 is shown on Fig. 7.6. The volume filled with helium where the beam is located, one large MultiWire Proportional Chamber (MWPC) and one scintillator wall had been already built. The MWPC was a simplified prototype compared with the final configuration. The existing hodoscope wasn't satisfactory enough to be duplicated for the other side. Instead it was decided to be completely redesigned for the new setup.

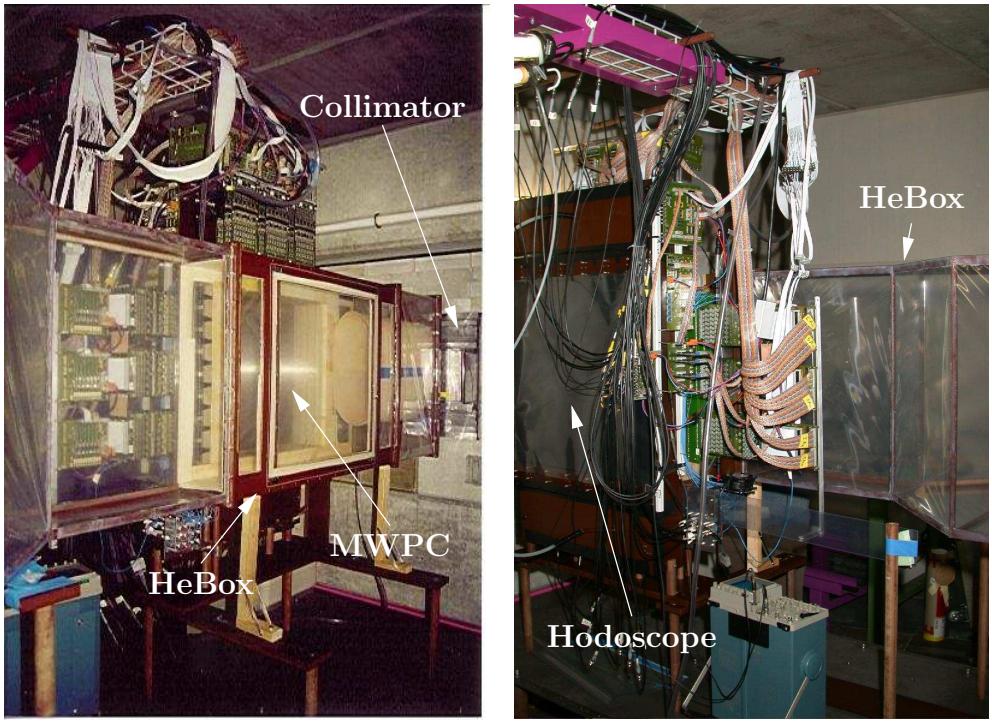

Figure 7.6: View from both sides of the setup (mid-2002)

A surrounding magnetic structure was added in the middle of 2002. It creates a vertical field guiding the neutron spins through the whole setup.

The current experimental setup can be seen on Fig. 7.7. The beam is now surrounded by a pair of symmetrical detectors. Each of them consists of a tracking detector (MWPC), a volume containing the Mott scatterer and a scintillator wall. The whole is sitting inside a magnetic structure producing a 10G vertical magnetic field. This field prolongates a similar field present in the collimator and in the beam line and keeps the neutron beam polarization.

Except for the hodoscopes, developed in 2003, and the DMCS (Device for the Movement of the Calibration Source), added after the commissionary run in 2003, all the

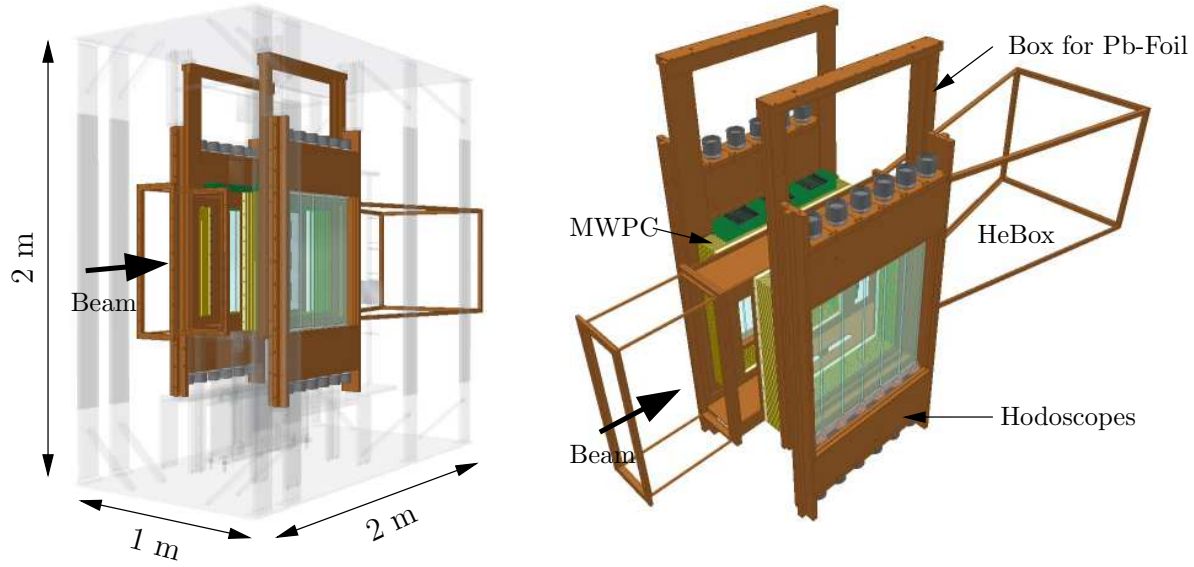

Figure 7.7: Two views of the experimental setup. Left: the magnetic structure around the setup (shaded) keeping the polarization of the neutrons. Right: the "sandwich" is visible ; from center to side, one can see the HeBox, the MWPCs (in yellow and green), the box containing the Pb-foils and the hodoscopes.

additional parts where under construction or ready to be installed at the beginning of 2003:

- the last part of the HeBox was enlarged to take into account the divergence of the beam and to reduce the background.
- the second MWPC was mounted, and the first one completed.
- the boxes for the Pb-Foils were mounted and connected to the MWPC.
- the Pb-foils were under development.
- the electronics for acquisition was ready to be used.

7.2.2 Requirements

The requirements can be sorted in two parts. Firstly, the electrons emitted by the neutron β-decay have a rather low energy[3]. Thus, the energy losses along their path in the detector has to be minimized. Secondly, the cold neutrons have a high probability to be scattered or captured by any surrounding material, and thus to produce background. This effect, although unavoidable, must be kept as low as possible.

In order to fulfill these requirements, the experimental setup was built as light as possible, using low-Z materials.

Additionally, the ferro-magnetic materials were prohibited since they disturb the guiding magnetic field.

[3]End-point 782 keV

7.2.3 The Helium Box

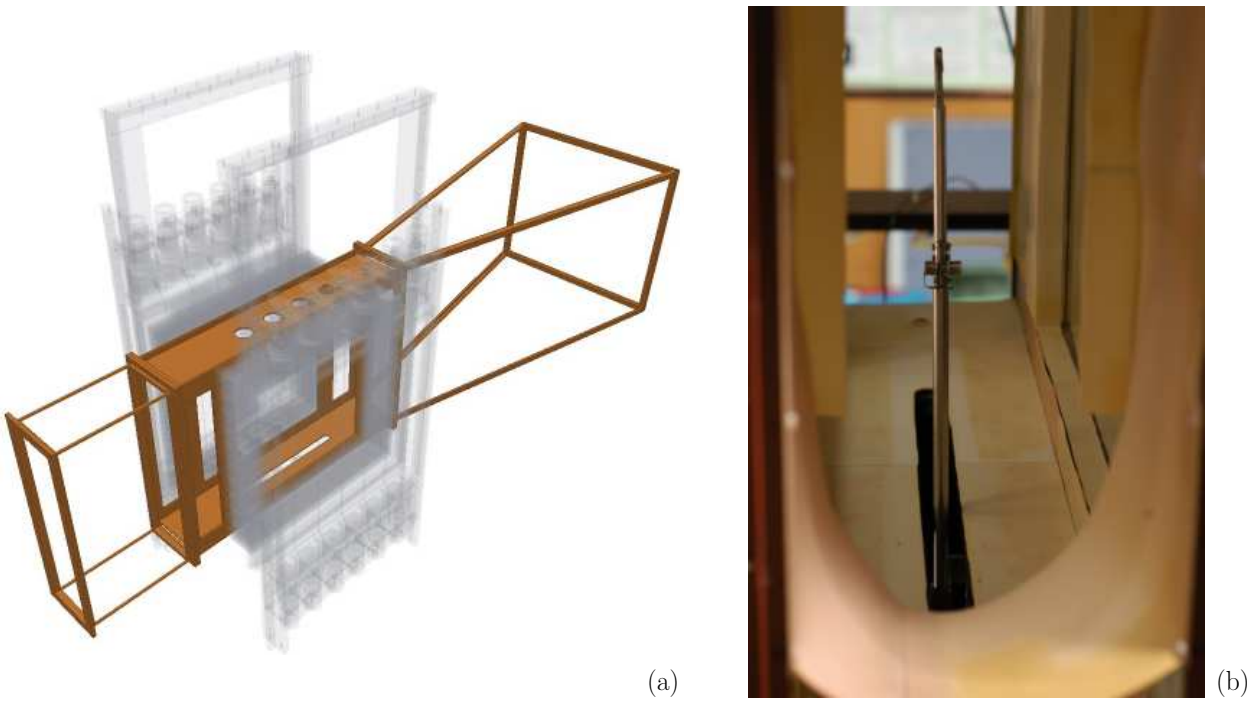

(a) (b)

Figure 7.8: HeBox: the resocel skeleton (a) and view of the inside from the collimator (b).

The "HeBox" (Fig. 7.8(a)) is the volume in which the neutron beam is transported. It consists of a light skeleton of resocel covered with $100\mu m$ Mylar foils. Once connected to the collimator (Fig. 7.3), the whole volume is tight. The inner part is covered with a 1.2mm-thick layer of 6-lithium fluoride loadedpolymer, visible on Fig. 7.8(b).

In order to reduce the neutron scattering (and thus the activation of the surrounding), there must be as few material as possible inside the HeBox, ideally vacuum. Unfortunately the thin windows of the chambers, together with the necessity to keep a good acceptance of the detector (large windows) forbid this solution. Therefore He at atmospheric pressure was used in this volume. Since it is difficult to guarantee the absolute tightness of such a light enclosure, it was decided to keep a constant flux of gas, injected through the collimator and going out at the bottom of the setup.

The last part of the HeBox is the beam dump section (Fig. 7.8(a)). It consits in a 1.3 m diverging box covered by ^{6}Li polymer. At the end of the HeBox, 4 layers of polymer stop the beam. Simulations show that in this way, neutrons reflected from the beam stop cannot increase the neutron flux between the detectors more than 10 ppm.

7.2.4 The MultiWire Proportional Chambers

7.2.4.1 Description

In order to measure the Mott asymmetry one must track the electrons before and after the scattering on the Mott scatterer. The tracking process itself should not disturb

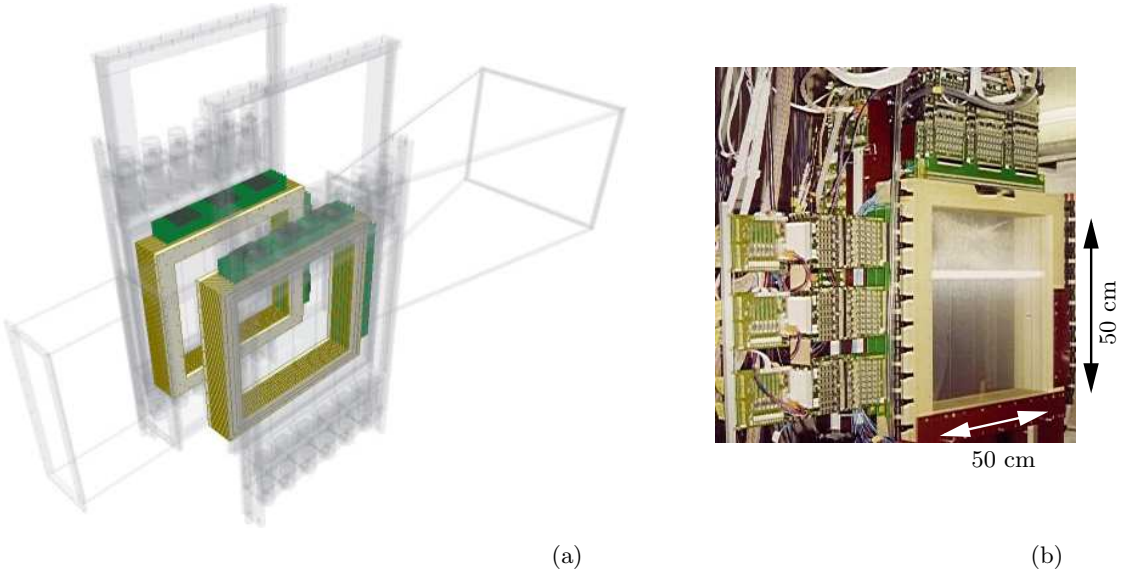

Figure 7.9: MWPC: place in the detector and view from the beam side

significantly the electrons, especially their momentum and their energy. A gas detector was built using thin wire electrodes, since foil planes would lead to multiple scattering of the electrons. Again, the gas mixture of the detector is based on He. The concept of the detector and the associated electronics were tested on a prototype (K-Prototype) in 2000 [40].

The MWPCs presently in use (Fig. 7.9) were developed in 2001 as "M-prototype" by the

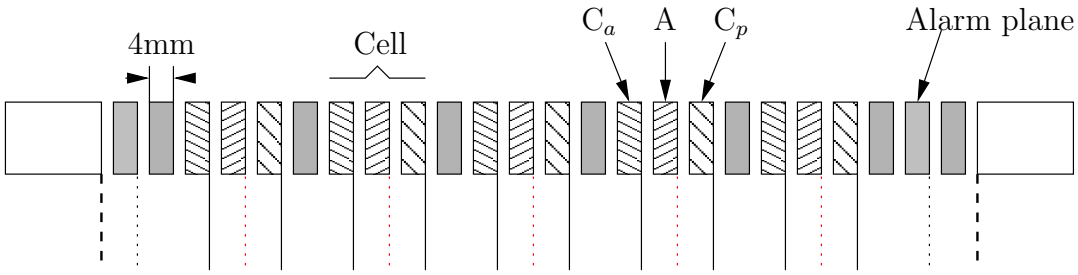

Figure 7.10: MWPC: Scheme of the position of the electrodes. Each anode plane (A) is placed between one active cathode plane (C_a) and one passive cathode plane (C_c).(not to scale)

team of the Jagiellonian University (Krakow). A full description can be found in [34]. The external dimensions of the MWPC are 625×625 mm^2 for an inside opening of 505×505 mm^2. Each MWPC consists of five active cells with a 4 mm separation (Fig. 7.10). A cell consists of one anode plane (horizontal wires) between two cathodes planes (vertical wires). Since one cathode plane is active, electrons can be tracked both in the vertical and horizontal planes.

The wires are made of Ni/Cr alloy (80/20%) with a 25μm diameter. They are set on the frames with a 0.05 N tension. Each anode plane consists of 96 wires spaced out by 5 mm and two additional 100μm field wires on both side. The cathode planes are made of 198 wires separated by 2.5 mm. The charge distribution on the cathode wires is large

and the spatial resolution cannot be better than 5 mm. Therefore, the cathodes wires are connected in pairs to increase the pulse height and reduce the number of electronic channels. A horizontal mesh of wires with a low voltage ($\sim$ 20 V) is added at both ends of the chamber in order to provide an alarm and an emergency shutdown in case of a deformation of the Mylar windows.

The gas used is a mixture of (in volume) 90% of Helium, 5% of Isobutane and 5% of Methylal (Dimethoxymethane $C_3H_80_2$). The typical voltage of the anode is 1800 V.
The chambers windows are made of 2.5 μm Mylar and their dimensions are 505×505 mm^2.

7.2.4.2 Flaws and improvements

Up to now, two full runs were performed with the chambers: one month in fall 2003 and three months at the end of the summer 2004. During the last week of the first run, the closest plane to the beam in one chamber was unable to hold more than 1500 V and some breakdowns occurred on the other planes. It was decided to open the chambers for inspection before any new run. Several wires were not as tight as expected: the tension should have been around 0.05 N and was less than 0.03 N. Aging effects were also noticed on wires: a "shadow" of the cathodes was visible on the anodes wire. With a stereomicroscope, the modification of color wasn't visible, but some particles of metal sticking on the wire were found (Fig. 7.11). It wasn't possible to remove them. Thus

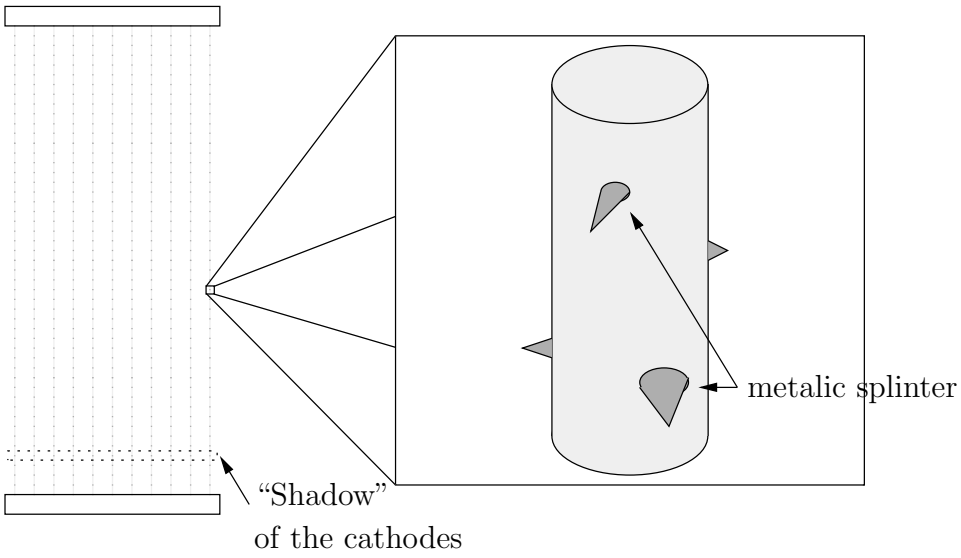

Figure 7.11: MWPC: Layout representing the aging effects discovered in the MWPC in 2004. A shadow of the cathodes was visible on the anodes, and some small particles of metal were sticking to the wires.

these wires had to be replaced.

7.2.5 The lead foils

As seen in Eq.(6.10), the cross section of the Mott scattering is directly related to the atomic number of the target material. Thus, the scattering target is built with high Z-material. Despite the possibility of oxidation lead was preferred to gold.

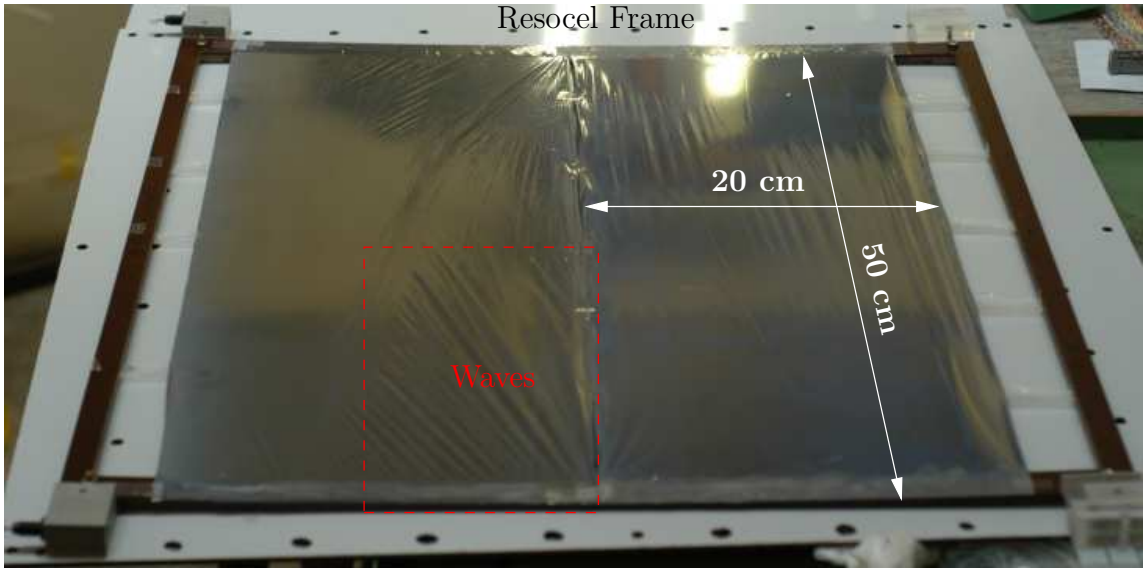

Figure 7.12: View of one Mott target, called "Pb-Foil". One can notice the "waves" produced by the tension on the foil.

Another important point concerning the Mott target is its thickness: it results from a compromise between the probability of scattering and the probability of multiple scattering. It is indeed impossible to distinguish them experimentally, so the multiple scattering proportion must be evaluated using simulations.

Technically, the Mott target consists of two foils of 500×200 mm^2 stretched on a resocel frame (Fig. 7.12). Each foil is a layer of 1μm of lead, evaporated on a 2.5μm Mylar foil. The inhomogeneity of the lead, measured by absorption of α particles is lower than 10%. As one can notice on (Fig. 7.12), one of the difficulties was to stretch the foils without creating waves, since they produce unknown modification in the effective thickness of the Pb-foils.

7.2.6 The hodoscopes

The scintillator walls have three purposes :

- the measurement of the energy of the electrons.
- the trigger of the acquisition.
- the generation of a veto on the side of the vertex.

The hodoscopes were developed using several prototypes. At the end of 2002, one scintillator wall was made with six slabs of 600×100×10 mm^3 plastic scintillator (Bicron B405), chosen for its fast response together with its acceptable energy resolution. The effective area was 500×500 mm^2. The light was collected at both extremities of each scintillator with a photomultiplier (PM) XP3330 from Photonis. Each slab was wrapped with a layer of diffusive material (Teflon) and a layer of Pokalon (100μm-thick black polymer) to protect the scintillator against light. The support structure of the hodoscopes was made of resocel (Fig. 7.13).

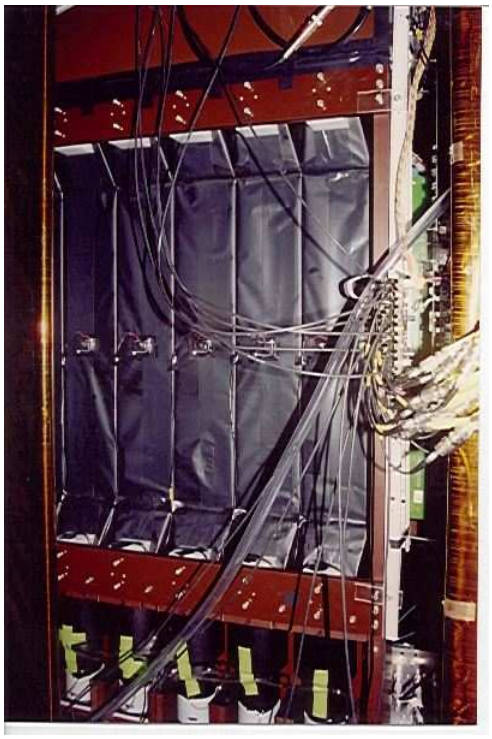

Figure 7.13: Hodoscope at the end of 2002. The bottom part is open and the PMs are visible. One slab is hidden by the magnetic leg.

On each slab, a LED was fixed at middle height, delivering a periodic signal of three different amplitudes (10 signals of each amplitude per second). It was used to monitor any change in the gains and the offsets of the PMs.

A constant flow of air was brought inside the magnetic shield of each PM: the XP3330 are made with borosilicate glass, porous to Helium and this flow prevents any concentration of helium around the PMs.

At the end of 2002, two problems were identified in this design:

- The magnetic shield around the PMs was not sufficient
- The signal amplitude was strongly dependent on the position of emission in the scintillator.

7.2.6.1 Calibration source: ^{207}Bi

A source of ^{207}Bi was used both to perform tests on the scintillators and during the data acquisition to calibrate the hodoscopes. This isotope decays to ^{207}Pb by electron capture with a period of 38 years. The internal capture is followed by an internal conversion and electrons with very well defined energies are emitted (Tab. 7.1).

The resolution of the plastic scintillators does not allow a good separation of the energies and the spectrum of the Bi source is similar to the one created by two energy lines: 503 keV and 995 keV.

The mechanical characteristics of the source are summarized in Tab. 7.2. The sample of radioactive material is kept between to thin foils (2.4 mg/cm^2) of Titanium, hold in a ring of Aluminum.

Energy (keV)	Electrons per 100 disint.
5-16	53.8
56-62	
68-75	2.8
80-88	
482	1.52
554-557	0.44
566-567	0.15
810	0.003
976	7.03
1048-1051	1.84
1060-1061	0.54
1682	0.02

Table 7.1: Energies and relative intensities of the electrons emitted by the ^{207}Pb created in the decay of the ^{207}Bi [41]. The red values are the energies used in our experiment

External diameter	25 mm
Thickness	3 mm
Diameter of the active deposit	5 mm
Nominal activity	37 kBq

Table 7.2: Physical characteristics of the ^{207}Bi source.

One should notice that this source is not collimated; this point is important since it allows the calibration of both hodoscopes simultaneously.

7.2.6.2 Magnetic field shielding

The μ-metal shield of the XP3330 was not sufficient. When the guiding field was ON (10G, vertical), 70% of the signal was lost despite the addition of μ-metal around the hodoscopes. The problem came from an inadequate configuration: not only the PMs are very sensitive to a magnetic field colinear to their axis of revolution, but also the magnetic shield is the least efficient in this configuration. The problem is particulary obvious if the edge of the PM, just behind the photocathode, is not protected.

In order to solve this problem, the influence of the position of the μ-metal shield on the PM was studied with the setup described in Fig. 7.14. The system was placed within the magnetic field generated by the electromagnet used in the experiment: a vertical field of 10G. One can notice that these conditions are worse than the ones really applied to the photomultipliers during a usual run: in operation, the PMs are more on side of the magnetic structure where the magnetic field is not vertical. The vertical component is thus smaller than 10G. The results of the test are show on Fig. 7.15.

The position of the shield at 3 cm before the photocathode was considered as acceptable: less than 5% of the full signal is lost and the geometry of the light guide does not need too much modifications.

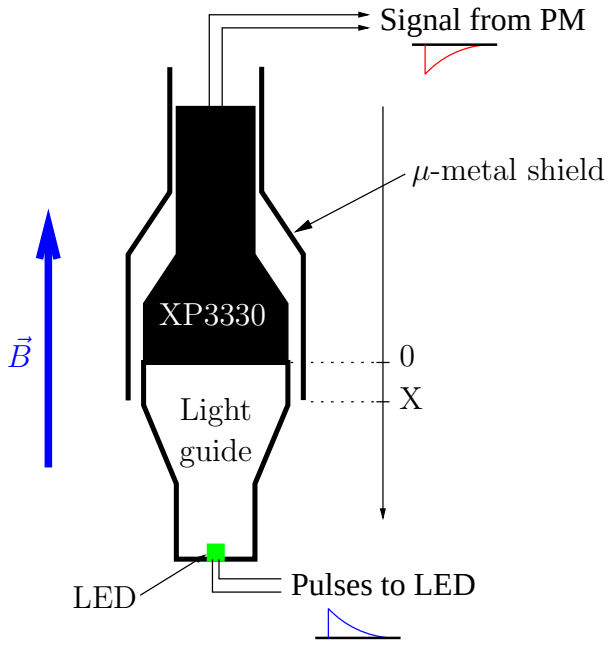

Figure 7.14: Scheme of the setup built to measure the influence of the magnetic shield position upon the signal delivered by the photomultipliers. This system was placed in the middle of the magnetic structure used for the experiment, creating a 10G vertical magnetic field.

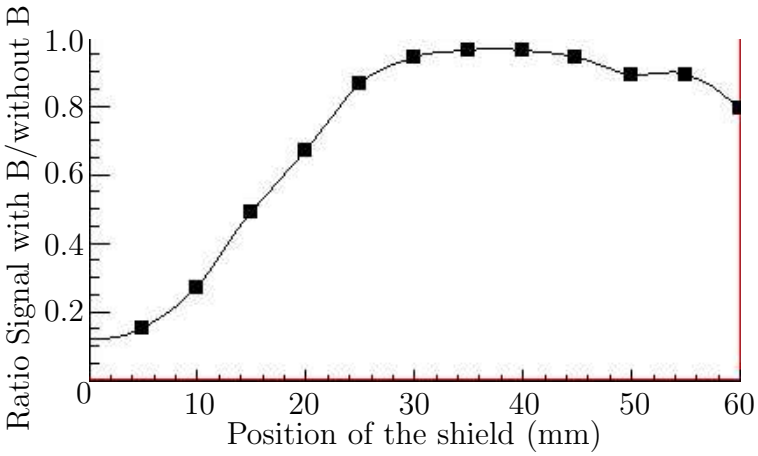

Figure 7.15: Influence of the position of the magnetic shield on the signal delivered by the photomultiplier. The "position" correspond to the distance between the edge of the magnetic shield and the edge of the PM (photocathode). A positive position indicates that the shield is partly around the light guide. The normalization is made with the signal delivered without magnetic field.

7.2.6.3 Scintillator wrapping

One scintillator was dismantled and carefully investigated. The first observations, with wrapping still around, showed that the scintillator transparency was not very good. Teflon was sticking on the scintillator, deteriorating the conditions of total reflection. The light attenuation of such setup was compared with similar ones using aluminized Mylar and

without wrapping, using the system described on Fig. 7.16: the ^{207}Bi source was placed on a 1 mm-thick plastic scintillator coupled to a fast PM. The whole system was moved over the scintillator length. The signal given by the fast PM was used in coincidence with the signal delivered by the XP3330. This method allows a good discrimination of the background. Because of the use of the thin scintillator, it is not possible to detect the low

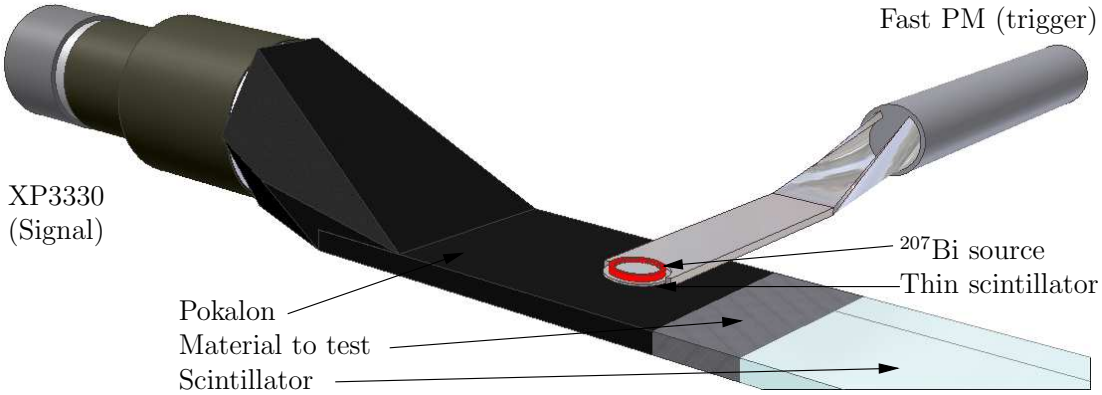

Figure 7.16: Experimental setup used for the wrapping comparison. The Bi source was placed at different position on the slab. In order to suppress the natural background, an additional thin scintillator was used as an active collimator : signal coincidence from both PMs was used as a trigger.

energy line when the source is further than 30 cm from the XP3330. Thus, the analysis was done using the high energy line of the source, and the results are shown on Fig. 7.17.

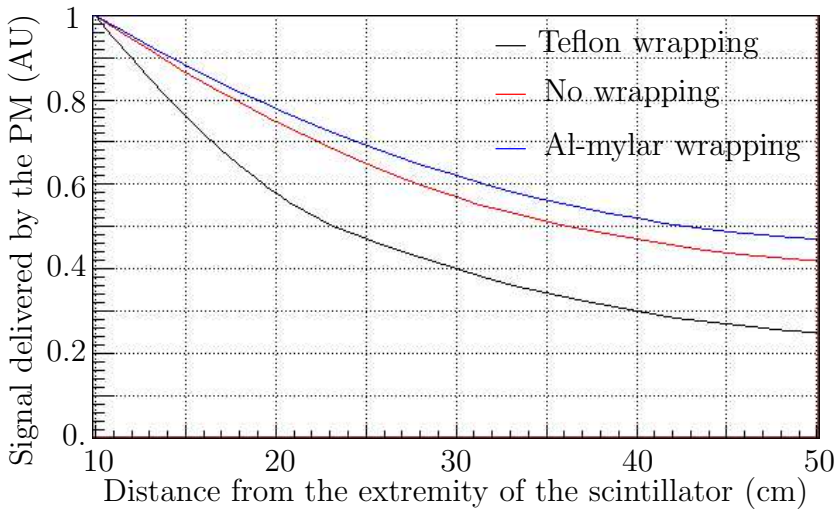

Figure 7.17: Variation of the signal amplitude vs position of emission in the scintillator for several scintillator wrappings. The signal is normalized to the the position x=10 cm. For all cases an additional layer of Pokalon is used for light tightness.

Without any doubt, the Mylar allows a better light collection than the Teflon. In addition, since it is much thinner, this material is better for electron detection because

it minimizes the energy losses. However, a problem may arise: aluminum may be activated by neutrons and produce a significant background on the scintillators. A careful comparison between scintillators wrapped either with Teflon and aluminized Mylar was performed. No sensible difference was observed between the background detected by each scintillators after being exposed to the neutron beam. The aluminum activation was then assumed to be negligible.

7.2.6.4 Light guide

The light guides used in 2002 were designed with a 5 cm-long step in order to strengthen the connection and improve the light collection (see Fig. 7.18(left light-guide)). On this setup the whole length of the scintillator was used for electron detection, and when the light emission was localized close to the step the light collection was much more efficient. In order to test this effect, one light guide was cut to reduce the step to 1 cm and put back on the end of the scintillator Fig. 7.18(right light-guide)).

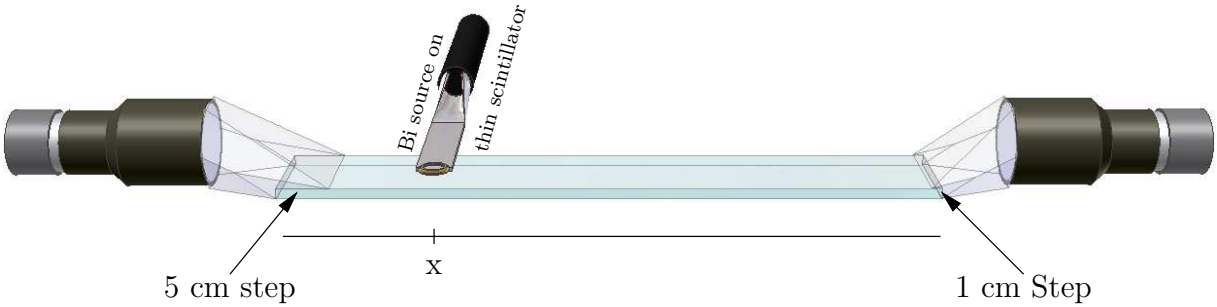

Figure 7.18: Experimental setup used for the light guides comparison. The Bi source was placed at different position on the slab. Again, the coincidence with an additional thin scintillator triggers the acquisition.

A setup similar as the previous one (Fig. 7.16) was used (Fig. 7.18) and the results are shown on Fig. 7.19. The variation of the signal amplitude with the position of light source in the scintillator is smoother with the new configuration. In order to improve a little bit more the setup, the new scintillators were made 3 centimeters longer. Thus the last part of the scintillator close to the light guide is not used for electron detection.

7.2.6.5 Current hodoscopes

The present setup is shown on Fig. 7.20.

It consists of six slabs of 100 mm wide and 10 mm thick[4] plastic scintillators (BC405). Each is 630 mm long, although only a global 555×555 mm^2 window is effective. Each slab and the coupled light guides are wrapped with aluminized Mylar, both for the light collection and to isolate from each other. Two PMs (Photonis XP3330) collect the light from both sides of a slab. Figure 7.21 represents the ^{207}Bi spectrum obtained by this setup. The energy standard deviation in the range $200-1000$ keV varies between 40 and 70 keV [42].

[4]The thickness of the scintillator was chosen to measure the electron energy up to 2 MeV.

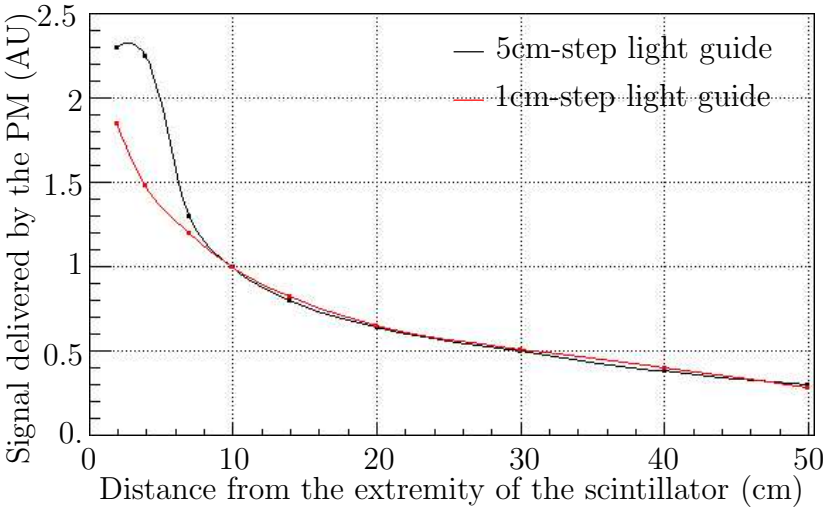

Figure 7.19: Variation of the signal amplitude vs position of emission in the scintillator for a light guide used in 2002 and a modified one. Both signals were normalized to the position of emission 10 cm away from the extremity of the scintillator on the side of the corresponding PM.

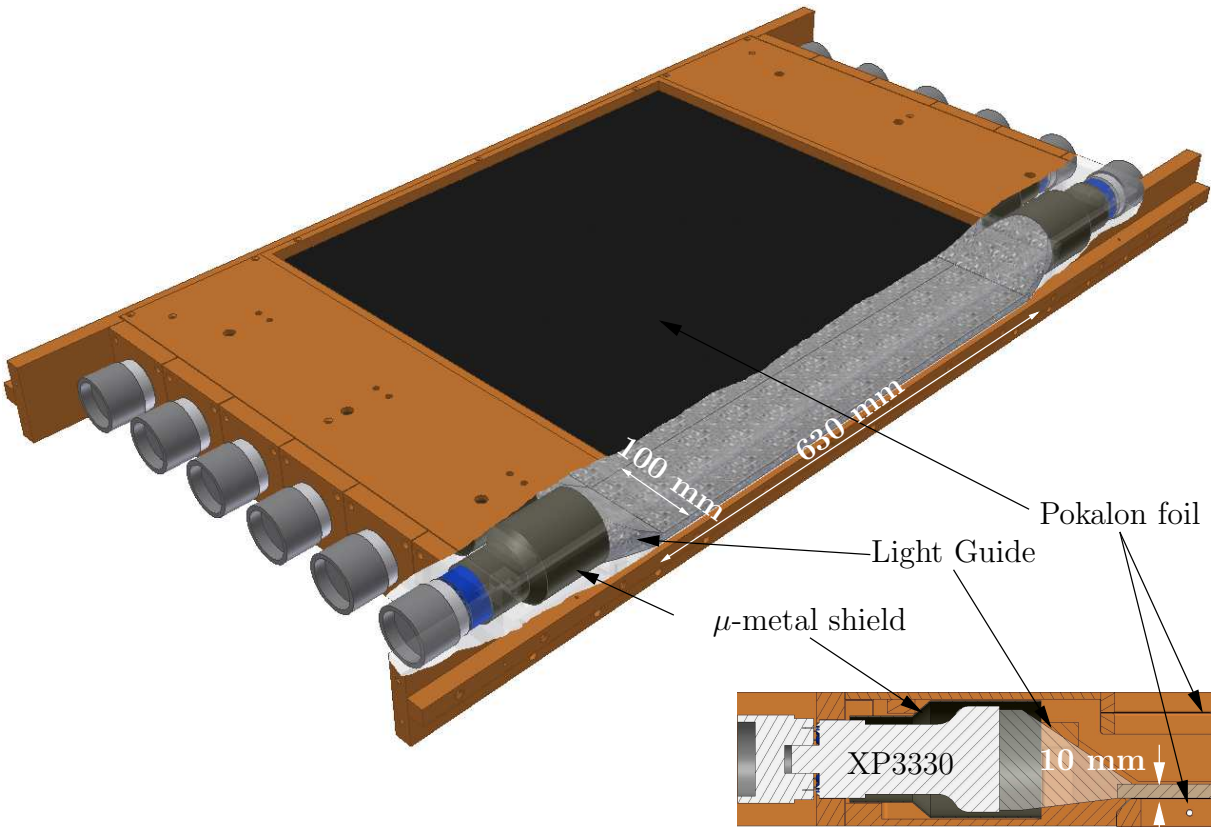

Figure 7.20: View of the current hodoscope. The box is partially open and one scintillator is visible.

The box containing the scintillators and the PM is light-tight and mainly built with resocel. Two Pokalon windows are placed before and behind the scintillators: one in order

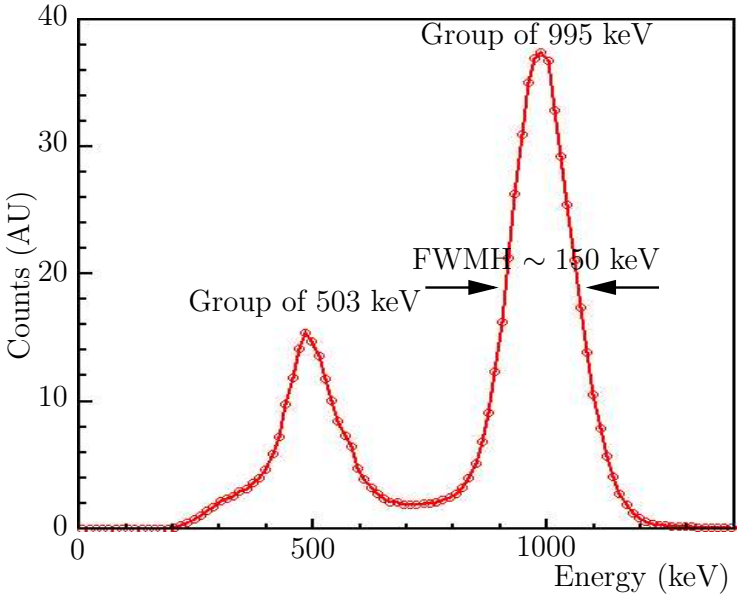

Figure 7.21: Measured spectrum of the ^{207}Bi calibration source. For the 995 keV Group, the Full Width at Half Maximum is around 150 keV which corresponds to a standard deviation of 64 keV [42].

to reduce the energy losses for the electrons and the second one to prevent back-scattering of high energy electrons.

A LED is placed on each slab in order to monitor any modification of the photomultipliers output. The flow of dry air was also implemented to this new setup.

7.2.7 The DMCS (Device for the Movement of the Calibration Source)

The calibration of the scintillators is performed with the ^{207}Bi source. The best place to set this source is inside the HeBox, on the plane $x = 0$ which corresponds to the theoretical plane of symmetry of the experimental setup (see Fig. 6.7). The coincidence between the chambers and the hodoscopes allows a good rejection of the natural γ-background during the calibration runs, and the information about the trajectory give a more precise definition of the detected energy. However, the calibration source must be removed, or at least hidden from the sight of the detector when it is not needed, and this operation should not require an opening of the HeBox.

Additionally, a better calibration of the scintillators would be achieve with the source placed at different positions in the HeBox.

These points led to the conception of a device able to manipulate the calibration source whose physical characteristics are summarize in the Tab. 7.2.

This device had to fulfill the following requirements:

- The source can move within a window of 400×400 mm^2 centered between the MWPCs. The idea was to cover this area as homogeneously as possible.
- When the source is not needed it is removed or parked in such a way that it has no influence on the measurements.

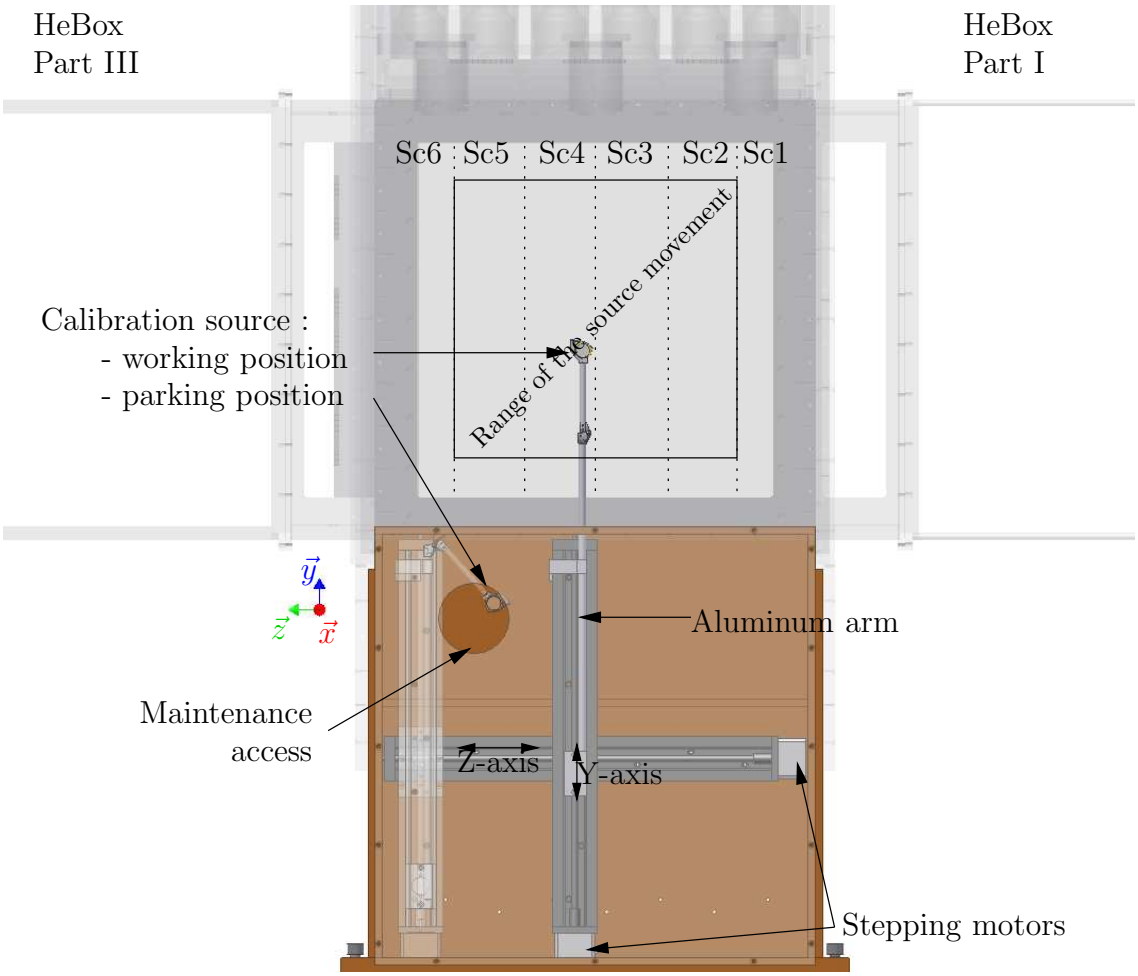

Figure 7.22: DMCS: Side view of the device under the HeBox. In shaded, the source is in the parking position.

The result of this development is visible on Fig. 7.22. The active part of the device is a pliable arm made of aluminum. It is moved along the z- and y-axis by two linear actuators using stepping motors. The system is placed in an He-tight box made of resocel with a transparent Plexiglas side. A hole was made in this frame in order to access the source for maintenance purposes. In normal operation, it is tightly covered by a thick Mylar foil. The whole is mounted below the HeBox and the calibration source is moved through a 4×45 cm^2 slit (visible on the Fig. 7.8). Since the DMCS became the lowest part of the setup, the He-output was moved from the bottom of the HeBox to the bottom of the device.

The initial idea was that the source would be left in the parking position when it was not needed. It was soon discovered that even in this position, it was still visible from the detector. It was then decided to remove it after each calibration run. Since it was necessary not to loose too much helium during the process, a kind of Mylar glove was adapted on the maintenance opening, filled with He before the procedure.

The movement of the calibration is controlled by a command/control created under LabView. It is possible to either control manually the position of the source or to program a path within the movement range. The maximum movement speed is set to 10 mm/s.

No matter which method is used, the operator can check the real-time position of the source, with a better precision than 5 mm.

7.2.8 Electronics subsystems

The electronics around the experimental system can be split into several subsystems, as shown on Fig. 7.23.

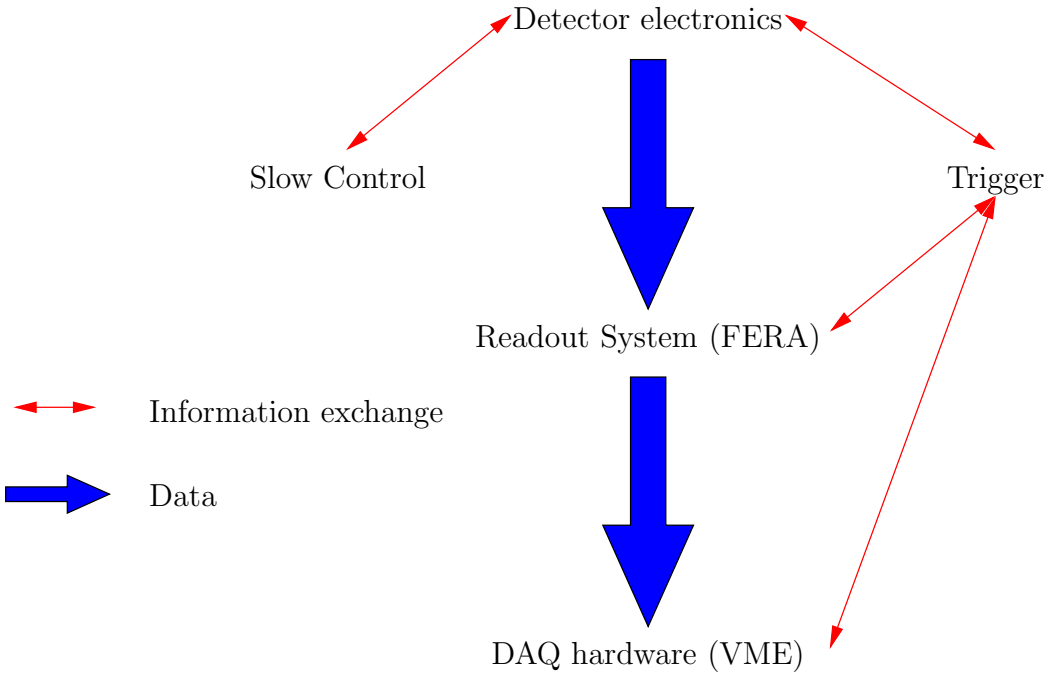

Figure 7.23: Overview of the electronics subsystems

7.2.8.1 Detector electronics

The electronics system of the MWPC was created for the prototype detector [34, 40]. The wire signals are amplified, shaped and discriminated. The logical signal is then delayed by 400 ns relatively from plane to plane and sent to TDCs. The signal is thus analogically multiplexed and the total number of digital channels necessary for two chambers is reduced from 1920 to 384. A time analysis with respect to the reference signal delivered by the fast trigger circuit allows a rough pulse height evaluation, useful in the cluster centroid reconstruction.

The 24 individual photomultiplier signals are first split in analog fan-outs. One branch is fed to the fast trigger circuit after discrimination and additionally a time measurement with respect to the fast trigger reference is performed for all individual PM's. The second branch is delayed and sent to charge sensitive ADCs. One should note that the hodoscopes operate at high count rates ($\sim 10^6$ per second) so that time information is necessary for the reduction of random coincidences.

7.2.8.2 Fast trigger

Under experimental conditions the background radiation consists of scattered neutrons, secondary γ-rays and electrons. This requires the inclusion of the information from the wire chambers in the event selection process. Thus, the trigger has two levels. The first step is activated by a signal from any photomultiplier. It provides a time reference and opens a 1 μs-gate. During this time, the information from the chambers and from all the other PMs are read and the plane multiplicities are compared with the thresholds set by the operator. If the conditions are fulfilled in one chamber (both electrodes) and a signal is provided by one PM on this side, the trigger will sort the event as a "Single Track". If the conditions are fulfilled in both chambers, it becomes a "V-Track"[5]

7.2.8.3 Readout and DAQ systems

All pulse digitizers used in the experiment are FERA compatible. The main stream of data is transported over the FERA bus, derandomized in two VME hosted triple port memory modules and logged onto a DLT device under control of a RIO2 controller running the LynxOS real-time operating system. Data buffer management and monitoring utilities are performed with the MBS[6] data acquisition software controlled from a PC running a Linux operating system.

The data gathered were recorded via SCSI on 35GB DLTs and then duplicated and stored on the PSI archive system [43], accessible from FTP (archivftp.psi.ch).

7.2.8.4 Slow control

The Slow Control is threefold:

- Control of the HV power supply (MWPC and PMs)
- Setting of all the thresholds used by the electronics boards
- Control of the calibration source motions

For each point, a feedback is provided to the user. The slow control is running on an industrial PC and programmed with the LabView graphical language.

7.3 Overview of the 2004 Run

The run performed in 2004 aimed at the measurement of the R parameter with the precision of 10^{-2}. It is thus a first step towards the final precession of $5 \cdot 10^{-3}$. It took place between the 01/08/2004 and the 26/10/2004.

7.3.1 Typical rates of acquisition

The table 7.3 summarizes the typical acquisition rates during the run 2004. For comparison purposes, the rate of "Single Tracks" given by the trigger is also indicated. During the run 2004, these potential Single Track events were prescaled, usually by a factor 2.

Type	Typical Rate (/s)	
	Detector 0	Detector 1
ST (scalers)	10000	8000
VT (scalers - Foil IN)	700	600
VT (scalers - Foil OUT)	500	500
VT (reconstructed -Foil IN)	0.12	0.15
VT (reconstructed -Foil OUT)	0.08	0.12

Table 7.3: Acquisition rates during the run 2004 corresponding to a proton beam current of 1.2 mA.

Considering the direction of the neutron beam, the detector 0 and detector 1 are localized on the right and on the left respectively. It is interesting to see that although the rates are higher on the detector 0, the reconstruction is better made with detector 1.

7.3.2 Computing and storage

It was decided at the beginning of the run to split the data in 1GB files, which correspond to ∼25min of acquisition time under normal conditions. Of course, this length is very dependent to the beam intensity and to the prescaling of the Single Tracks. During the run 2004, about 3000 files were recorded.

7.3.3 Procedures

7.3.3.1 Calibration

The run took advantage of the weekly shutdown of the proton beam for maintenance. Therefore, this day was used for the scintillator calibration. The Bi source was installed on its support and slowly moved between the two chambers. The motions were arbitrary chosen by the operator to provide an emission of electrons almost homogeneous in the 400×400 mm^2 range. The first cycle, performed with a source alone, was followed by three cycles with respectively 1, 2 and 3 layers of 100 μm Aluminum placed at both sides of the source. These "degraders" provided additional energy lines and thus improve the scintillators calibration.

7.3.3.2 Foils position

The events of interest are scattered by the Pb-foil. Unfortunately, additional events scattered by the surroundings are also recorded. The evaluation of this "background" is performed with measurements where the Pb-Foils are not in the trajectory of the electrons (Foils "OUT"). Since the data are gathered into files whose length is more or less related to the number of neutrons decaying in the HeBox, it was decided to use this length as a unit defining the cycle Pb-Foil IN/ Pb-foil OUT:

[5]These definitions of ST and VT are peculiar to the trigger and will be used only by the scalers.
[6]Multi-Branch System, GSI

- 15 files with both foils IN
- 5 files with only one foil OUT
- 1 file with both foils OUT
- 5 files with only the second foil OUT

The cycle was defined to minimize the Pb-foils motions.

7.3.4 Remarks on the run made in 2004

Several problems appeared during the run 2004 and others were discovered later during the analysis.

7.3.4.1 Instability of the MWPC gas mixture

The gas mixture used in the MWPC was set by several commercial flow meters (tapered glass tube with a float). It was soon obvious that these devices were unstable and needed frequent adjustments. Since the chambers are very sensitive to the mixture, their efficiency was unstable during the measurements. A use of flow controllers was proposed and should be implemented before the next measurement.

7.3.4.2 Calibration source lost

At the end of the calibration run performed on the 6/10, the Bi source was found missing. When the device was going back to the parking position, the spring used to keep straight the arm holding the source did not go into the slit at the bottom of the HeBox. It jumped out of its place and stayed in the HeBox. The upper part of the arm then folded back without control and the source fell to the bottom of the DMCS box.

Since several calibration runs were still to be performed and it wasn't sure that the windows of the MWPCs were not damaged, the HeBox was opened. The spring was exchanged and the calibration source recovered. Two days were necessary to do this and come back to normal acquisition.

The problem was caused by the change of shape of the springs due to mechanical constraints. So far, no solution has been found to prevent such deformation.

7.3.4.3 Low polarization of the neutrons

During the early stage of the data analysis, it soon became obvious that the neutron polarization was not as high as expected but around 40% [42].

The vertical magnetic field around the detector bends the electron trajectories on the projection (X,Z). The radius is about 2 m and is therefore not visible in one chamber only[7]. Nevertheless, it is possible for V-Tracks to compare the trajectories reconstructed by both chambers (Fig.7.24). The magnetic field in the beam line is going downward. Thus the field around the Mott polarimeter should go in the same direction and the shifting angle α should be positive.

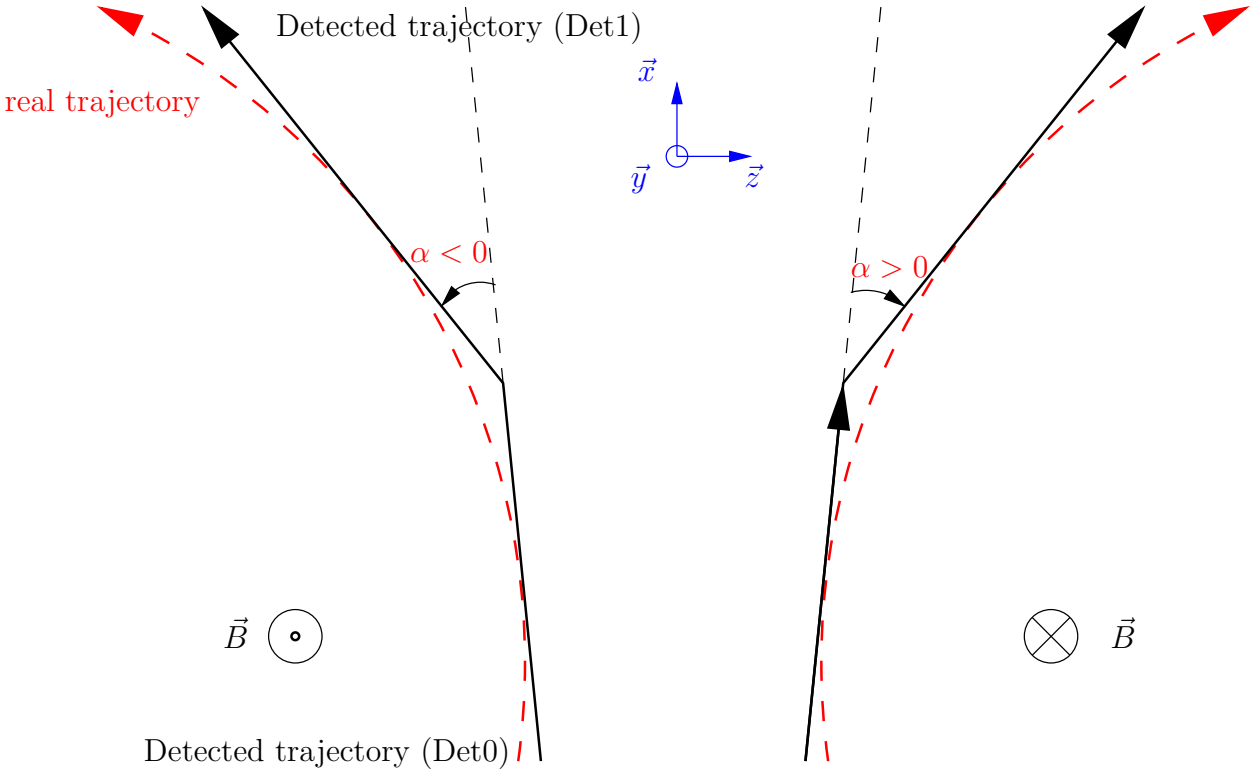

Figure 7.24: Influence of the magnetic field on the electron trajectory (both field direction).

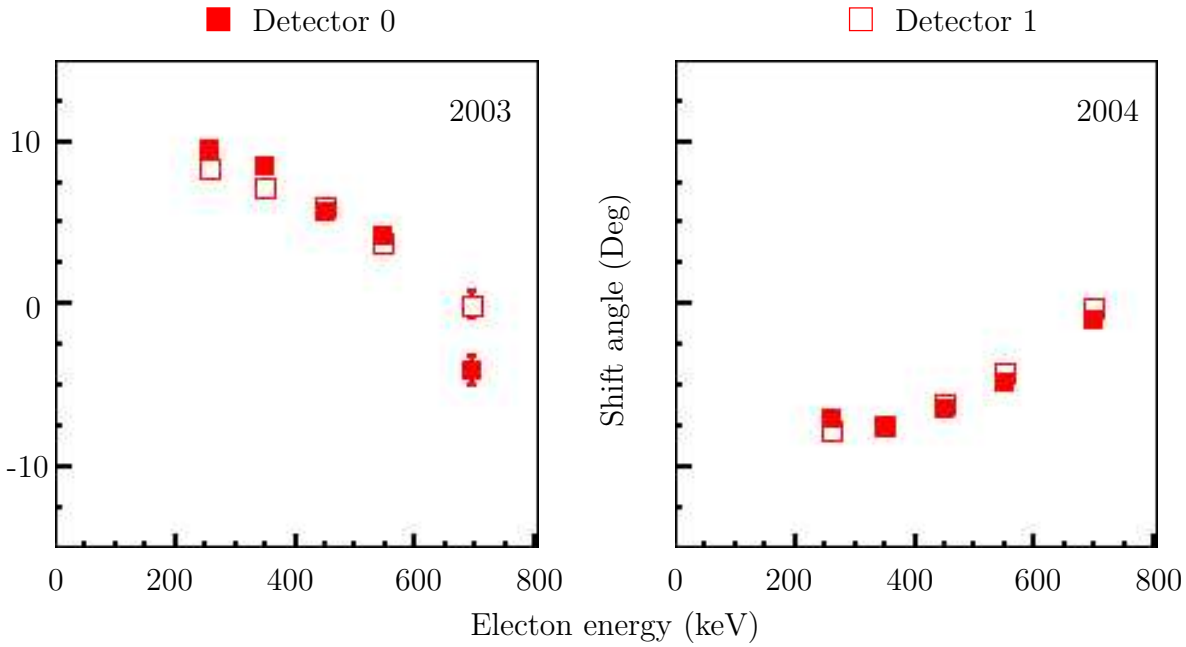

Figure 7.25: Average shift angle as a function of electron energy (2003 & 2004).

Figure 7.25 shows the centroids of the α distribution for 2003 and 2004 as a function

of energy. In 2003, the shifting angle is positive which means the magnetic field is going downward, whereas in 2004, it is going upward. Thus in 2004, the magnetic field around the detector was inverted compared to the rest of the line. This can explain the neutron polarization losses.

[7]The trajectories detected by the chambers are considered as linear

Chapter 8

Analysis

The methods used to analyzed the data are described in this chapter. At the beginning of the chapter are introduced the framework and the conventions employed later. Then the different ways to extract the parameters R and N are examined, followed by an overview of the reconstruction algorithm. The last part of the chapter presents a tomography-like method to localize the background sources.

8.1 Definitions and assumptions

8.1.1 Vectors and Angles

To describe the analysis procedure, it is necessary to introduce several definitions concerning the reference frames, the vectors and the others variables used further in the analysis. For the sake of simplicity, the emission and the scattering processed are described separately (Fig. 8.1).

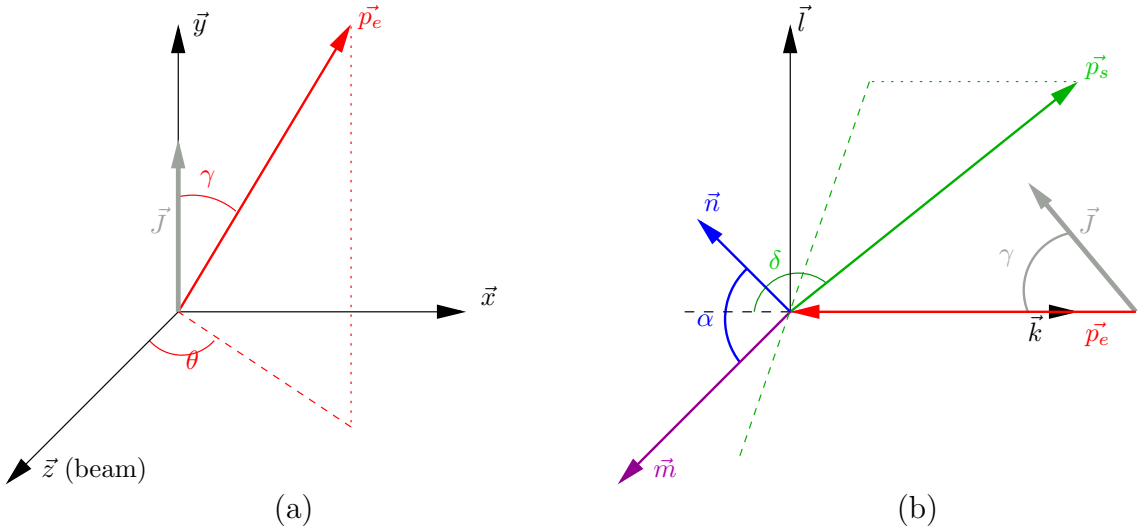

Figure 8.1: Reference frame for the analysis of the events acquired in the neutron decay experiment. The emission is described in (a) and the scattering in (b)

The reference frame is the the LAB-frame $(\vec{x}, \vec{y}, \vec{z})$ (Fig. 8.1(a)), identical to the neu-

tron rest frame (the velocity of the cold neutron is neglected); $\vec{z}$ is chosen along the neutron beam and directed downstream; $\vec{y}$ points vertically upwards and $\vec{x}$ is chosen in order to keep the frame orthogonal and right-handed. One has to notice that the neutron polarization $\vec{J}$ is collinear to $\vec{y}$. In this frame, the electron is emitted with a momentum $\vec{p}_e$ characterized by the angles (θ, γ).

It is easier to describe the scattering in a new frame, related to the emission momentum $\vec{p}_e$. The reference frame $(\vec{k}, \vec{l}, \vec{m})$ can be built as shown on Fig. 8.1(b) with the following definitions:

$$\begin{aligned} \vec{k} &= -\frac{\vec{p}_e}{|\vec{p}_e|} \\ \vec{m} &= \frac{\vec{J} \times \vec{p}_e}{|\vec{J} \times \vec{p}_e|} \\ \vec{l} &= \vec{m} \times \vec{k} \end{aligned}$$

In this frame, the unit vector $\hat{n}$ can be defined by:

$$\begin{aligned} \hat{n} &= \frac{(\vec{p}_e \times \vec{p}_s)}{|\vec{p}_e \times \vec{p}_s|} \\ &= \begin{pmatrix} 0 \\ \sin\alpha \\ \cos\alpha \end{pmatrix}_{(\vec{k},\vec{l},\vec{m})} \end{aligned} \tag{8.1}$$

and the definition of the unit vector $\hat{J}$ is

$$\hat{J} = \begin{pmatrix} \cos\gamma \\ \sin\gamma \\ 0 \end{pmatrix}_{(\vec{k},\vec{l},\vec{m})} \tag{8.2}$$

The scattering is then completely characterized by the angles δ and α.

8.1.2 Implementation in the decay rates equation

The symbols used in the following are defined as follows:

E – total electron energy at neutron decay.
E_e – kinetic electron energy at neutron decay.
E'_e – kinetic electron energy at scattering.
$\hat{p}_e$ – $\hat{p}_e = \vec{p}_e/|\vec{p}_e| = \begin{pmatrix} \sin\gamma\sin\theta \\ \cos\gamma \\ \sin\gamma\cos\theta \end{pmatrix}_{(\vec{x},\vec{y},\vec{z})} = \begin{pmatrix} -1 \\ 0 \\ 0 \end{pmatrix}_{(\vec{k},\vec{l},\vec{m})}$.
p_e – $p_e = |\vec{p}_e|$.
Ω_e – solid angle of the emitted electron in the LAB frame, defined by (θ, γ)
$\hat{p}_s$ – $\hat{p}_s = \vec{p}_s/|\vec{p}_s| = \begin{pmatrix} -\cos\delta \\ \sin\delta\cos\alpha \\ \sin\delta\sin\alpha \end{pmatrix}_{(\vec{k},\vec{l},\vec{m})}$.
p_s – $p_s = |\vec{p}_s|$.

Ω_s – solid angle of the scattered electron in the LAB frame, defined by (α, δ)
P – polarization value of the decaying neutron: $P = |\vec{J}|$.
'1' – neutron spin state: flipper #1 - off and flipper #2 - off.
'2' – neutron spin state: flipper #1 - on and flipper #2 - off.
'3' – neutron spin state: flipper #1 - off and flipper #2 - on.
'4' – neutron spin state: flipper #1 - on and flipper #2 - on.
η_1 – efficiency of flipper #1.
η_2 – efficiency of flipper #2.
d_M – nominal thickness of the Mott scattering target.
d'_M – effective thickness of the Mott scattering target.
β – velocity factor: $\beta = p_e c/E_e = v_e/c$.
m – electron rest mass.
ζ – electron mass-to-energy ratio: $\zeta = mc^2/E$.
ϵ – any implicit variable of the efficiency function to be integrated over (like decay origin, scattering point, etc.).

Equation (5.2) gives the probability of emission of electrons whose spins are in the direction $\vec{\sigma} = \hat{n}$ and Eq.(6.12) introduces the influence of the Mott scattering on these electrons. To take this effect into account and write the probability of scattering in the direction (α, δ) for electrons emitted in the direction (θ, γ), the following substitutions have to be performed in Eq.(5.2):

$$\vec{\sigma} \rightarrow S(E'_e, \delta)\hat{n} \tag{8.3}$$

$$\omega_0(E_e) = \frac{F(\pm Z, E_e)}{(2\pi)^4} p_e E_e (E^0 - E_e)^2 \rightarrow \omega_0(E_e)\sigma_M(E'_e, \delta) \tag{8.4}$$

where S and σ_M are the analyzing power and the scattering cross section. The Mott polarimeter gives access to $\hat{n}$ perpendicular to $\vec{p}_e$, so the terms containing G and Q disappear. In addition, neglecting the Fiertz interaction reduces the equation to:

$$\begin{aligned} \omega(P, \hat{n}|E, \Omega_e\Omega_s) dE d\Omega_e d\Omega_s &\propto 1 + AP\beta\, \hat{J}\cdot\hat{p}_e \\ &+ PS(E'_e, \delta)\left[N\,\hat{n}\cdot\hat{J} + R\beta\,\hat{n}\cdot(\hat{J}\times\hat{p}_e)\right] \end{aligned} \tag{8.5}$$

With $N' = N/\beta$, this equation becomes:

$$\begin{aligned} \omega(P, \hat{n}|E, \Omega_e\Omega_s) dE d\Omega_e d\Omega_s &\propto 1 + P\beta\left\{A\,\hat{J}\cdot\hat{p}_e + S(E'_e, \delta)\left[N'\,\hat{n}\cdot\hat{J} + R\,\hat{n}\cdot(\hat{J}\times\hat{p}_e)\right]\right\} \\ &= 1 + P\beta\{A\,\mathcal{F}(\gamma) + S(E'_e, \delta)\,[N'\,\mathcal{G}(\gamma, \alpha) + R\,\mathcal{H}(\gamma, \alpha)]\} \end{aligned} \tag{8.6}$$

The geometrical factors $\mathcal{F}$, $\mathcal{G}$ and $\mathcal{H}$ are defined by:

$$\begin{aligned} \mathcal{F}(\gamma) &= \hat{J}\cdot\hat{p}_e \\ &= \cos\gamma \end{aligned} \tag{8.7}$$

$$\begin{aligned} \mathcal{G}(\gamma, \alpha) &= \hat{n}\cdot\hat{J} \\ &= (\sin\alpha\,\vec{l} + \cos\alpha\,\vec{m})\cdot\hat{J} \\ &= \sin\alpha\sin\gamma \end{aligned} \tag{8.8}$$

$$\begin{aligned} \mathcal{H}(\gamma, \alpha) &= \hat{n}\cdot(\hat{J}\times\hat{p}_e) \\ &= \cos\alpha\sin\gamma \end{aligned} \tag{8.9}$$

with the conventions previously defined.

The neutron decay is measured for four neutron spin states with neutron polarizations chosen as:

$$P_1 = +P, \;\; P_2 = -\eta_1 P, \;\; P_3 = -\eta_2 P, \;\; P_4 = +\eta_1\eta_2 P, \tag{8.10}$$

The rates of electrons scattered in the Mott process become:

$$\begin{aligned}
\omega_1(E_e,\gamma;E'_e,\delta;\alpha) &= \omega_0(E_e)\,\sigma_M(E'_e,\delta,d'_M)\,\{1 + \\
&+ P\beta(E_e)\,\{A\,\mathcal{F}(\gamma) + S(E'_e,\delta,d'_M)\,[N'\,\mathcal{G}(\gamma,\alpha) + R\,\mathcal{H}(\gamma,\alpha)]\}\} \\
\omega_2(E_e,\gamma;E'_e,\delta;\alpha) &= \omega_0(E_e)\,\sigma_M(E'_e,\delta,d'_M)\,\{1 + \\
&- \eta_1 P\beta(E_e)\,\{A\,\mathcal{F}(\gamma) + S(E'_e,\delta,d'_M)\,[N'\,\mathcal{G}(\gamma,\alpha) + R\,\mathcal{H}(\gamma,\alpha)]\}\} \\
\omega_3(E_e,\gamma;E'_e,\delta;\alpha) &= \omega_0(E_e)\,\sigma_M(E'_e,\delta,d'_M)\,\{1 + \\
&- \eta_2 P\beta(E_e)\,\{A\,\mathcal{F}(\gamma) + S(E'_e,\delta,d'_M)\,[N'\,\mathcal{G}(\gamma,\alpha) + R\,\mathcal{H}(\gamma,\alpha)]\}\} \\
\omega_4(E_e,\gamma;E'_e,\delta;\alpha) &= \omega_0(E_e)\,\sigma_M(E'_e,\delta,d'_M)\,\{1 + \\
&+ \eta_1\eta_2 P\beta(E_e)\,\{A\,\mathcal{F}(\gamma) + S(E'_e,\delta,d'_M)\,[N'\,\mathcal{G}(\gamma,\alpha) + R\,\mathcal{H}(\gamma,\alpha)]\}\},
\end{aligned} \tag{8.11}$$

where σ_M is the the Mott scattering probability for unpolarized electrons with the kinetic energy E'_e in the target of density ρ_M and thickness d_M:

$$\sigma_M(E'_e,\delta,d'_M) = \frac{d\sigma_M}{d\Omega_s}(E'_e,\delta)\,\rho_M\,d_M \tag{8.12}$$

d_M is the real thickness of the target, which is different from the apparent thickness d'_M seen by the electron. The scatterer is set perpendicularly to x-axis. Therefore the apparent thickness is:

$$d'_M = \frac{d_M}{|\sin\theta_e\cos\phi_e|} \tag{8.13}$$

One must notice that the Mott differential cross section $d\sigma_M/d\Omega_s$ and the analyzing power S are functions of the electron energy E' before the scattering process. The energy losses between the emission and the scattering must be taken into account.

8.2 Asymmetry

As already mentioned in Sec. 6.2.3, there are three ways to write an asymmetry in order to calculate R:

- The "left-right" asymmetry in the Mott scattering.
- The asymmetry between electrons scattered on the same side for neutron spin UP and DOWN.
- Both asymmetries at the same time, to form a super-ratio.

Equation (8.11) shows the rate of electrons *emitted* with the characteristics $(E_e, \gamma; E'_e, \delta; \alpha)$ which has to be corrected with the efficiency and the acceptance of the detector. In the following, the geometrical acceptance of the detector will be included in the efficiency, and a more general convention will be used for ω: ω_i will be either ω_1 or ω_4 (neutron spin UP) and ω_j correspond to ω_2 or ω_3 (neutron spin DOWN). Additionally when "left" and "right" scattering are separated, the range of α will be limited to $[0, \pi[$ and $\omega'(\alpha) = \omega(\alpha + \pi)$. Then

$$\begin{aligned} x(E_e, \gamma; E'_e, \delta; \alpha) &= A\,\mathcal{F}(\gamma) + S(E'_e, \delta, d'_M)\,[N'\,\mathcal{G}(\gamma, \alpha) + R\,\mathcal{H}(\gamma, \alpha)] \\ x'(E_e, \gamma; E'_e, \delta; \alpha) &= x'(E_e, \gamma; E'_e, \delta; \alpha + \pi) \\ &= A\,\mathcal{F}(\gamma) - S(E'_e, \delta, d'_M)\,[N'\,\mathcal{G}(\gamma, \alpha) + R\,\mathcal{H}(\gamma, \alpha)] \end{aligned} \tag{8.14}$$

it is then obvious that:

$$\begin{aligned} x(E_e, \gamma; E'_e, \delta; \alpha) - x'(E_e, \gamma; E'_e, \delta; \alpha) &= 2S(E'_e, \delta, d'_M)\,[N'\,\mathcal{G}(\gamma, \alpha) + R\,\mathcal{H}(\gamma, \alpha)] \\ x(E_e, \gamma; E'_e, \delta; \alpha) + x'(E_e, \gamma; E'_e, \delta; \alpha) &= 2A\,\mathcal{F}(\gamma) \end{aligned} \tag{8.15}$$

The rates of detection become:

$$\begin{aligned} \omega_i(E_e, \gamma; E'_e, \delta; \alpha) &= \omega_0\,W_0\;\epsilon(E_e, \gamma; E'_e, \delta; \alpha)[1 + \eta_i P\beta\,x(E_e, \gamma; E'_e, \delta; \alpha)] \\ \omega'_i(E_e, \gamma; E'_e, \delta; \alpha) &= \omega_0\,W_0\;\epsilon'(E_e, \gamma; E'_e, \delta; \alpha)[1 + \eta_i P\beta\,x'(E_e, \gamma; E'_e, \delta; \alpha)] \\ \omega_j(E_e, \gamma; E'_e, \delta; \alpha) &= \omega_0\,W_0\;\epsilon(E_e, \gamma; E'_e, \delta; \alpha)[1 - \eta_j P\beta\,x(E_e, \gamma; E'_e, \delta; \alpha)] \\ \omega'_j(E_e, \gamma; E'_e, \delta; \alpha) &= \omega_0\,W_0\;\epsilon'(E_e, \gamma; E'_e, \delta; \alpha)[1 - \eta_j P\beta\,x'(E_e, \gamma; E'_e, \delta; \alpha)] \end{aligned} \tag{8.16}$$

8.2.1 "Left-right" asymmetry

This is a straightforward application of the setup described in section 6.2.3. This method is very simple to use in a symmetric setup with respect to the beam. In this case, the asymmetry is written for one spin state $\Psi \in \{1, 2, 3, 4\}$:

$$Asym_\Psi(E_e, \gamma; E'_e, \delta; \alpha) = \frac{\omega_\Psi(E_e, \gamma; E'_e, \delta; \alpha) - \omega'_\Psi(E_e, \gamma; E'_e, \delta; \alpha)}{\omega_\Psi(E_e, \gamma; E'_e, \delta; \alpha) + \omega'_\Psi(E_e, \gamma; E'_e, \delta; \alpha)} \tag{8.17}$$

and the substitution of Eq.(8.16) in the previous equation leads to:

$$Asym_\Psi(E_e, \gamma; E'_e, \delta; \alpha) = \frac{\epsilon(1 + \eta_\Psi P\beta x) - \epsilon'(1 + \eta_\Psi P\beta x')}{\epsilon(1 + \eta_\Psi P\beta x) + \epsilon'(1 + \eta_\Psi P\beta x')} \tag{8.18}$$

$$\tag{8.19}$$

The efficiencies can be written as $\epsilon' = \epsilon - \Delta\epsilon$ then:

$$Asym_\Psi(E_e, \gamma; E'_e, \delta; \alpha) = \frac{\epsilon\eta_\Psi P\beta(x - x') + \Delta\epsilon(1 + \eta_\Psi P\beta x)}{\epsilon\eta_\Psi P\beta(x + x') + \Delta\epsilon(1 + \eta_\Psi P\beta x)} \tag{8.20}$$

$$= \frac{\eta_\Psi P\beta(x - x') + \frac{\Delta\epsilon}{\epsilon}(1 + \eta_\Psi P\beta x)}{\eta_\Psi P\beta(x + x') + \frac{\Delta\epsilon}{\epsilon}(1 + \eta_\Psi P\beta x)} \tag{8.21}$$

$$Asym_\Psi(E_e, \gamma; E'_e, \delta; \alpha) = \frac{\eta_\Psi P\beta S[N'\,\mathcal{G} + R\,\mathcal{H}] + \frac{\Delta\epsilon}{2\epsilon}(1 + \eta_\Psi P\beta x)}{1 + \eta_\Psi P\beta 2A\,\mathcal{F} + \frac{\Delta\epsilon}{2\epsilon}(1 + \eta_\Psi P\beta x)} \tag{8.22}$$

If $\Delta\epsilon/\epsilon \ll 1$, the asymmetry can be simplified to:

$$Asym_{\Psi}(E_e,\gamma;E'_e,\delta;\alpha) = \frac{\eta P\beta S(E'_e,\delta,d'_M)\,[N'\,\mathcal{G}(\gamma,\alpha) + R\,\mathcal{H}(\gamma,\alpha)]}{1+\eta P\beta A\mathcal{F}(\gamma)} \tag{8.23}$$

It is obvious that this method requires a symmetric setup having especially $\epsilon = \epsilon'$ or instead a good control over the efficiency. If this condition is fullfiled the asymmetry will depend only on geometrical factors introduced by $\mathcal{F}$, $\mathcal{G}$ and $\mathcal{H}$. For a given angle γ and energy, the asymmetry as a function of α will be the sum of a cosine and a sinus with the respective weights given to N and R.

8.2.2 Asymmetry under neutron spin inversion

The asymmetry for a fixed angle α obtained by inverting the neutron spin is:

$$Asym_{ij}(E_e,\gamma;E'_e,\delta;\alpha) = \frac{\omega_i(\alpha)-\omega_j(\alpha)}{\omega_i(\alpha)+\omega_j(\alpha)} \tag{8.24}$$

with the substitution given by Eq.(8.16), the previous equation becomes

$$\begin{aligned} Asym_{ij}(E_e,\gamma;E'_e,\delta;\alpha) &= \frac{\epsilon(1+\eta_i P\beta x)-\epsilon(1-\eta_j P\beta x)}{\epsilon(1+\eta_i P\beta x)+\epsilon(1-\eta_j P\beta x)} \\ &= \frac{(\eta_i+\eta_j)P\beta x}{2+(\eta_i-\eta_j)P\beta x} \end{aligned} \tag{8.25}$$

Assuming that the spin flipper efficiencies are very similar, one can write $\eta = \eta_j = \eta_i + \Delta\eta$, then

$$Asym_{ij}(E_e,\gamma;E'_e,\delta;\alpha) = \frac{P\beta x(\eta+\frac{\Delta\eta}{2})}{1-P\beta x\frac{\Delta\eta}{2}} \tag{8.26}$$

if $\Delta\eta/2 \ll 1$, then it is possible to simplify this expression to:

$$Asym_{ij}(E_e,\gamma;E'_e,\delta;\alpha) = \eta P\beta\{A\,\mathcal{F}(\gamma) + S(E'_e,\delta,d'_M)\,[N'\,\mathcal{G}(\gamma,\alpha) + R\,\mathcal{H}(\gamma,\alpha)]\} \tag{8.27}$$

The obvious advantage of this method is the cancellation of the efficiencies in the asymmetry. In the previous equation, the influence of the parameters A, N and R are of the same order. The A-correlation depends on $\cos(\gamma)$ only whereas the N- and R-correlations depend both on $\sin(\gamma)$ and on $\sin(\alpha)$ and $\cos(\alpha)$ respectively. The asymmetry sensitivity with respect to the N- and R-correlations is thus maximum from electrons emitted horizontally and the offset generated by the A-correlation is then equal to zero.

8.2.3 Super-ratio

The super-ratio r is defined by the expression:

$$r(\alpha) = \frac{\sqrt{\omega_i(\alpha)\omega'_j(\alpha)}}{\sqrt{\omega'_i(\alpha)\omega_j(\alpha)}} \tag{8.28}$$

and the asymmetry can then be written as

$$\begin{aligned} Asym_{ij}(\alpha) &= \frac{r(\alpha)-1}{r(\alpha)+1} && (8.29)\\ &= \frac{\omega_i(\alpha)\omega'_j(\alpha)-\omega'_i(\alpha)\omega_j(\alpha)}{\left[\sqrt{\omega_i(\alpha)\omega'_j(\alpha)}+\sqrt{\omega'_i(\alpha)\omega_j(\alpha)}\right]^2} \\ &= \frac{\omega_i(\alpha)\omega'_j(\alpha)-\omega'_i(\alpha)\omega_j(\alpha)}{\omega_i(\alpha)\omega'_j(\alpha)+\omega'_i(\alpha)\omega_j(\alpha)+2\sqrt{\omega_i(\alpha)\omega'_j(\alpha)\omega'_i(\alpha)\omega_j(\alpha)}} && (8.30)\end{aligned}$$

In order to simplify this equation, the numerator and the denominator are treated separately:

$$\begin{aligned} \omega_i(\alpha)\omega'_j(\alpha)-\omega'_i(\alpha)\omega_j(\alpha) &= \epsilon\epsilon' P\beta(\eta_i+\eta_j)(x-x') && (8.31)\\ \omega_i(\alpha)\omega'_j(\alpha)-\omega'_i(\alpha)\omega_j(\alpha) &= \epsilon\epsilon'\left[2+P\beta(\eta_i-\eta_j)(x+x')-2\eta_i\eta_j P^2\beta^2 xx'\right] && (8.32)\end{aligned}$$

$$\begin{aligned} \omega_i(\alpha)\omega'_j(\alpha)\omega'_i(\alpha)\omega_j(\alpha) = (\epsilon\epsilon')^2[& \quad 1 \\ & + \quad (\eta_i-\eta_j)P\beta(x+x') \\ & + \quad (\eta_i^2+\eta_j^2)P^2\beta^2 xx' + \eta_i\eta_j P^2\beta^2(x+x')^2 \\ & + \quad (\eta_i\eta_j^2-\eta_i^2\eta_j)P^3\beta^3(x+x')xx' \\ & + \quad \eta_i^2\eta_j^2 P^4\beta^4 x^2 x'^2 \quad] \end{aligned} \tag{8.33}$$

Where xx has the form:

$$\begin{aligned} xx' &= \{A\mathcal{F}+S[N'\mathcal{G}(\gamma,\alpha)+R\mathcal{H}(\gamma,\alpha)]\}\{A\mathcal{F}-S[N'\mathcal{G}(\gamma,\alpha)+R\mathcal{H}(\gamma,\alpha)]\} \\ &= (A\mathcal{F})^2-(S[N'\mathcal{G}(\gamma,\alpha)+R\mathcal{H}(\gamma,\alpha)])^2 && (8.34)\end{aligned}$$

The present knowledge about S, N and R allows the approximation

$$(S[N'\mathcal{G}(\gamma,\alpha)+R\mathcal{H}(\gamma,\alpha)])^2 \ll 1 \tag{8.35}$$

In addition, assuming that $\eta=\eta_i\simeq\eta_j$, the asymmetry simplifies to:

$$Asym_{ij} \simeq \frac{\eta P\beta\eta(x-x')}{2-2\eta^2P^2\beta^2(x+x')(A\mathcal{F})^2+2\sqrt{1-2\eta^2(A\mathcal{F})^2+\eta^4(A\mathcal{F})^4}} \tag{8.36}$$

or explicitly

$$Asym_{ij}(E_e,\gamma;E'_e,\delta;\alpha) = \frac{\eta P\beta S(E'_e,\delta,d'_M)\left[N'\,\mathcal{G}(\gamma,\alpha)+R\,\mathcal{H}(\gamma,\alpha)\right]}{1-[\eta P\beta A\,\mathcal{F}(\gamma)]^2} \tag{8.37}$$

The advantages of this method, compared to the "left-right" asymmetry is twofold: i) no assumption on the efficiencies is needed and ii) the systematic effect due to A is smaller: PA is of the order of magnitude of 0.1 so $(PA)^2$ is in the order of magnitude of 0.01, which becomes negligible with respect to 1.

8.3 Integration

To summarize, the three asymmetries calculated above are

- "left-right" (for $\epsilon \simeq \epsilon'$)

$$Asym(E_e, \gamma; E'_e, \delta; \alpha) = \frac{\eta P \beta S(E'_e, \delta, d'_M) \left[N' \, \mathcal{G}(\gamma, \alpha) + R \, \mathcal{H}(\gamma, \alpha)\right]}{1 + \eta P \beta A \, \mathcal{F}(\gamma)}$$

- "Up-Down" (with $\eta = \eta_i \simeq \eta_j$)

$$Asym_{ij}(E_e, \gamma; E'_e, \delta; \alpha) = \eta P \beta \{A \, \mathcal{F}(\gamma) + S(E'_e, \delta, d'_M) \left[N' \, \mathcal{G}(\gamma, \alpha) + R \, \mathcal{H}(\gamma, \alpha)\right]\}$$

- Super-ratio (with $\eta = \eta_i \simeq \eta_j$)

$$Asym_{ij}(E_e, \gamma; E'_e, \delta; \alpha) = \frac{\eta P \beta S(E'_e, \delta, d'_M) \left[N' \, \mathcal{G}(\gamma, \alpha) + R \, \mathcal{H}(\gamma, \alpha)\right]}{1 - [\eta P \beta A \, \mathcal{F}(\gamma)]^2}$$

These three asymmetries are calculated for point-like sources, target and detectors and our experimental setup does not correspond to these conditions. Therefore, the rates must be integrated before the calculation of the asymmetries. Two methods of integration are studied, called "the micro-integration" and the "macro-integration".

8.3.1 Micro-integration

The main issue of the integration is the *unknown* efficiency of the detectors, in particular the MWPC. The efficiency of each measurement plane is convoluted with the efficiencies of the other planes. But the whole setup can be seen as a set of small Mott polarimeters. The integration range is defined by:

- The neutrons decay in the volume $V(x_0, y_0, z_0)$ defined by:
  - $x \in [x_0; x_0 + \Delta x]$
  - $y \in [y_0; y_0 + \Delta y]$
  - $z \in [y_0; z_0 + \Delta z]$
- The electrons are emitted in the solid angle Ω_e defined by:
  - $\theta \in [\theta_0; \theta_0 + \Delta\theta]$
  - $\gamma \in [\gamma_0; \gamma_0 + \Delta\gamma]$
- The electrons called "right" are scattered in the solid angle Ω_s defined by:
  - $\alpha \in [\alpha_0; \alpha_0 + \Delta\alpha]$
  - $\delta \in [\delta_0; \delta_0 + \Delta\delta]$
- The electrons called "left" are scattered in the solid angle Ω'_s defined by:
  - $\alpha \in [\alpha_0 + \pi; \alpha_0 + \pi + \Delta\alpha]$

– $\delta \in [\delta_0; \delta_0 + \Delta\delta]$

- The electrons are emitted with an energy:

– $E_e \in [E_{e0}; E_{e0} + \Delta E_e]$

Over the energy interval, the electron velocity β can be considered as constant. Four rates are detected, one for each possible couple "neutron polarization state/electron scattering side".

$$\begin{aligned}
N_i(x_0, y_0, z_0, \gamma_0, \theta_0, \alpha_0, \delta_0) &= \int_V \int_{\Omega_e} \int_{\Omega_s} \int_{E_e} \epsilon(V, \Omega_e, \Omega_s, E_e)\omega_i(V, \Omega_e, \Omega_s, E_e) dv d\Omega_e d\Omega_s dE_e \\
N'_i(x_0, y_0, z_0, \gamma_0, \theta_0, \alpha_0, \delta_0) &= \int_V \int_{\Omega_e} \int_{\Omega_s} \int_{E_e} \epsilon'(V, \Omega_e, \Omega_s, E_e)\omega'_i(V, \Omega_e, \Omega_s, E_e) dv d\Omega_e d\Omega_s dE_e \\
N_j(x_0, y_0, z_0, \gamma_0, \theta_0, \alpha_0, \delta_0) &= \int_V \int_{\Omega_e} \int_{\Omega_s} \int_{E_e} \epsilon(V, \Omega_e, \Omega_s, E_e)\omega_j(V, \Omega_e, \Omega_s, E_e) dv d\Omega_e d\Omega_s dE_e \\
N'_j(x_0, y_0, z_0, \gamma_0, \theta_0, \alpha_0, \delta_0) &= \int_V \int_{\Omega_e} \int_{\Omega_s} \int_{E_e} \epsilon'(V, \Omega_e, \Omega_s, E_e)\omega'_j(V, \Omega_e, \Omega_s, E_e) dv d\Omega_e d\Omega_s dE_e
\end{aligned} \tag{8.38}$$

with $\epsilon'(V, \Omega_e, \Omega_s, E_e) = \epsilon(V, \Omega_e, \Omega'_s, E_e)$ If the integration range is small enough so that ϵ and ϵ' can be considered as constant, the efficiencies can be extracted from the integrals. Then ω can be substituted by Eq.(8.11) and five integrals can be defined:

$$N_0 = \int_V \int_{\Omega_e} \int_{\Omega_s} \int_{E_e} w_0(E_e) W_0(\Omega_e, E_e) \tag{8.39}$$

$$\langle A \rangle = [N_0]^{-1} \int_V \int_{\Omega_e} \int_{\Omega_s} \int_{E_e} w_0(E_e) W_0(\Omega_e, E_e) \mathcal{F}(\gamma) \tag{8.40}$$

$$\langle S \rangle = [N_0]^{-1} \int_V \int_{\Omega_e} \int_{\Omega_s} \int_{E_e} w_0(E_e) W_0(\Omega_e, E_e) S(\delta, E'_e) \tag{8.41}$$

$$\langle R \rangle = [N_0 \langle S \rangle]^{-1} \int_V \int_{\Omega_e} \int_{\Omega_s} \int_{E_e} w_0(E_e) W_0(\Omega_e, E_e) S(\delta, E'_e) \mathcal{G}(\gamma, \alpha) \tag{8.42}$$

$$\langle N \rangle = [N_0 \langle S \rangle]^{-1} \int_V \int_{\Omega_e} \int_{\Omega_s} \int_{E_e} w_0(E_e) W_0(\Omega_e, E_e) S(\delta, E'_e) \mathcal{H}(\gamma, \alpha) \tag{8.43}$$

With these notations, the rates can be written as:

$$N_i = \epsilon N_0 \{1 + \eta_i P \beta [A\langle A \rangle + \langle S \rangle (N\langle N \rangle + R\langle R \rangle)]\} \tag{8.44}$$

$$N'_i = \epsilon' N_0 \{1 + \eta_i P \beta [A\langle A \rangle - \langle S \rangle (N\langle N \rangle + R\langle R \rangle)]\} \tag{8.45}$$

$$N_j = \epsilon N_0 \{1 - \eta_j P \beta [A\langle A \rangle + \langle S \rangle (N\langle N \rangle + R\langle R \rangle)]\} \tag{8.46}$$

$$N'_j = \epsilon' N_0 \{1 - \eta_j P \beta [A\langle A \rangle - \langle S \rangle (N\langle N \rangle + R\langle R \rangle)]\} \tag{8.47}$$

Because of the similarity with Eq.(8.11), it is straightforward to write the "UP/DOWN" asymmetry and the super-ratio for these integration, for $\eta = \eta_i \simeq \eta_j$

- For the "Up-Down" asymmetry

$$Asym_{ij}(x_0, y_0, z_0, \gamma_0, \theta_0, \alpha_0, \delta_0, E_{e0}) = \eta P \beta [A\langle A \rangle + \langle S \rangle (N\langle N \rangle + R\langle R \rangle)]$$

- For the super-ratio

$$Asym_{ij}(x_0, y_0, z_0, \gamma_0, \theta_0, \alpha_0, \delta_0, E_{e0}) = \frac{\eta P \beta \langle S \rangle (N \langle N \rangle + R \langle R \rangle)}{1 - [\eta P \beta A \langle A \rangle]^2}$$

It is useless to write the "left-right" asymmetry since ϵ and ϵ' are unknown and *a fortiori* not equal.

This way of building the asymmetry seems to be rather easy to use. Since the efficiencies of the detector do not appear in the calculation, it is possible to simulate events in order to find the value of the integrals. A large number of asymmetries will be obtained (depending on the binning on the variables) and can be considered as the result of several independent experiments.

However, two problems arise. The first one is technical and related to the method of construction of the integrals. One must remember that the ranges of integration are chosen in order to assume the efficiencies to be constant. This requirement imposes the sorting of the data over a large number of variables (Position of emission, direction of emission, direction of scattering and energy). If an very optimistic situation is considered, for instance 10^6 events sorted in the following binning:

- $Y_{emission} \in [-500; 500] \longrightarrow 10$ bins
- $Z_{emission} \in [-100; 100] \longrightarrow 2$ bins
- $\gamma \in [-60; 60] \longrightarrow 4$ bins
- $\theta \in [-60; 60] \longrightarrow 4$ bins
- $\alpha \in [0; 360] \longrightarrow 8$ bins
- $\delta \in [60; 180] \longrightarrow 3$ bins

$\Rightarrow 10 * 2 * 4 * 4 * 8 * 3 = 7680$ bins so in average each bin will receive 130 events.

The second problem concerns the super-ratio and comes from an implicit condition: it is possible to build the super-ratio (Eq.(8.37)) *only* if the efficiencies ϵ and ϵ' are different from zero. The consequence is that for given values of γ, θ, α and δ, both "Left" *and* "Right" events have to be detectable. This is not so critical for the real efficiency which should never be zero, but it means that for a range of variables, the symmetric range with respect to the emission direction must be detectable, and therefore be within the acceptance of the detector. This condition reduces the usefull statistics by 3 orders of magnitude.

8.3.2 Macro-integration

The detector is now seen as a whole entity. The integration is performed on the whole detector for all variables, except three of them: γ, E_e and α which are integrated over "small" ranges in order to separate the contribution of N and R in the measured rates.

We have then:

$$N_i(k,l) = \int_{E_e(k)-\frac{\Delta E_e}{2}}^{E_e(k)+\frac{\Delta E_e}{2}} \int_{\alpha(m)-\frac{\Delta\alpha}{2}}^{\alpha(m)+\frac{\Delta\alpha}{2}} \int_{other\ \ variables} \epsilon\omega_i \tag{8.48}$$

$$N'_i(k,l) = \int_{E_e(k)-\frac{\Delta E_e}{2}}^{E_e(k)+\frac{\Delta E_e}{2}} \int_{\alpha(m)-\frac{\Delta\alpha}{2}}^{\alpha(m)+\frac{\Delta\alpha}{2}} \int_{other\ \ variables} \epsilon'\omega'_i \tag{8.49}$$

$$N_j(k,l) = \int_{E_e(k)-\frac{\Delta E_e}{2}}^{E_e(k)+\frac{\Delta E_e}{2}} \int_{\alpha(m)-\frac{\Delta\alpha}{2}}^{\alpha(m)+\frac{\Delta\alpha}{2}} \int_{other\ \ variables} \epsilon\omega_j \tag{8.50}$$

$$N'_j(k,l) = \int_{E_e(k)-\frac{\Delta E_e}{2}}^{E_e(k)+\frac{\Delta E_e}{2}} \int_{\alpha(m)-\frac{\Delta\alpha}{2}}^{\alpha(m)+\frac{\Delta\alpha}{2}} \int_{other\ \ variables} \epsilon'\omega'_j \tag{8.51}$$

The electron velocity can be considered as constant. Thus five integrals can built for a "left" scattering ($\beta = \beta(k)$):

$$\overline{N}_0(k,l) = \int \epsilon(\Omega_e,\Omega_s,E_e)w_0(E_e)W_0(\Omega_e,E_e) \tag{8.52}$$

$$\overline{\mathcal{F}}(k,l) = [N_0]^{-1}\int \epsilon(\Omega_e,\Omega_s,E_e)w_0(E_e)W_0(\Omega_e,E_e)\mathcal{F}(\gamma) \tag{8.53}$$

$$\overline{S}(k,l) = [N_0]^{-1}\int \epsilon(\Omega_e,\Omega_s,E_e)w_0(E_e)W_0(\Omega_e,E_e)S(\delta,E'_e) \tag{8.54}$$

$$\overline{\mathcal{G}}(k,l) = [N_0\overline{S}]^{-1}\int \epsilon(\Omega_e,\Omega_s,E_e)w_0(E_e)W_0(\Omega_e,E_e)S(\delta,E'_e)\mathcal{G}(\gamma,\alpha) \tag{8.55}$$

$$\overline{\mathcal{H}}(k,l) = [N_0\overline{S}]^{-1}\int \epsilon(\Omega_e,\Omega_s,E_e)w_0(E_e)W_0(\Omega_e,E_e)S(\delta,E'_e)\mathcal{H}(\gamma,\alpha) \tag{8.56}$$

For a "right" scattering, five additional integrals are defined:

$$\overline{N}'_0(k,l) = \int \epsilon'(\Omega_e,\Omega_s,E_e)w_0(E_e)W_0(\Omega_e,E_e) \tag{8.57}$$

$$\overline{\mathcal{F}}'(k,l) = [N_0]^{-1}\int \epsilon'(\Omega_e,\Omega_s,E_e)w_0(E_e)W_0(\Omega_e,E_e)\mathcal{F}(\gamma) \tag{8.58}$$

$$\overline{S}'(k,l) = [N_0]^{-1}\int \epsilon'(\Omega_e,\Omega_s,E_e)w_0(E_e)W_0(\Omega_e,E_e)S(\delta,E'_e) \tag{8.59}$$

$$\overline{\mathcal{G}}'(k,l) = [N_0\overline{S}]^{-1}\int \epsilon'(\Omega_e,\Omega_s,E_e)w_0(E_e)W_0(\Omega_e,E_e)S(\delta,E'_e)\mathcal{G}(\gamma,\alpha) \tag{8.60}$$

$$\overline{\mathcal{H}}'(k,l) = [N_0\overline{S}]^{-1}\int \epsilon'(\Omega_e,\Omega_s,E_e)w_0(E_e)W_0(\Omega_e,E_e)S(\delta,E'_e)\mathcal{H}(\gamma,\alpha) \tag{8.61}$$

so we can write the rates as:

$$N_i(k,l) = \overline{N}_0\{1+\eta_i P\beta(k)[A\overline{\mathcal{F}}+\overline{S}(N'\overline{\mathcal{G}}+R\overline{\mathcal{H}})]\} \tag{8.62}$$

$$N'_i(k,l) = \overline{N}'_0\{1+\eta_i P\beta(k)[A\overline{\mathcal{F}}'-\overline{S}'(N'\overline{\mathcal{G}}'+R\overline{\mathcal{H}}')]\} \tag{8.63}$$

$$N_j(k,l) = \overline{N}_0\{1-\eta_j P\beta(k)[A\overline{\mathcal{F}}+\overline{S}(N'\overline{\mathcal{G}}+R\overline{\mathcal{H}})]\} \tag{8.64}$$

$$N'_j(k,l) = \overline{N}'_0\{1-\eta_j P\beta(k)[A\overline{\mathcal{F}}'-\overline{S}'(N'\overline{\mathcal{G}}'+R\overline{\mathcal{H}}')]\} \tag{8.65}$$

The main difference between these equations and the similar ones in the previous section, Eqs.(8.44-8.47) is the presence of the efficiency inside the integrals. Then,

$$\begin{aligned} \overline{N_0} &\neq \overline{N_0}' \\ \overline{\mathcal{F}} &\neq \overline{\mathcal{F}}' \\ \overline{S} &\neq \overline{S}' \\ \overline{\mathcal{G}} &\neq \overline{\mathcal{G}}' \\ \overline{\mathcal{H}} &\neq \overline{\mathcal{H}}' \end{aligned} \tag{8.66}$$

The question now is how to evaluate $\overline{\mathcal{F}}$, $\overline{S}$, $\overline{\mathcal{G}}$ and $\overline{\mathcal{H}}$ (and their equivalents $\overline{\mathcal{F}}'$, $\overline{S}'$, $\overline{\mathcal{G}}'$, $\overline{\mathcal{H}}'$).

For an unpolarized beam, $P = 0$ so that the rate of detected events becomes:

$$N(k,l) = \overline{N_0}(k,l) = \int \epsilon(\Omega_e, \Omega_s, E_e) w_0(E_e) W_0(\Omega_e, E_e) \tag{8.67}$$

This unpolarized beam can be "artificially" created with a mixture of both neutron spin states:

$$\frac{1}{\eta_i} P_i + \frac{1}{\eta_j} P_j = 0 \tag{8.68}$$

with $P_i = \eta_i P$ and $P_j = -\eta_j P$. Therefore the rate of detected events induced by an unpolarized neutron beam is the weighted sum of Eq.(8.63) and Eq.(8.65).

$$N_0(k,l) = \frac{\eta_j N_i(k,l) + \eta_i N_j(k,l)}{\eta_j + \eta_i} \tag{8.69}$$

We can approximate the integral $N_0(k,l)$ with the rate of the reconstructed events having good characteristics over E_e, γ and α. We must notice that the higher the statistics, the better the approximation. We can now consider each microscopic part of the integral as sum of the reconstructed events with the requested characteristic. It is then easy to add a correction on the sum in order to build $\overline{\mathcal{F}}$, $\overline{S}$, $\overline{\mathcal{G}}$ and $\overline{\mathcal{H}}$:

$$\begin{aligned} \overline{\mathcal{F}}(k,l) &\simeq [N_0(k,l)(\eta_i + \eta_j)]^{-1} \\ &\times \left[\eta_j \sum_{n=1}^{N_i} \mathcal{F}(\gamma_n) + \eta_i \sum_{n=1}^{N_j} \mathcal{F}(\gamma_n) \right] \end{aligned} \tag{8.70}$$

$$\begin{aligned} \overline{S}(k,l) &\simeq [N_0(k,l)(\eta_i + \eta_j)]^{-1} \\ &\times \left[\eta_j \sum_{n=1}^{N_i} S(E_e^n, \Omega_e^n, \delta_n) + \eta_i \sum_{n=1}^{N_j} S(E_e^n, \Omega_e^n, \delta_n) \right] \end{aligned} \tag{8.71}$$

$$\begin{aligned} \overline{\mathcal{G}}(k,l) &\simeq [\overline{S}(k,l) N_0(k,l)(\eta_i + \eta_j)]^{-1} \\ &\times \left[\eta_j \sum_{n=1}^{N_i} S(E_e^n, \Omega_e^n, \delta_n) \mathcal{G}(\gamma_n, \alpha_n) + \eta_i \sum_{n=1}^{N_j} S(E_e^n, \Omega_e^n, \delta_n) \mathcal{G}(\gamma_n, \alpha_n) \right] \end{aligned} \tag{8.72}$$

$$\begin{aligned} \overline{\mathcal{H}}(k,l) &\simeq [\overline{S}(k,l) N_0(k,l)(\eta_i + \eta_j)]^{-1} \\ &\times \left[\eta_j \sum_{n=1}^{N_i} S(E_e^n, \Omega_e^n, \delta_n) \mathcal{H}(\gamma_n, \alpha_n) + \eta_i \sum_{n=1}^{N_j} S(E_e^n, \Omega_e^n, \delta_n) \mathcal{H}(\gamma_n, \alpha_n) \right] \end{aligned} \tag{8.73}$$

8.3.2.1 "Left/Right" asymmetry

This asymmetry for a spin state Ψ ($\Psi \in \{1,2,3,4\}$) can be built by analogy with Eq.(8.17):

$$Asym_{\Psi}(k,l) = \frac{N_{\Psi}(k,l) - N'_{\Psi}(k,l)}{N_{\Psi}(k,l) - N'_{\Psi}(k,l)} \tag{8.74}$$

with a substitution from Eq.(8.63) and Eq.(8.64), the asymmetry becomes:

$$Asym_{\Psi} = \frac{\overline{N}_0\{1+\eta_{\Psi}P\beta[A\overline{\mathcal{F}}+\overline{S}(N'\overline{\mathcal{G}}+R\overline{\mathcal{H}})]\} - \overline{N}'_0\{1+\eta_{\Psi}P\beta[A\overline{\mathcal{F}}'-\overline{S}'(N'\overline{\mathcal{G}}'+R\overline{\mathcal{H}}')]\}}{\overline{N}_0\{1+\eta_{\Psi}P\beta[A\overline{\mathcal{F}}+\overline{S}(N'\overline{\mathcal{G}}+R\overline{\mathcal{H}})]\} + \overline{N}'_0\{1+\eta_{\Psi}P\beta[A\overline{\mathcal{F}}'-\overline{S}'(N'\overline{\mathcal{G}}'+R\overline{\mathcal{H}}')]\}} \tag{8.75}$$

This formula can be established for each couple (k,l) but cannot be simplified in the general case because of different efficiencies. It is then possible to find numerically the value of the parameters R and N from Eq.(8.75).

8.3.2.2 "Up/Down" asymmetry

The efficiencies in the integrals are not critical here since the ranges of integration are the same for both neutron spin states and the efficiencies have no reason to depend on the neutron polarization. We can then find a result similar to Eq.(8.27)

$$Asym_{ij}(k,l) = \frac{(\eta_i+\eta_j)P\beta(k)\{A\,\overline{\mathcal{F}}+\overline{S}\,[N'(k)\,\overline{\mathcal{G}}+R\,\overline{\mathcal{H}}]\}}{2+(\eta_i-\eta_j)P\beta(k)\{A\,\overline{\mathcal{F}}+\overline{S}\,[N'(k)\,\overline{\mathcal{G}}+R\,\overline{\mathcal{H}}]\}} \tag{8.76}$$

then

$$P\beta(k)\{A\,\overline{\mathcal{F}}+\overline{S}\,[N'(k)\,\overline{\mathcal{G}}+R\,\overline{\mathcal{H}}]\} = \frac{N_i-N_j}{\eta_j N_i+\eta_i N_j} \tag{8.77}$$

8.3.2.3 Super-ratio

Because of the efficiencies, it is not possible to make the simplification in the super-ratio to get a result similar to Eq.(8.37). If we define:

$$\overline{X}(k,l) = A\,\overline{\mathcal{F}}(k,l)+\overline{S}(k,l)\,[N'(k)\,\overline{\mathcal{G}}(k,l)+R\,\overline{\mathcal{H}}(k,l)]\} \tag{8.78}$$

$$\overline{X}'(k,l) = A\,\overline{\mathcal{F}}'(k,l)-\overline{S}'(k,l)\,[N'(k)\,\overline{\mathcal{G}}'(k,l)+R\,\overline{\mathcal{H}}'(k,l)]\} \tag{8.79}$$

then

$$Asym_{ij}(k,l) = \frac{\sqrt{(1+\eta_i P\beta\overline{X})(1+\eta_j P\beta\overline{X}')}-\sqrt{(1+\eta_i P\beta\overline{X}')(1+\eta_j P\beta\overline{X})}}{\sqrt{(1+\eta_i P\beta\overline{X})(1+\eta_j P\beta\overline{X}')}+\sqrt{(1+\eta_i P\beta\overline{X}')(1+\eta_j P\beta\overline{X})}} \tag{8.80}$$

$$Asym_{ij}(k,l) = \frac{P\beta(k)(\eta_i+\eta_j)(\overline{X}-\overline{X}')}{2+P\beta(k)(\eta_i-\eta_j)(\overline{X}+\overline{X}')+2\eta_i\eta_j(P\beta(k))\overline{X}\overline{X}'+\sqrt{SQRT}} \tag{8.81}$$

with

$$SQRT = (1+\eta_i P\beta\overline{X})(1+\eta_j P\beta\overline{X}')(1+\eta_i P\beta\overline{X}')(1+\eta_j P\beta\overline{X}) \tag{8.82}$$

Again, the asymmetry cannot be simplified because of the different efficiencies and the determination of the parameters R and N must be done numerically.

8.3.2.4 Discussion over the Macro-integration

The advantage of this method of integration is the possibility to determine the parameters without knowing *a priori* the efficiency of the detector, since the geometrical factors $\overline{\mathcal{F}}$, $\overline{S}$, $\overline{\mathcal{G}}$ and $\overline{\mathcal{H}}$ are calculated using the experimental data. The difficulty related to that point is that different data must be used for their calculation than for the evaluation of the parameters R and N.

It is not possible to chose amongst Eqs.(8.75), Eq.(8.77) and Eq.(8.81) which one gives the best result, especially concerning the systematics. This should be done using a sample of real data but was not performed during this work. Due to lack of time, the main effort was placed rather on the background analysis than on the determination of the parameters R and N. Therefore it is not yet possible to conclude which asymmetry is the best.

8.4 The reconstruction algorithm: NPRun

8.4.1 Overview

Two kinds of events are recorded : "Single Tracks" (ST) and "V-Tracks" (VT). The first correspond to a charged particle flying through one tracking detector, and reaching the hodoscope without being back-scattered on the Pb-foil. The second are associated with electrons which are back-scattered and fly again in the tracking detector before crossing the second one and stopping in the second hodoscope.

The events are reconstructed by an algorithm called NPRun, written in C++. This program is taking the raw data from the acquisition (TDCs and ADCs signals) and reconstructing events, recorded in files using the Root [44] format. It is thus the analysis cornerstone since all the analysis programs developed for this experiment use these Root files. It was initially developed by M. Janousch. His work was continued by C. Hilbes, followed by A. Kozela with help of J. Pulut. It is still under constant improvement. During my work on the analysis, I was mainly a user of this software which led me to the discovery of few bugs in the program. A raw description of the algorithm is given on Fig. 8.2.

NPRun considers an event as a possible ST if:

- One and only one track is reconstructed on each projection plane for only one side.
- No Tracks are reconstructed on any plane of projection on the other side.
- One photomultiplier delivers a signal on the side of the track

Likewise, the algorithm will see an event as a VT if:

- Up to three tracks are reconstructed on each projection plane, on one side.
- One and only one track is reconstructed on each projection plane on the other side.
- One PM delivers a signal on the other side.

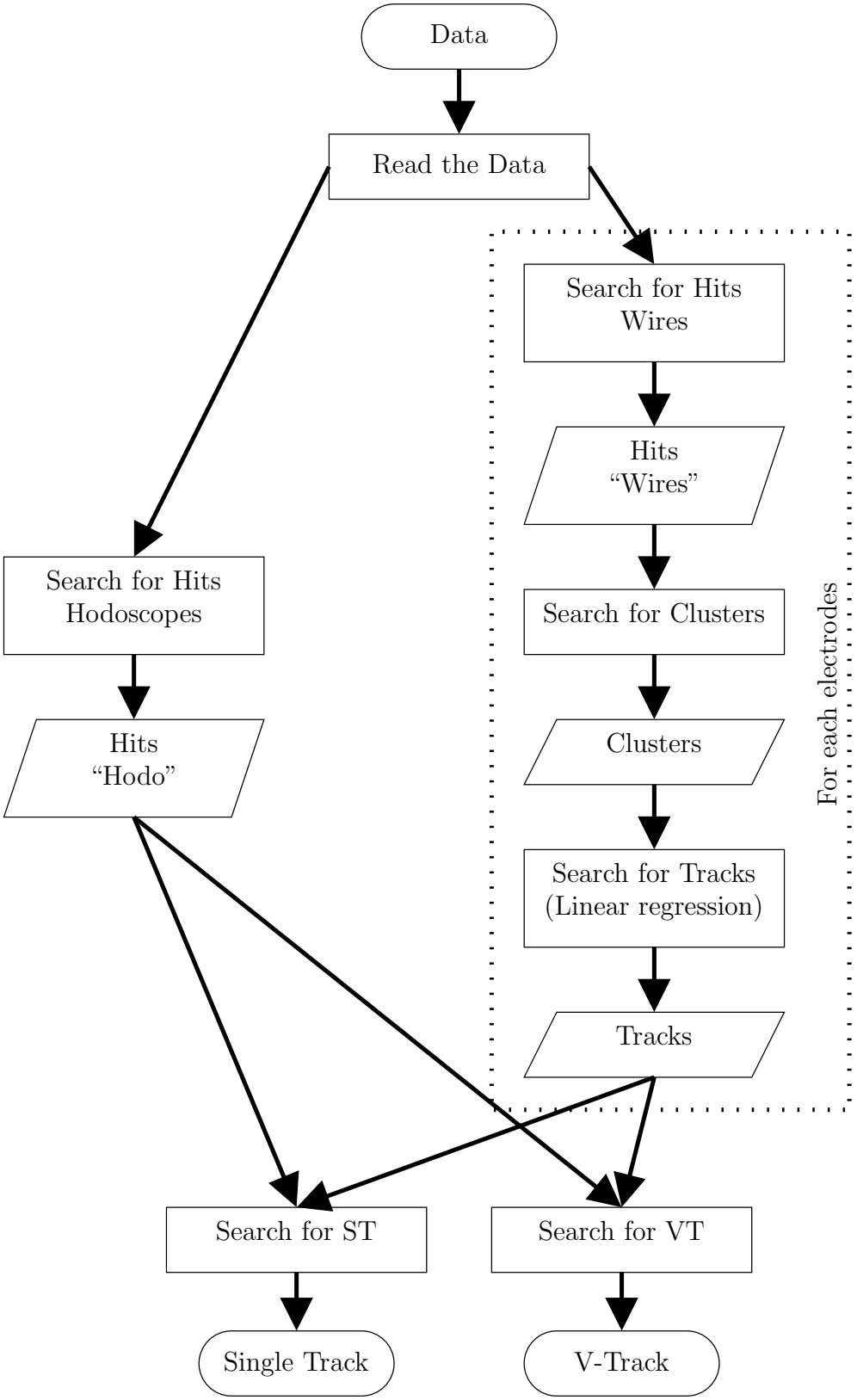

Figure 8.2: Flowchart representing the event reconstruction process.

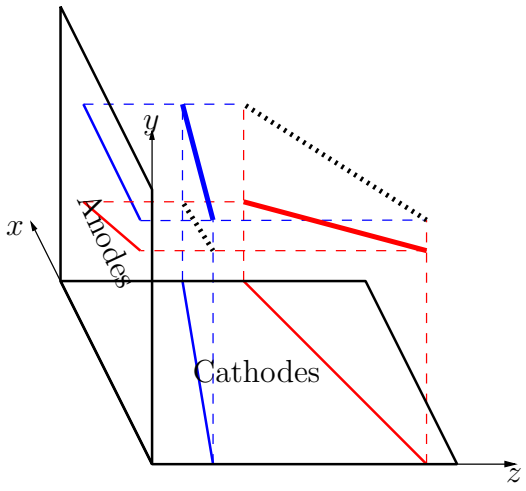

Figure 8.3: Illustration of the reconstruction ambiguity when more than one track is detected in a MWPC. Here, two particles (red and blue) are flying through the detector. Each particle is detected by the electrodes, giving the corresponding projections. Without further information, the algorithm can either reconstruct them correctly, or reconstruct the dotted tracks.

The limit over the number of reconstructed tracks on each detector is the consequence of a limitation in our setup. The point to be remembered is that the MWPCs give projections of the tracks on two perpendicular planes. Therefore if more than one track is recorded an ambiguity of reconstruction appears, illustrated by Fig. 8.3.

This ambiguity needs additional information to be lifted. The position information provided by the hodoscope is not accurate enough to rely on, so it is not possible to deal with events consisting of several tracks on only one side. In the case of VT, the program can use events with three tracks on one side and one on the other side. The tracks intersections on both projection planes and the additional track on the other side are then used to lift the ambiguities. These few requirements do not give us satisfactory reconstructed events. Several additional criteria are applied, gathered in the so-called "EventQuality" (ST and VT) and "Quality" (VT only).

8.4.2 Quality of the Single Tracks

The "EventQuality" concerns the reconstruction of the Tracks. The meaning of each bit of the Single Tracks "EventQuality" is summarize in the table 8.1. Each criterion is described below, using an example of ST (Fig. 8.4). In this example, the electron is detected by the detector 1. This side will then be called "detection side" whereas the other side is the "opposite side".

The meaning of each bit in the parameter *EventQuality* is:

0. Veto hodoscope
   If one signal is given by one scintillator from the opposite side, this flag is set to "0". Since it could mean that the event comes from the outside of the experiment, this criterion is a veto. In the example the criterion is fulfilled and $EventQuality(0) = 1$.

1. Only one scintillator delivers a signal
   It is not possible to reconstruct completely a track, especially if the electron is

Bit	EventQuality
0	No Veto hodoscope
1	Only one scintillator firing
2	Coherency Track/Hodoscope
3	
4	
5	Veto MWPC chamber (Cathode)
6	Veto MWPC chamber (Anode)
7	Stesalit Veto

Table 8.1: "EventQuality" for Single Tracks: meaning of the different bits

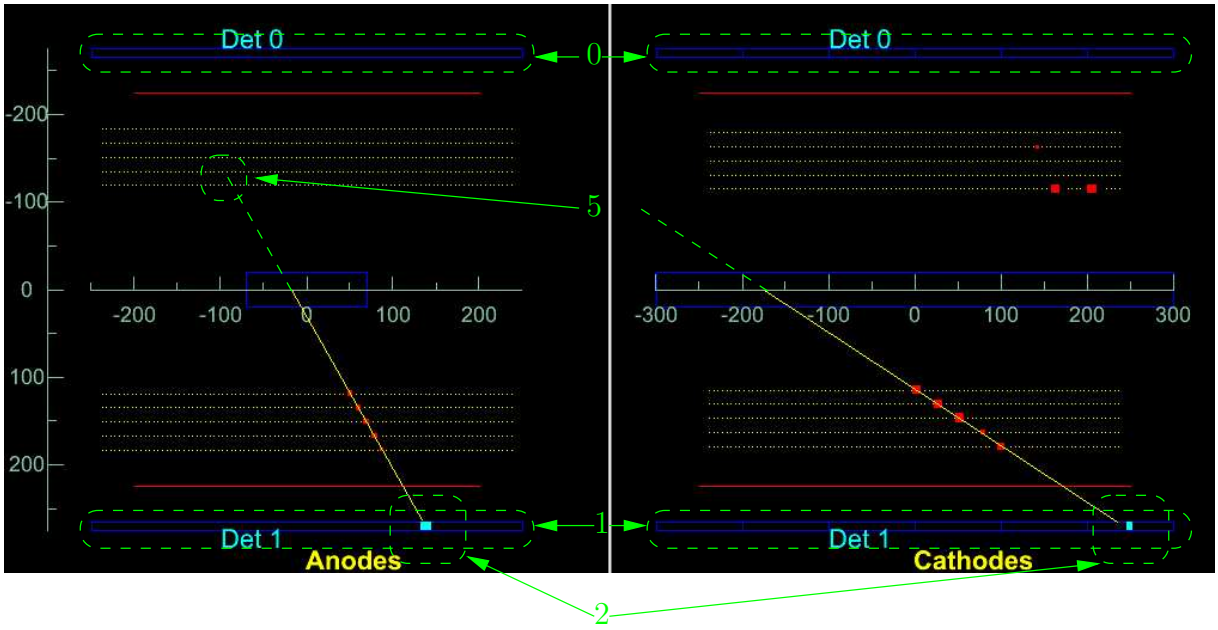

Figure 8.4: Example of Single Track with the corresponding criterion

scattered forward by a wire, a window or the Pb-foil. There, it was decided to reject events were more than one scintillator is delivering a signal on the detection side. The high statistics of ST allows this strong condition. In the example the criterion is fulfilled and $EventQuality(1) = 1$.

2. Coherency track/hodoscope
   The experimental setup allows a rough localization of the light emission in the hodoscope wall. First, the z-coordinate is given by the position of the fired detector. Secondly, the comparison between both photomultipliers of the scintillator gives a rough estimate of the y-coordinate. This position of emission has to be coherent with the reconstructed track. Here the criterion is fulfilled and $EventQuality(2) = 1$.

5. MWPC Veto (Cathode)
   This veto aims at the rejection of the tracks coming from the opposite chamber. Each projection is extrapolated up to the first and second active cathode of the opposite

MWPC. If one of these planes gives a signal coherent with the extrapolation, the signal is assumed to be emitted in the opposite detector and therefore rejected. In the example, the opposite MWPC does not deliver in the surrounding of the extrapolation so that $EventQuality(4) = 0$.

6. MWPC Veto (Anode)
   Similar to the previous one, this veto concerns the first and second opposite anode planes. In the example, $EventQuality(5) = 0$.

7. Stesalit Cut
   The purpose of this cut is to reject the tracks emitted in the MWPC which is detecting the trajectory. If one of the reconstructed projections crosses the Stesalit frames of the MWPC, it can be either stopped there or emitted from the frame. In both cases, such an event is rejected. In the example none of the tracks crosses the frames so $EventQuality(6) = 0$.

Therefore, a good Single Track has an *EventQuality* "00000111" (=7).

8.4.3 Quality of the V-Tracks

Since "EventQuality" concerns the reconstruction of the tracks, it is similar for V-Tracks and for Single Tracks. The parameter "Quality" is dedicated to the description of some criteria related to V-Tracks exclusively. Table 8.2 summarizes the meaning of each bit of

Bit	EventQuality	Quality
0	No Veto hodoscope	One vertex found
1	Only one scintillator firing	Matching Cathode
2	Coherency Track/Hodoscope	Matching Anode
3	Horizontal VT	Multiple Vertex
4	Vertical VT	Multiple Matching Cathode
5	Veto MWPC chamber (Cathode)	Multiple Matching Anode
5	Veto MWPC chamber (Anode)	
7	Stesalit Veto	

Table 8.2: "EventQuality" and "Quality" for V-Tracks: meaning of the different bits

these two criteria. Again, their thorough descriptions rely on a V-Track example (Fig. 8.5). The "scattering" side and the "opposite" side are then respectively the detector 0 and the detector 1.

The meaning of each bit in the parameter *EventQuality* is:

0. Veto hodoscope
   For V-Tracks the veto is triggered by the scintillator wall on the scattering side. This example does not fulfill this condition so $EventQuality(0) = 0$.

1. Only one scintillator delivering a signal
   This criterion is similar to the one used for ST and it concerns the scintillator wall on the opposite side (since it is the one which detects the electron). The condition is fulfilled here and $EventQuality(1) = 1$.

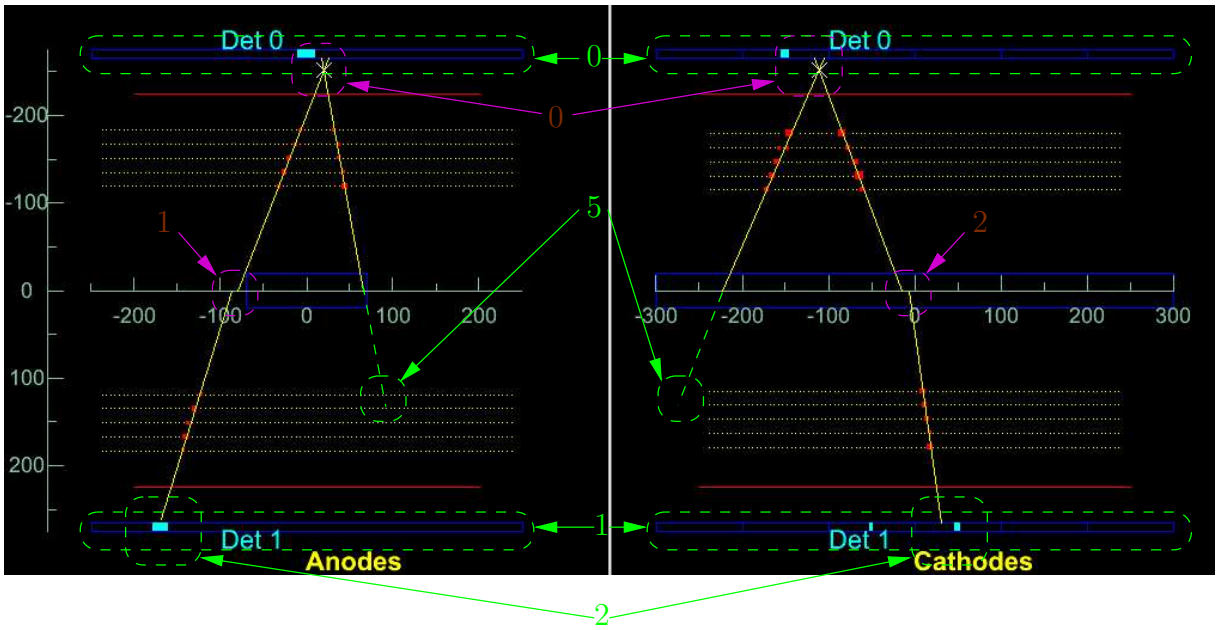

Figure 8.5: Example of V-Track with the corresponding criteria: green for "EventQuality" and purple for "Quality".

2. Coherency track/hodoscope
   This criterion is the same as the one used for ST. In this example, the track and the signal from the hodoscope are coherent, so the $EventQuality(2) = 1$.

3. Horizontal and vertical V-Track
   This happens when a V-Track can be reconstructed only in one projection. On the other hand, a track must be reconstructed in both detectors. In principle these events should be the best for the measurement of R and N since they maximize one component and cancel the second one. Unfortunately, a large part of them are accidental coincidences. Therefore it was decided to reject these events. The example is neither a vertical nor an horizontal V-Track so $EventQuality(3) = 0$ and $EventQuality(4) = 0$.

4. MWPC Veto (Cathode)
   This Veto is similar to the one used with ST. It concerns the short-arm of the V-Track, considered as the emission trajectory. In the example, this veto is not triggered then $EventQuality(5) = 0$.

5. MWPC Veto (Anode)
   This Veto is similar to the one used with ST and it is again applied on the short arm of the V-Track. In the example, this veto is not triggered then $EventQuality(6) = 0$.

6. Stesalit Veto
   This veto is the same as the one used with ST. Here no tracks crosses the Stesalit frames so $EventQuality(6) = 0$ and $EventQuality(7) = 0$.

The meaning of each bit in the parameter *Quality* is:

0. One vertex found
   This criterion concerns the track intersections (called "vertex") in both projections. This flag is set to "1" if there is at least one coherent couple anode/cathode. It is the case here, so $Quality(0) = 1$.

1. Matching projections on cathodes
   In the cathode projection, one track on the scattering side and another on the opposite side must be coherent. This condition is fulfilled in the example and $Quality(1) = 1$.

2. Matching projection on anodes
   In the anode projection, one track on the scattering side and another on the opposite side must be coherent. This condition is fulfilled in the example and $Quality(2) = 1$.

The bits 3, 4 and 5 are activated if more than one couple of track fulfill the previous conditions, which is possible only when three tracks are reconstructed on the scattering side. Since it is not the case here, $Quality(3) = 1$, $Quality(4) = 0$ and $Quality(5) = 0$.

A good V-Track has then an *EventQuality* of "00000111" (=7) and a *Quality* of "00000111" (=7). The example has a Quality 7 but an EventQuality 6 (Veto from hodoscope). It is then considered as scattered by a scintillator and thus not accepted for the calculation of the parameters R and N.

8.5 Background

The asymmetries calculated in the previous chapter are valid only if the measured rates are built with electrons coming from the neutrons decay. In the following, they will be called "signal". Since the neutrons are flying in an He-filled volume, some of them are scattered and induce (directly or indirectly) a "background" of electrons in the surrounding of the beam. The majority of these electrons have different characteristics from the signal and therefore can be rejected by applying cuts in the data. However, the other part can not be neglected and must be evaluated in order to be taken into account in the calculation of the asymmetries.

8.5.1 Cuts

The rejection of the well reconstructed events are defined according to:

- the energy
- the position of emission
- the position of scattering

The analysis uses two levels of cuts. The first one actually rejects events meaningless for the measurement, for instance the events with an energy higher than 2 MeV and events coming from positions very far from the neutron beam. The second level is a selection: events which do not fulfill the conditions of good events are not definitely rejected but will be used further in the analysis for the background evaluation. The events kept at the

end of the cuts will then be a mixture of electrons coming from the neutron β-decay and background.

8.5.2 Energy and emission position

The neutron β-decay end-point is 782 keV.

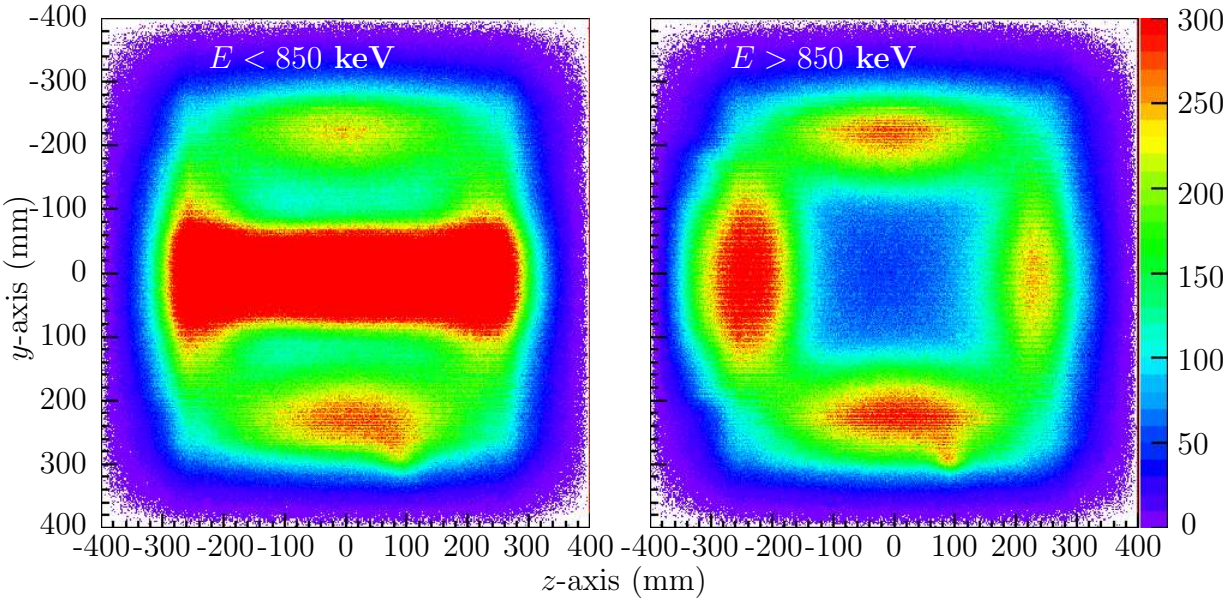

Figure 8.6: Emission distribution for energies lower and higher than 850 keV. The distribution is observed on the plane $x = 0$. The beam is clearly visible for energies lower than 850 keV but disappeared completely for energies above 850 keV.

The Fig. 8.6 shows the distribution of the intersection between Single Tracks and the plane $x = 0$ mm for energies lower and higher than 850 keV. For high energy, the signature of the beam vanishes. In the following, 850 keV will be used as the limit energy of the electrons coming from the beam.

If one assume that a given material produces a background which spectrum is independent to its closeness to the beam, it is possible to normalize the background using the high energy contribution ($E > 850$ keV). Therefore, the difference between both graphs in Fig. 8.7 should correspond to the contribution of the beam.

This picture shows that the beam is localized between $y = -100$ mm and $y = +100$ mm. It corresponds to the beam geometry assumed according to the collimator and neutron guide geometry.

This picture shows also the limits of this normalization method which assumes that the background spectrum has the same shape from every place in the detector. The white areas correspond to overestimations of the high energy contribution and some underestimations are also visible. Thus this assumption is limited to some places close to the beam.

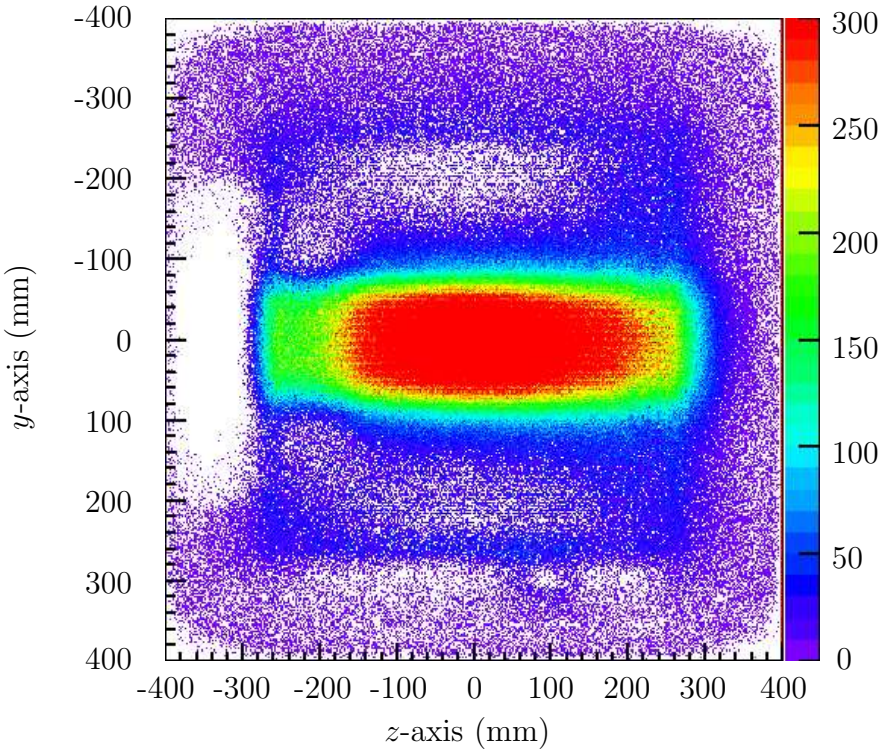

Figure 8.7: Subtraction between low- and high-energy contributions.

8.5.2.1 Position of scattering

The interesting scattering events are produced on the Pb-foils. Other events are scattered by the surrounding material, including hodoscopes and MWPC wires. Since the Pb-foil is well defined on y and z, it is possible to reject the events whose scattering coordinates are not in the area $(y, z) \in [-250, 250] \times [-230, 230]$ mm^2.

The Pb-foil is localized at $x = \pm 225$ mm. Since the probability to an electron to be back-scattered by the Pb-Foil is less than 10^{-3}, the foil does not change the contribution of its surroundings. Therefore, the measurement made with the foils OUT provides the information about the contribution of the surroundings.

8.5.3 Background evaluation

Once the cuts are made, the sample of data contains a mixture of signal and background. The events accepted by the cuts belong to one of the following categories:

- Electron emitted by a neutron decay and scattered on the Pb-foil (Interesting events, referred as "signal" in the following)
- Electron emitted by a neutron decay and scattered by the surrounding of the Pb-foil (Background)
- Electron emitted by the surrounding of the neutron beam and scattered by the Pb-foil (Background)

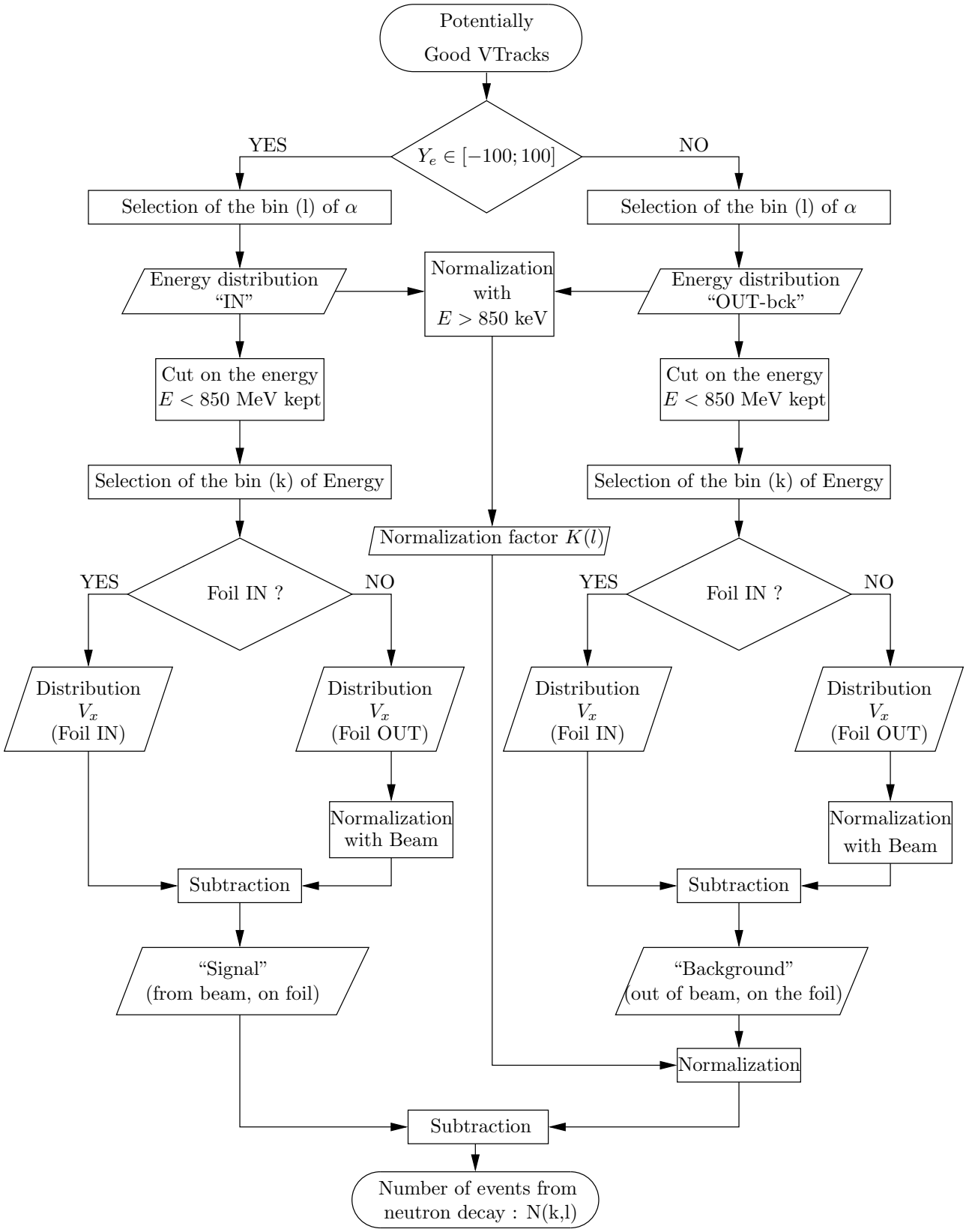

Figure 8.8: Principle of the background subtraction

- Electron emitted by the surrounding of the neutron beam and scattered by the surrounding of the Pb-foil (Background)

It is not possible, for a given event, to know to which of these four categories it belongs. However, a procedure of background subtraction was elaborated to evaluate the *number of events* emitted by the neutron β-decay and scattered on the Pb-foil (Fig. 8.8).

8.5.3.1 Evaluation Beam IN/OUT

In the following, the events apparently coming from the beam will be referred as "IN-events". Thus they can be distinguished between signal ("IN-s") which corresponds to electrons actually emitted by the neutron beam, and background ("IN-bck") corresponding to electrons emitted by the surrounding. On the other hand, the events apparently coming out of the beam will be called "OUT-bck" (Fig. 8.9).

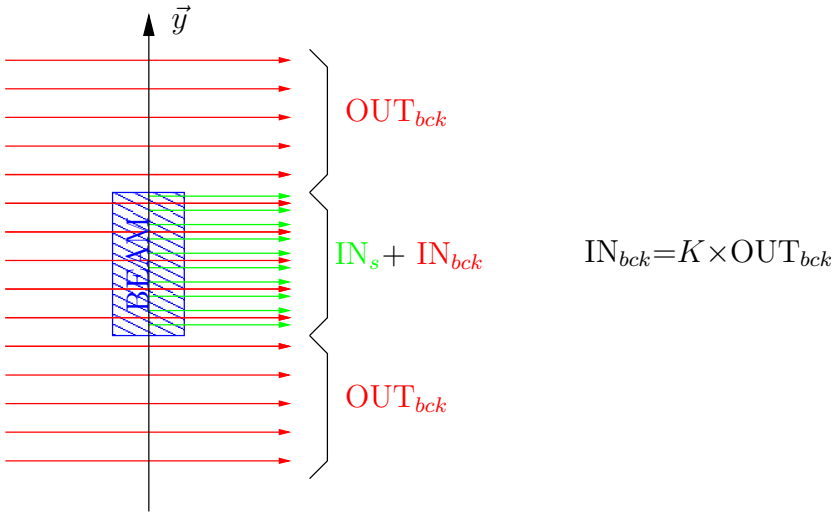

Figure 8.9: Composition of the events emitted ; definition of "IN-events" and "OUT-bck"

The background spectrum is assumed to be homogeneous, whether it crosses the beam or not. It is then possible to use the high energy events to evaluate the background contribution in the emission (Fig. 8.10). The ratio between the number of events above 850 keV determines the normalization factor, called K.

As it was seen on Fig. 8.7, the assumption other the background homogeneity is valid only locally. Thus the events "OUT-bck" are limited to $|y_e| \in [100; 200]$. For the same reason, in the following the events "IN" and "OUT" will be chosen with $z_e \in [-200; 200]$.

In order to check the coherence of this method, it is possible to use the result of the subtraction of the normalized "OUT-bck" from "IN-events". This distribution should be consistent with the energy distribution from the neutron beta decay convoluted with the Mott scattering cross section and analyzing power and the response of the plastic scintillators. This test was performed with success with Single Tracks [42], but not yet with VTracks.

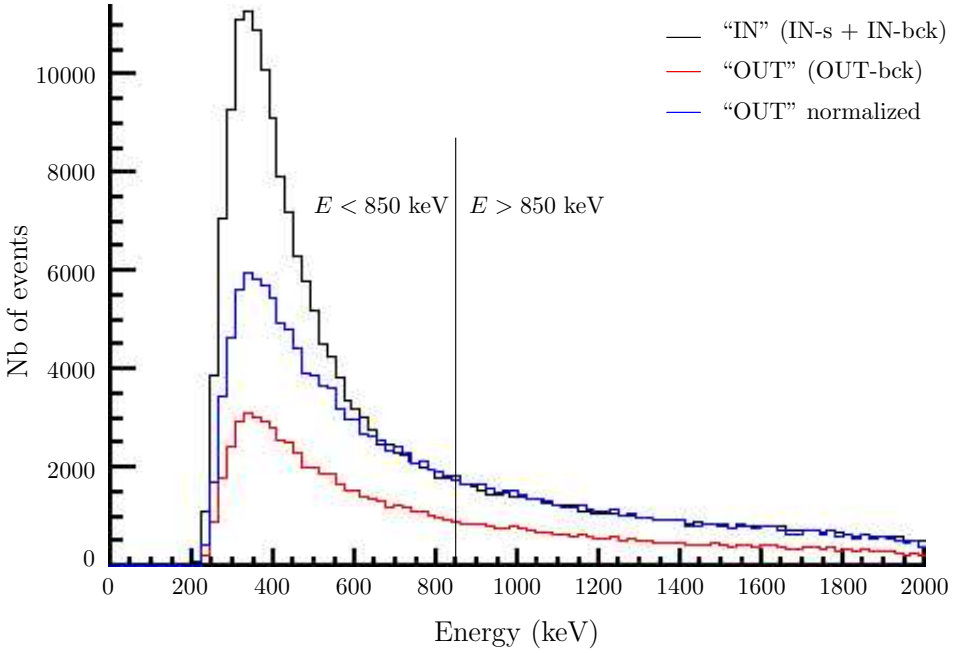

Figure 8.10: Normalization of the background using the energy spectra and calculation of K.

8.5.3.2 Number of events scattered on the Pb-foil.

The second step is to find the fraction of electrons actually scattered by the Pb-foil for electrons "IN-s" and "OUT-bck"[1]. This is done by the comparison between the distribution of the scattering x-coordinate between "foil IN" and "foil OUT"(Fig. 8.11).

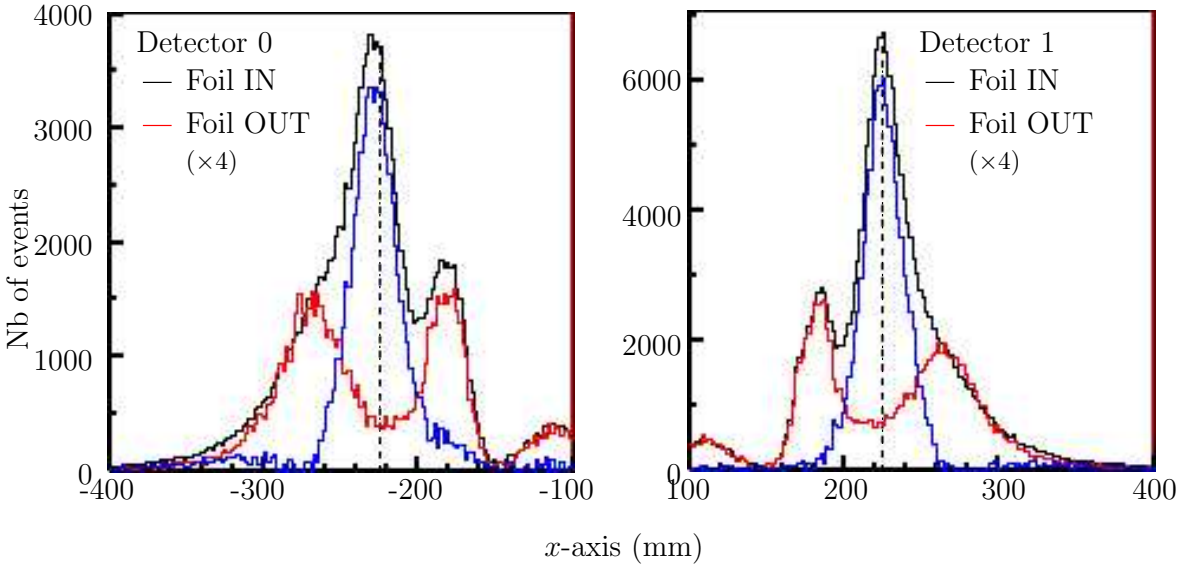

Figure 8.11: Distribution of the x-coordinate of the scattering for foil IN and foil OUT (normalized). The dotted line represents the theoretical position of the Pb-foil.

[1]Since the area were "OUT-bck" are coming from is close to the origin of "IN-bck", the scattering behavior of "IN-bck" and "OUT-bck" is assumed to be equivalent.

The normalization between these two spectra is performed using the proton beam integrated over the measuring time. The result is then a number of events scattered on the Pb-foil for the electron "IN-s" and "OUT-bck".

8.5.3.3 Evaluation of the signal

The first step gives the ratio (K) between the background electrons and the electrons coming from the β-decay and the second step provides the number of electrons from each origin scattered on the Pb-foil, N_{beam} and $N_{background}$ respectively. The number of events produced by the neutron β-decay and scattered on the Mott target is then :

$$N = N_{beam} - K * N_{background} \tag{8.83}$$

For a given electron emission $\vec{p}_e$, there is no reason to believe that the relative behavior of the signal and of the background are the same for different values of α (defining the scattering plane) and of the energy and thus this operation must be performed on every bin of energy (k) and α (l) defined previously.

8.6 Source localization using tomography

8.6.1 Principle

The tracking detectors are sensitive only to the trajectory of the electrons and no information is available about the position of emission along this trajectory. In order to study how the electrons are emitted, it is then necessary to define a plane, and to observe the distribution of *the intersection between the trajectories and the plane.* For instance, the plane $x = 0$ mm is used for the study of the electrons emitted by the beam and the cut of the background coming from the opposite side of the HeBox is performed on the plane $x = \pm 85$ mm. Figure 8.12 shows the intersection between the plane $x = 0$ mm and the well reconstructed Single Tracks with an energy lower than 850 keV. The beam is clearly visible between $y = \pm 100$ mm.

This is not satisfactory if an unknown source has to be investigated. On this figure for instance, there is apparently two sources: one on the top and one on the bottom. However it is not possible to decide whether it is a wide source localized also in the vicinity of the plane or a small source but not focused on this plane.

In order to localize the sources, a tomography-like method is used. It is possible to define several parallel planes and study how the events are focused (Fig. 8.13(a)). This method is very efficient when the source is small and strong enough to overwhelm others. It can be used to roughly estimate the position of the source. It is also possible to select several ranges of incidence angles and, for a given plane, to look at the respective positions of the spots (Fig. 8.13(b)). When the source is not on the chosen plane, it is differently localized according to the choice of the incident angle. When a large range of angle is available, this method gives very satisfactory result since the position shift becomes very obvious when the plane of study is not well chosen. The side effect is that this method can be biased when the trajectories are screened by some parts of the experiment.

The direct information provided by the tracking detector are the projections of the trajectories horizontally and vertically. It is then convenient to use as "incidence angle"

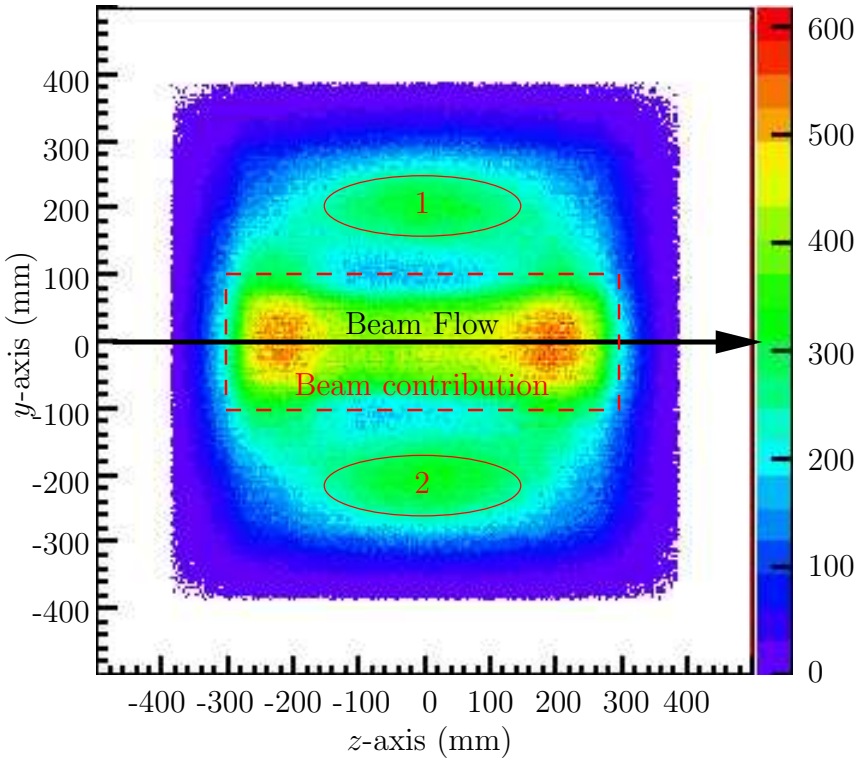

Figure 8.12: Intersection between the tracks seen by detector 0 (Energy < 850 keV) and the plane x=0 mm. It is possible to see the contribution of the beam $y = \pm 100$ mm and two possible sources (1 & 2) on top and bottow.

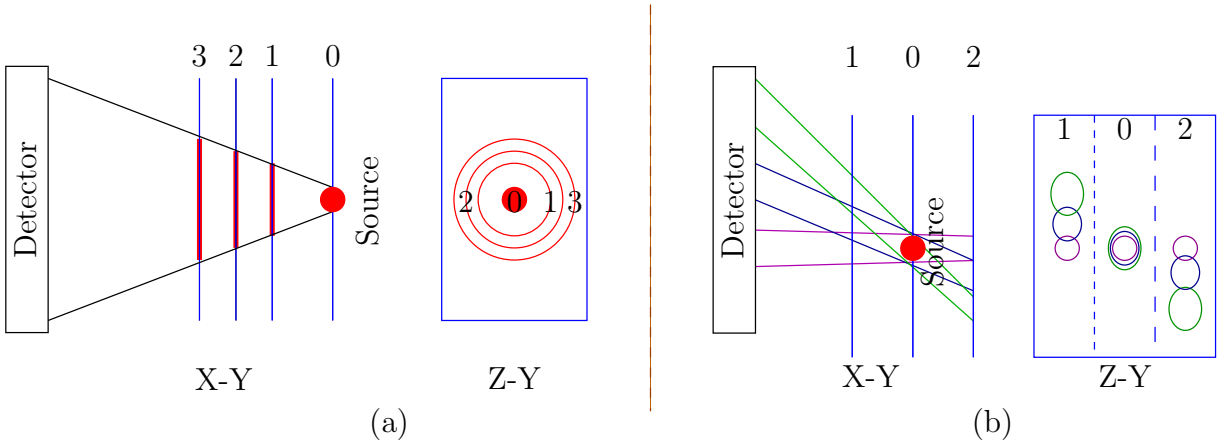

Figure 8.13: Tomography: (a)Localization of a source using several planes of visualization ;(b)Localization of a source using several angles of incidence.

(φ) the angle between the projection and the x-axis, without additional conditions on the second projection.

8.6.2 Limits of the method

This identification method is limited by the detector geometry. It is possible that a source would not be visible with a large enough range of angle, and then the tracks convergence would not be strong enough to find the source.

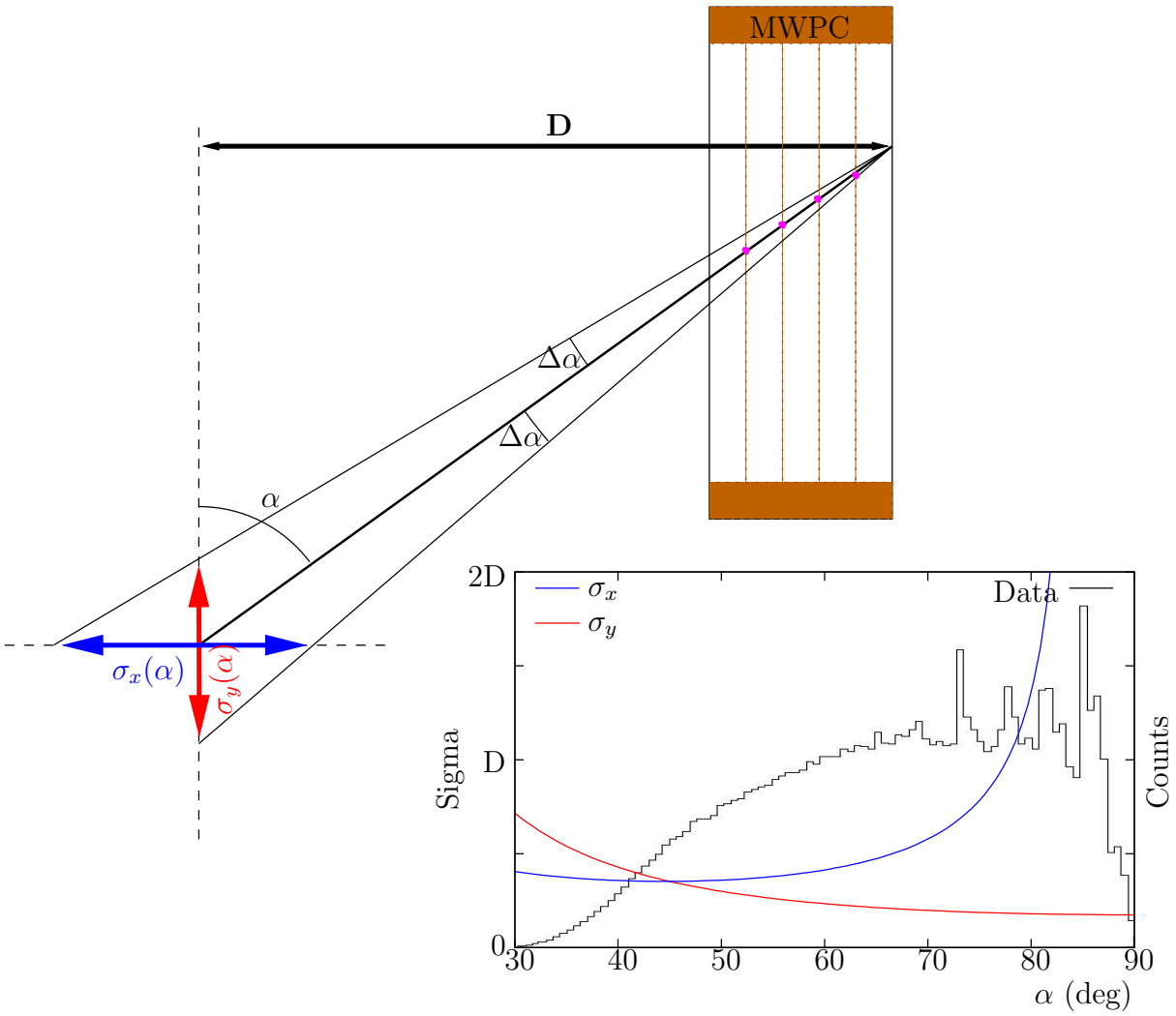

Figure 8.14: Influence of the emission angle on the tomography resolution for both x and y direction of study. The graphs were created with a acceptable reconstruction resolution of $\Delta\alpha = 5°$. The third graph represents the typical distribution of emission angle in real data.

More disturbing, the resolution of the spot reconstruction depends on the studied plane and on the angle of emission (γ or θ in Fig. 8.1). In the following, we will refer to these angles as α As one can see in Fig. 8.14, the data recorded has an emission angle γ larger than 45°. For this kind of events, the resolution along σ_y is better than the resolution along σ_x. If this result is transposed to the experimental setup, it means that the tomography resolution is better on the planes (YZ) than on the planes (XY) and (XZ).

Chapter 9

Background study

This chapter presents the results of the investigation of the background produced by charged particles associated with scattered neutrons. They are follow by a discussion concerning the different behavior between the background recorded with Single Tracks and V-Tracks.

9.1 Analysis with Single Tracks

A major issue in the analysis concerns the background. It is indeed possible to subtract its contribution in the measured rates, but this procedure needs a precise knowledge of the source. Using the tomography-like method, a thorough study of the background sources has been performed over the data recorded in 2004. Additionally, the result of this study can be used to improve the detection system before the next run, expected in summer 2006.

Ideally, this study should be made with V-Tracks. However, due to the low statistic of these events, Single Tracks are used. It is assumed that the sources of electrons are the same for both kinds of events. However, one must remember that because of the scattering cross section, the acceptance of the detector is not the same for Single Tracks and for V-Tracks.

The background study was thus made with electrons with energy larger than 850 keV. As it was seen in the previous chapter, these events cannot be emitted by neutron β-decay.

In the following, the ST used will be the well reconstructed ones, with E¡ 2 MeV. In order not to bias the study of background, the veto from the opposite MWPC and the "Stesalit Veto" are not activated at first. Their effect is investigated separately.

9.1.1 Tomography with the planes (Z, Y)

Like it was seen in the previous chapter, the ranges of incidence angle available provide the best resolution for these planes of study.

The distribution of the tracks crossing the plane $x = 0$ mm is showed on Fig. 9.1. Four areas can be distinguished. Due to their localization, they do not have the same impact on the analysis: the sources 1 and 2 are well separated from the beam and can be "easily" cut out from the data, whereas 3 and 4 are completely mixed with the beam and need a careful evaluation before being subtracted.

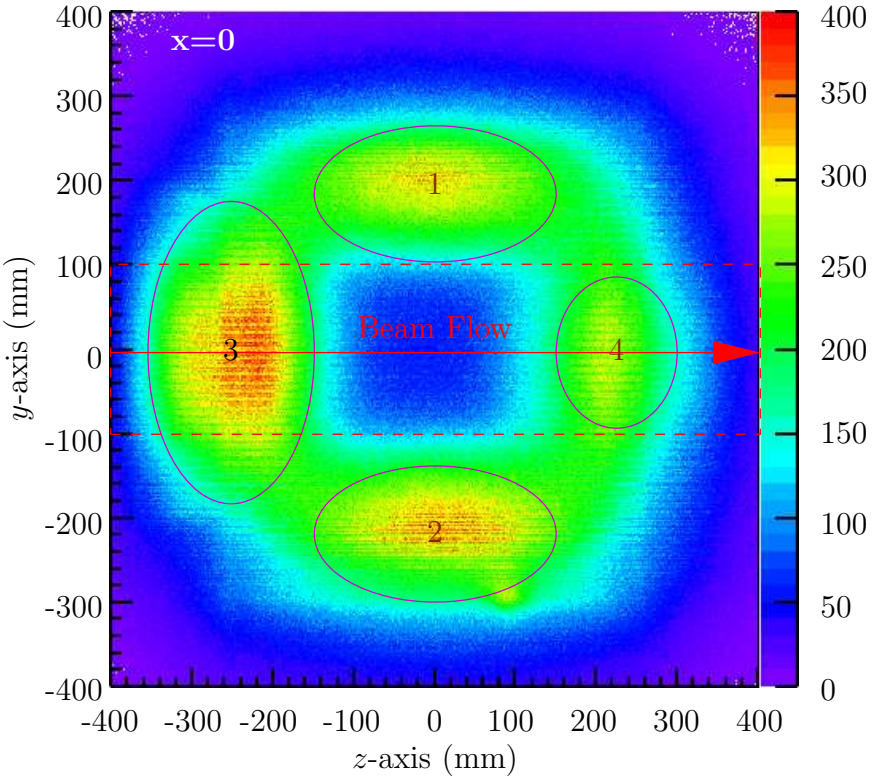

Figure 9.1: Distribution of the background events (E > 850 keV) in the plane $x = 0$ mm. These events were detected by the detector 0. The dashed line represents the limits of the beam.

None of them is very well localized. The reason can either be that the sources are broad or that the plane $x = 0$ is not the one where the background is emitted. However, there is nothing but Helium in the vicinity of the beam. Since the area $[-100; 100] \times [-100; 100]$ mm^2 is almost empty of background, the Helium cannot be the main source of electrons. Therefore it must be searched somewhere else, where there is more material. A cross section of one side of the experimental setup is showed on Fig. 9.2.

The first notable place is the limit of the HeBox $|x| = 85$ mm. Figure 9.3 shows the distribution of the intersection between the tracks recorded by detector 0 and the planes $x = -85$ and $x = 85$ respectively. For $x = -85$ mm, the area 3 is well localized near the inner edge of the MWPC, like the areas 1 and 2 for $x = 85$ mm. Since these positions correspond respectively to vertical and horizontal planes, it seems appropriate to use the plane $z = -250$ mm for the study of the source 3 and the planes $y = -250$ mm and $y = 250$ mm for the sources 1 and 2 respectively.

This figure provides two additional information. On $x = -85$ mm, it is possible to see that some tracks are recorded *outside* the black line representing the limits of the detecting MWPC window. These events thus are emitted *inside* this MWPC. On $x = 85$ mm, on can see that the major part of the events from area 1 and 2 are detected *inside* the full line representing the window of the opposite MWPC. The events are thus emitted *inside* this chamber.

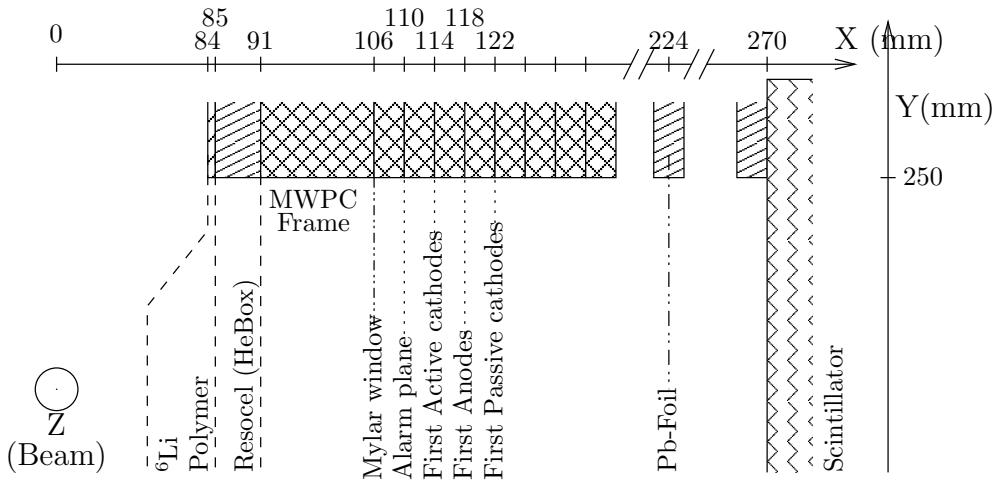

Figure 9.2: Cross section of the detector 1 along the X-coordinate at $z = 0$ mm. The position of the main parts of the detector are indicated. The detector 0 is symmetric with respect to the plane $x = 0$ mm.

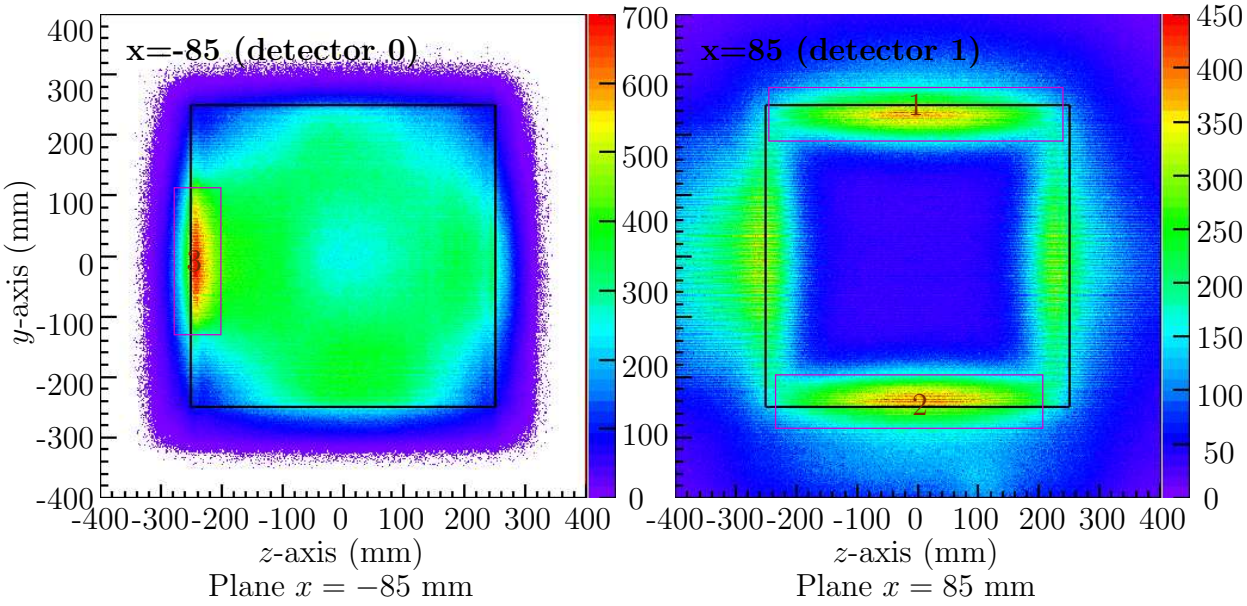

Figure 9.3: Study of the background recorded by the detector 0 in the plane $x = -85$ mm (left), close to detector 0, and $x = 85$ mm (right), close to detector 1. The thick black square represents the opening of the closest detector.

9.1.2 Tomography with the planes (X, Z)

These planes are particularly suitable for the study of the inner part of the MWPC, on the top and the bottom. The incidence angle used here is the angle between the projection provided by the anodes and the x-axis.

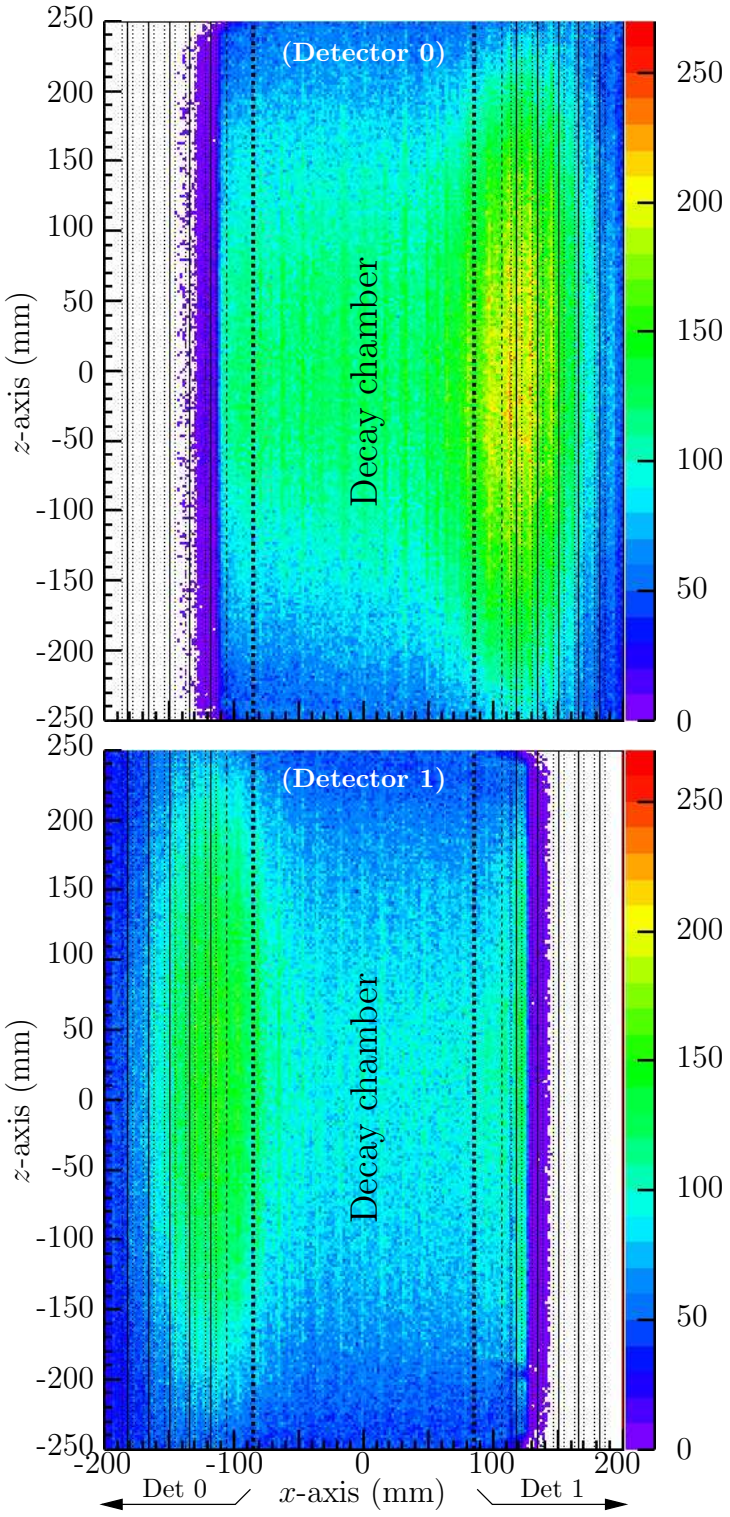

Figure 9.4: Map of the tracks in the plane $y = 250$ mm. The scale is the same for both detectors. The thick dashed lines represent the limits of the HeBox. The thin ones are the Mylar windows of the MWPC. The solid and the dotted lines represent the electrodes, with respect to their orientation toward the plane of measurement.

9.1.2.1 Plane $y = 250$ mm: Top of the MWPC

Figure 9.4 represents the intersection between the tracks and the plane $y = +250$ mm for both detectors. The background of the area 1 is mainly emitted by the frame of the MWPC, around the position of the first cell of tracking. The difference of statistics between both detectors is to be related to a different efficiency (intrinsic and thresholds).

9.1.2.2 Plane $y = -250$ mm: Bottom of the MWPC

The same procedure is applied on the plane $y = -250$ mm (Fig. 9.5).

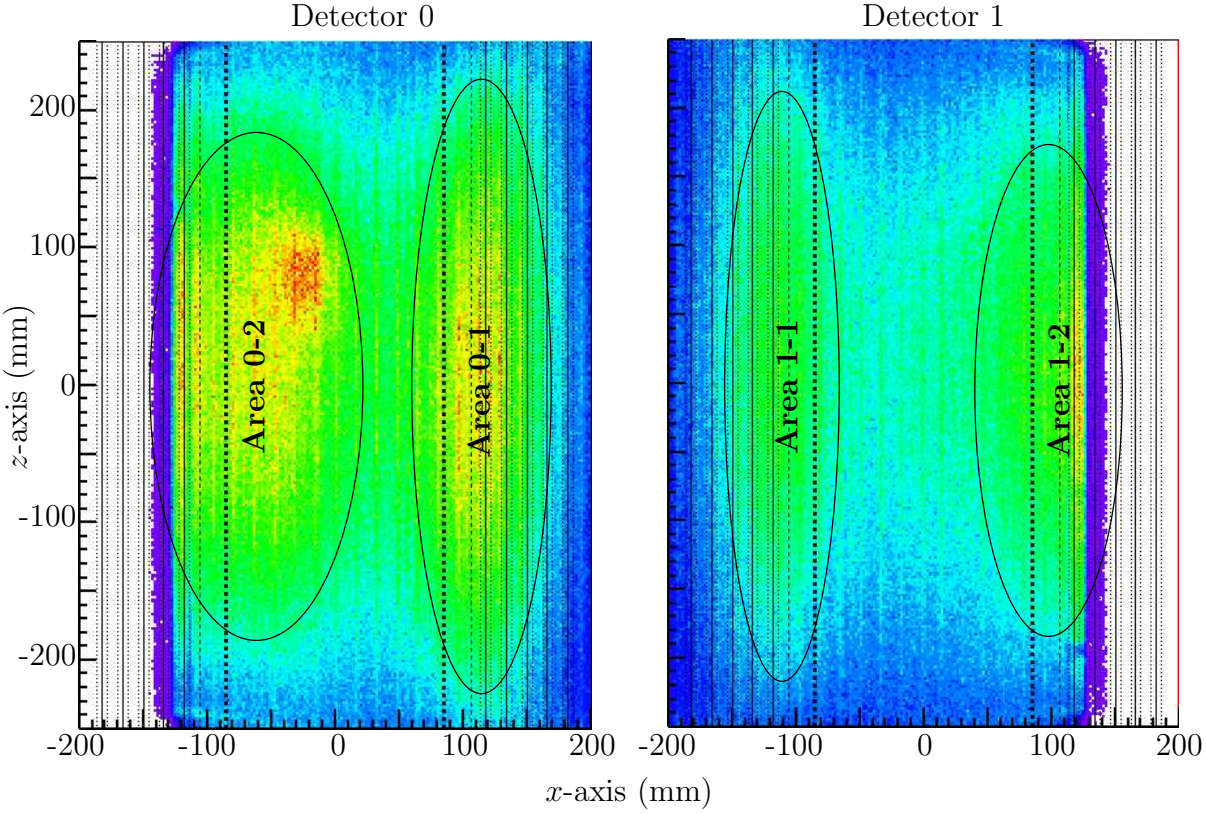

Figure 9.5: Map of the tracks in the plane $y = -250$ mm for both detectors. Two sources are observed by each detector. The description of the sources can be found in the text.

Four interesting areas are visible. The "0-1" and "1-1" seem to correspond to the background source visible on the plane $y = 250$ mm, in the opposite MWPC. The sources "0-2" and "1-2" can be localized on the detecting MWPC frame (between $x = -85$ mm), or lower. The slit opened at the bottom of the HeBox, for example, could produce this background. The spot visible in the area "0-2" is described later in this work.

9.1.2.3 Precise localization with very tilted tracks

In the previous figure, the background sources "0-2" and "1-2" are diffused and it is not possible to know accurately where they are localized. Since they are very close to the detector, it is possible to use very tilted tracks in order to have a better resolution on

these sources. Figure 9.6 presents the distribution of the tracks observed by both detectors

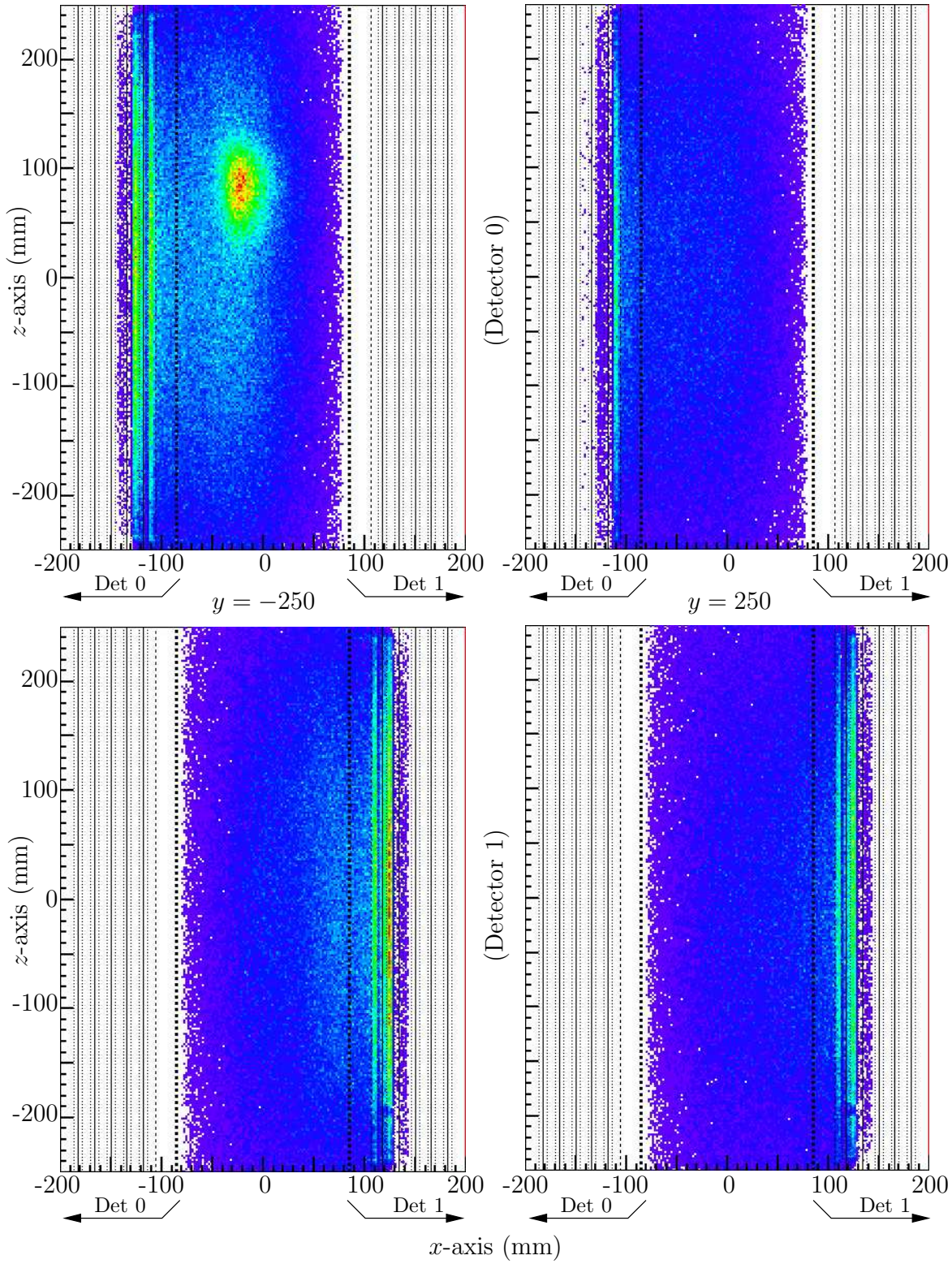

Figure 9.6: Map of the tracks in the plane $y = \pm 250$ mm detected by both detectors. The sample used consists of tracks with an incident angle in $[40, 45]$ mm. The scale is the same for each distribution.

on the planes $y = \pm 250$ mm for tracks with an incident angle $|\varphi| \in [40, 45]$ mm.

One should notice that on every figures but one (Det 0, $y = 250$ mm), two distinct sources are visible inside the detecting MWPC. The first is localized between the Mylar window and the first plane of cathodes; and the second between the first anode plane and the second cathodes plane.

On each of these figures except one, it is possible to see a very sharp limit around $x = -130$ mm (Detector 0) and $x = 130$ mm (Detector 1) where the number of observed tracks suddenly decreases. It is an effect of the conditions of reconstruction: at least a signal coming from 4 planes is requested to reconstruct a ST which seldom occurs when the tracks are emitted further than the first cell of tracking. On (Det 0, $y = 250$ mm) the limit is on $x = -115$ mm and thus only one source between the Mylar window and the first cathode plane is observed. So far no explanation was found.

One should notice the contrast between the background coming from the opposite chamber, broad and intense, and the one emitted inside the detector, well localized and weak. The difference of accuracy is obviously a consequence of the incidence angle. Two explanations about the difference of intensity can be found: i) the background is preferentially emitted towards the opening of the chamber detector where the neutrons came from and ii) the background is emitted isotropically but because of the closeness to the detector, it is difficult to reconstruct the tracks.

9.1.2.4 Bottom of the HeBox

The source called "area 0-2" on Fig. 9.5 contains also a contribution coming from the bottom of the HeBox and this source can be sorted into two kinds. The first one, also visible on Fig. 9.6 (Detector 0, $y = -250$ mm) is very well localized and will be analyzed later in the chapter. The second, very diffuse is so far not well known. It is visible only with tracks whose incident angle $\varphi \in [-40, -20]$ and mainly from detector 0. The use of large incidence angle precises the emission position around $x = -300$ mm and $y = 0$ mm which corresponds to slit opened at the bottom of the HeBox. However, this source is still diffuse and cannot be completely analyzed.

9.1.3 Tomography with the planes (X, Y)

9.1.3.1 Plane $z = -250$ mm

The incidence angle studied here is the angle between the projection given by the cathodes and the x-axis. The result of the intersection between the plane $z = -250$ mm and the Single Tracks (detector 0) with E > 850 keV can be seen on Fig. 9.7. The main source of background is localized in the area "Li0" for the detector 0. One can notice that it is much stronger than the previously studied background. The position of emission corresponds to a piece of ^{6}Li-polymer placed to act as a collimator to absorb the diverging neutrons. The aim was to prevent neutrons to enter in the the MWPC. As one can see on Fig. 9.8, the detector 1 sees a similar source, corresponding to the symmetric piece of polymer. The pieces of polymer were placed in 2003, before the commissioning run. As a consequence, it is not possible to quantify their efficiency and their side effects.

Additional points can be noticed on this plane $z = -250$ mm. In order to have a better view, one can select a range of incidence angle. Figure 9.9 shows the same distribution as

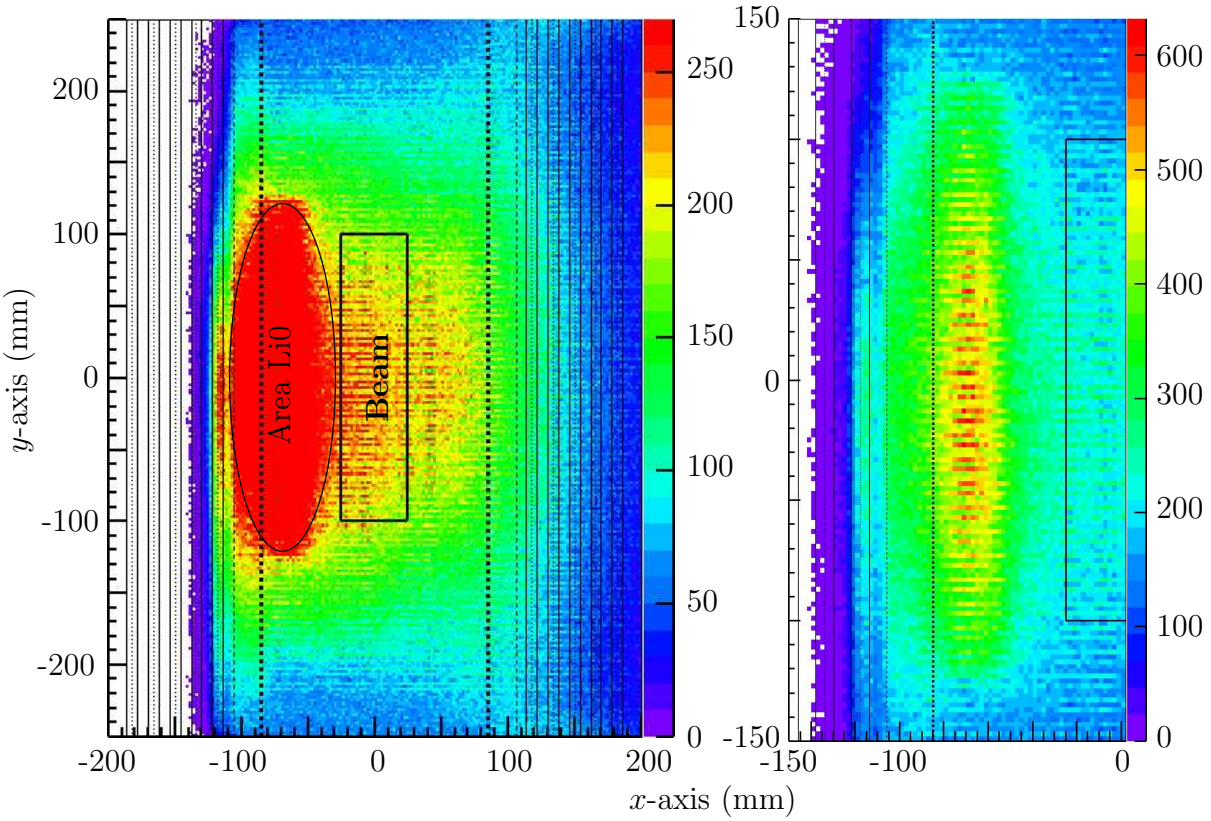

Figure 9.7: Map of the tracks in the plane $z = -250$ mm, detected by detector 0. Left: global distribution with the same scale as on Fig. 9.4. Right: Focus with a different scale on the huge source. Its maximum is localized on $x = -70$ mm.

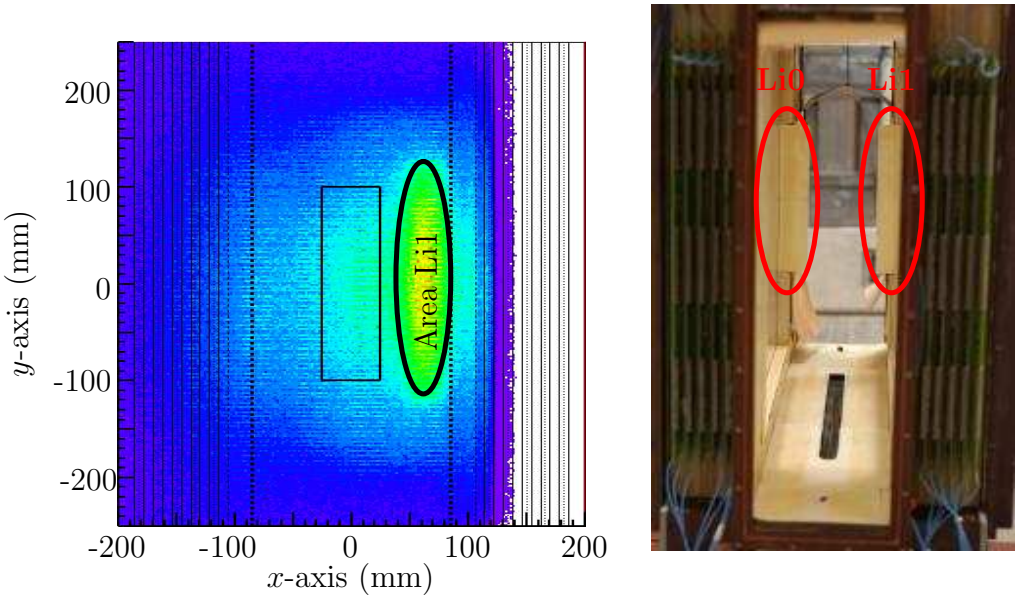

Figure 9.8: Left: map of the tracks in the plane $z = -250$ mm recorded by detector 1. Right: picture of the HeBox, from the beam dump. The Li-doped polymer used as collimator is visible.

Fig.9.7 but only for tracks with an incidence angle in the range $[-35°; -30°]$. Except for

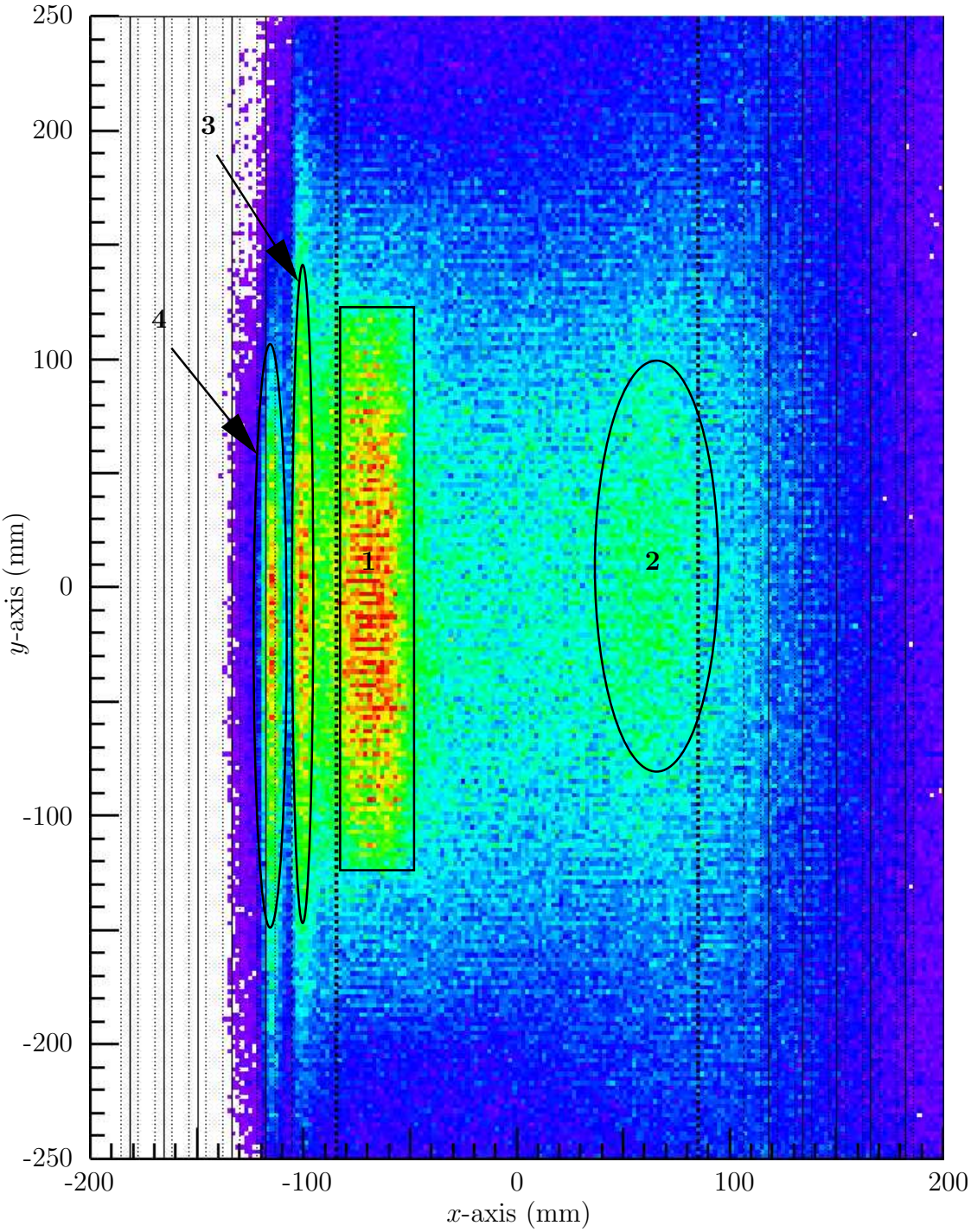

Figure 9.9: Background study on the plane $z = -250$ mm with tilted tracks performed with detector 0. Since only the relative contribution are meaningful, the scale was hidden.

the ^{6}Li polymer already described (1), three additional sources are visible. "2" seems to be the contribution of the symmetrical piece of polymer. It is worth to notice that this source seems very weak, compared to the the same one detected by the other detector. The contributions "3" and "4" are localized along the Mylar window and the first cathode

planes respectively. It is interesting so see that this last contribution is stronger on the bottom than on the top. It even disappear above $y = 100$ mm. A symmetric pattern can be observed with the detector 1.

9.1.3.2 Plane $z = +250$ mm

On the plane $z = 250$ mm, each detector sees two sources of background (Fig. 9.10). One situated inside the opposite MWPC (0-1 and 1-1) and the second localized inside

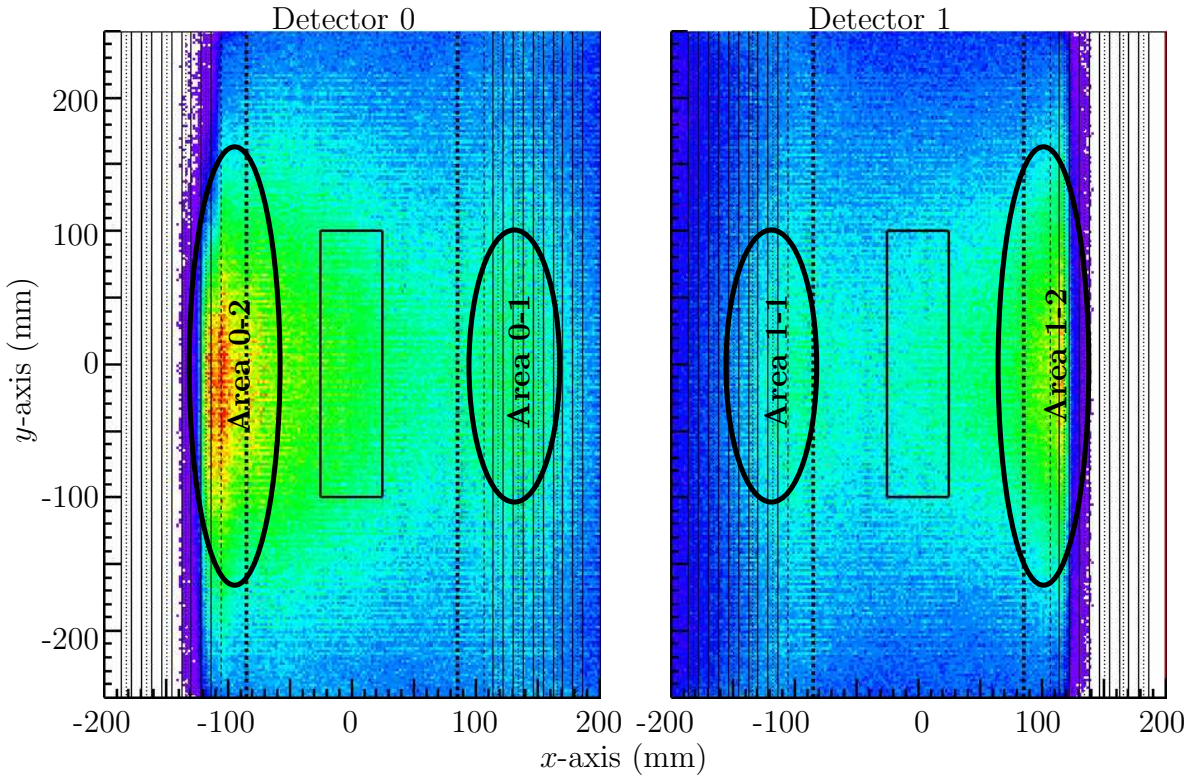

Figure 9.10: Map of the tracks in the plane $z = 250$ mm for both detector. Two sources of background are visible on each detector. The scales are identical to the ones used on Fig. 9.4.

the detecting MWPC, just behind the window (0-2 and 1-2). The first ones seem to be equivalent to the ones already observed on the top and the bottom (area 1 and 2 on Fig. 9.1). Although they are closer to the beam, these two areas appears to emit less background than their equivalent on the top and bottom.

To study the areas 0-2 and 1-2, it is necessary to use ST with a large incidence angle (Fig. 9.11).

This background consists of a mixture of three distinct sources (1,2 and 3 in the figure). The first two observed are similar to the ones visible on $z = -250$ mm (3 and 4 on Fig. 9.9). They are emitted on the Mylar window (2) and around the first anode plane (1). The third source (3) is a diffuse background coming from the third part of the HeBox.

The detector 1 detects also two sources localized on the Mylar window and the first anode plane. On the other hand, the equivalent of the diffuse background is much weaker

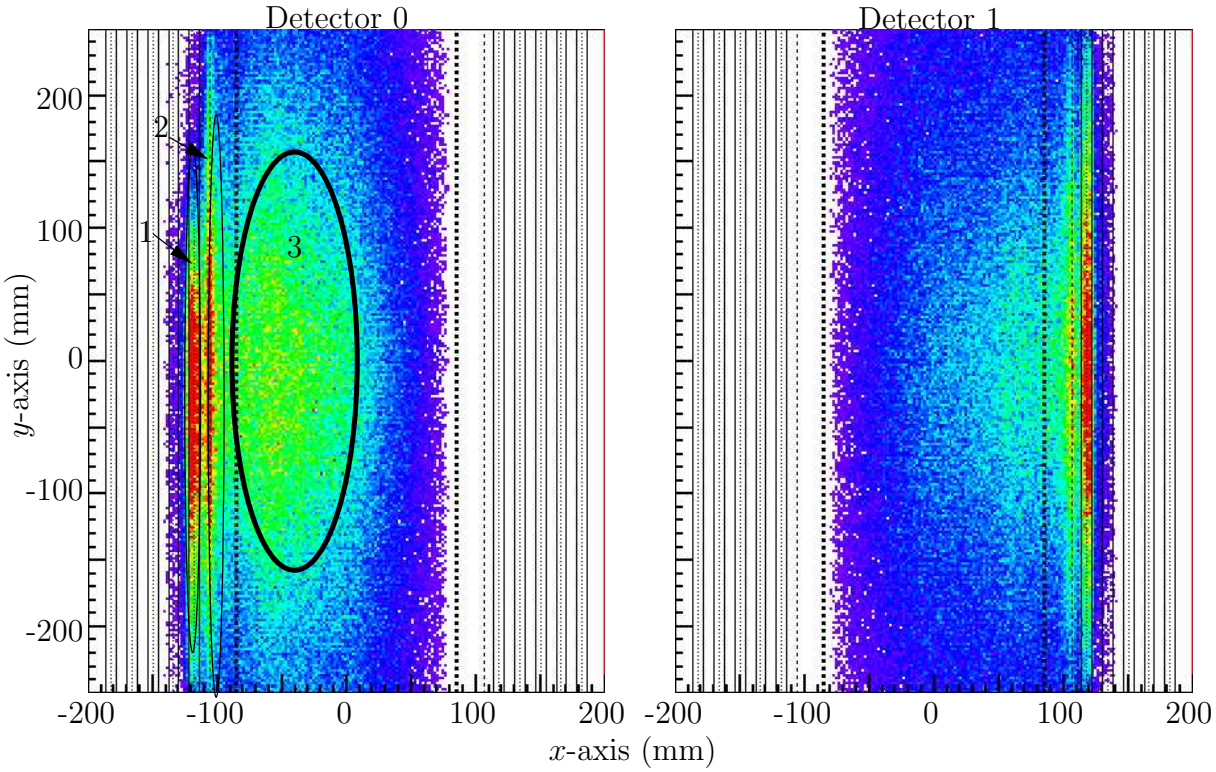

Figure 9.11: Detail of the background observed by both detectors on the plane $z = 250$. This figure was performed with $\varphi \in [40, 45]$ and the scale is the same for both detectors.

than for the detector 0.

9.1.4 Origins of these background sources

It was previously studied where these background sources are localized. The question now is to find the reason why it is emitted. A special sample of data was then selected: few hours corresponding to a beam shutdown.

9.1.4.1 Background coming from MWPC

The rates evolution of the background (E>850 keV) coming from inside the MWPCs is shown on Fig.9.12. Three contributions are visible.

The most important is directly correlated with the beam and disappear within few seconds after the beam shutdown. This background is probably due to Compton electrons emitted by γ-rays. A study of the emission angular distribution should provide some information about the origin of theses γ.

Just after the beam shutdown, an exponential decay is visible. The half-time estimation gives a value of 1050 ± 50 s. It was not possible to identify the element(s) involved in this β-decay.

After about one hour and half, the only contribution left is constant one which intensity is around 6% of the full intensity of the background coming from the opposite MWPC.

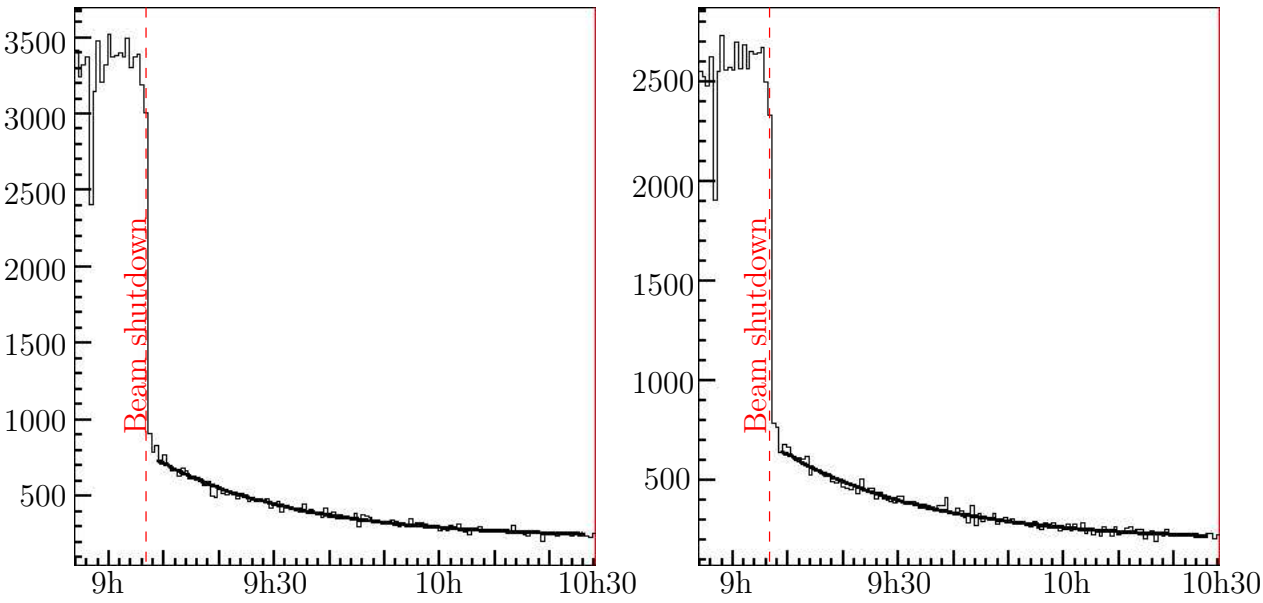

Figure 9.12: Evolution of the background rates detected by detector 0 (left) and detector 1 (right) coming from their opposite MWPC.

9.1.4.2 Background coming from Li-foils

The rates evolution of the background (E>850 keV) coming from inside the MWPCs is shown on Fig.9.13. Two contributions are visible.

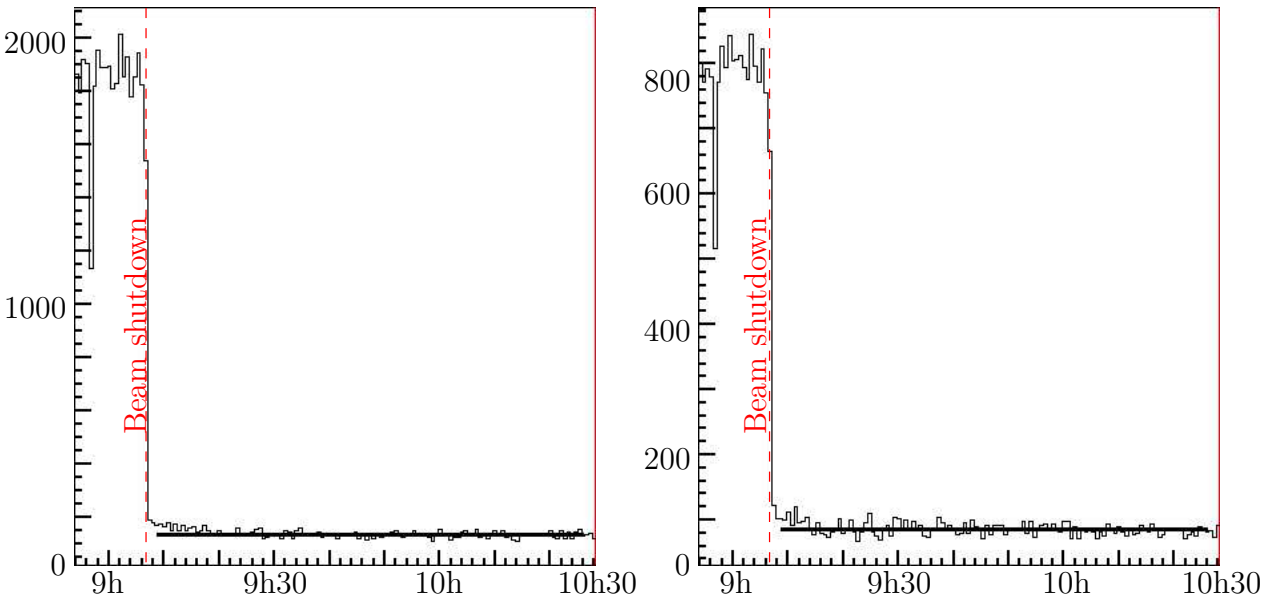

Figure 9.13: Evolution of the background rates detected by detector 0 (left) and detector 1 (right) coming from the ^{6}Li-doped polymer.

Like the background coming from the MWPC, the main contribution disappear within few seconds after the beam shutdown. Again, the most probable process is the emission of Compton electrons.

This source of background has no visible exponential decay. The constant contribution represents around 10 % of the full background emitted by this source.

9.1.5 Effect of the cuts

Amongst the cuts made by the reconstruction algorithm, two are more important for the background study: the "Stesalit Veto" and the "MWPC Veto". Both are employed as a rejection of the background emitted by the surrounding of the MWPCs, especially by their Stesalit frames.

9.1.5.1 The "MWPC Veto"

The "MWPC Veto" aims at the rejection of the tracks coming from inside the opposite chamber. In Fig. 9.14 the obvious effect of the veto on the background rejection for ST

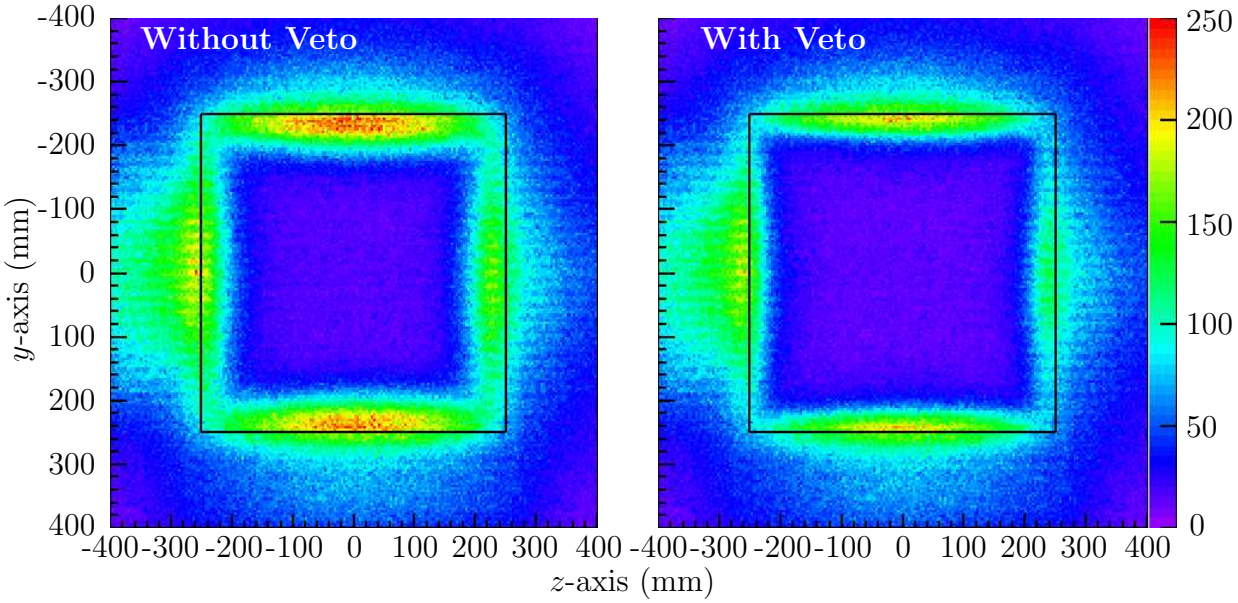

Figure 9.14: Map of the intersection between the tracks ($E > 1MeV$) detected by Det 0 and the plane $x = 85$ mm (opening of the opposite MWPC) without and with activation of the "MWPC Veto". The black square represents the limits of the MWPC window.

is visible. It is interesting to see that this veto does not reject all the background coming from the opposite chamber, because of two reasons:

- The two last wires on the side of each plane are field wires, so the chamber is inefficient there
- The distance between the side of the HeBox and the first plane of measurement is 30 mm for cathodes and 34 mm for anodes.

Therefore the veto is fully efficient only for a track coming further than $|x| = 120$ mm.

9.1.5.2 The "Stesalit Cut"

The purpose of the "Stesalit cut" is to reject the tracks potentially coming from inside of the detecting MWPC. On each projection of the track, a test is performed to see whether the trajectory crosses the frame of the MWPC. If it is the case, this event is rejected by the cut.

Its effect is a sharp cut on the side of the detector. For instance, on Fig. 9.10, it will remove all the tracks on the left of $x = -85$ mm for the detector 0 and the tracks on the right of $x = +85$ mm for the detector 1. Some of the background emitted by the areas "0-2" and "1-2" will be rejected.

This cut is particularly useful for the background rejection in the areas 3 and 4 defined in Fig. 9.1 since background and signal are completely mixed in these areas.

9.1.6 A mysterious source...

The main part of the background study was performed using few hours of measurement. However, for comparison purpose, a test with higher statistics was done. Almost by accident, a very precise source of background was discovered at the bottom of the HeBox. Visible only with very tilted tracks, this source disappeared after few days.

With the help of the tomography, this source was localized at the slit open for the manipulation of the calibration source as seen in Fig. 9.15:

- $X \in [-10; +60]$ mm
- $Y \in [-330; -260]$ mm
- $Z \in [+50; +130]$ mm

Due to its position, it is visible only for small emission angles ($\theta < 45°$) and with the detector 0[1]. This position is coherent with the calibration source stacked half-way to the parking position.

The tracks coming from this area are selected and compared to the tracks of the surrounding (Fig. 9.16(left)). After subtraction, the energy spectrum of this source can be compared with the energy spectrum of the ^{207}Bi (Fig. 9.16(right)). One can notice that this spectrum does not fully match with the one of the Bi, although they have similar shapes. It is probable that not only electrons coming from the calibration source are detected, but also electrons coming from its support, made in aluminum and stainless steel, which change the shape of the spectrum. It is also possible to see how the rates of tracks coming from this source evolved in time. The source was visible just after the calibration run (25/08/2004), and disappeared few days later (Fig. 9.17). No mention of such problem can be found in the logbooks and that nobody seems to remember it. The questions to be solved before the next run are then:

- How the source could get stack in this position ?
- How did the source reach its parking position if nobody moved it on purpose ?

[1]The source is not localized on the plane $x = 0$ and therefore it is hidden from the detector 1 by the HeBox.

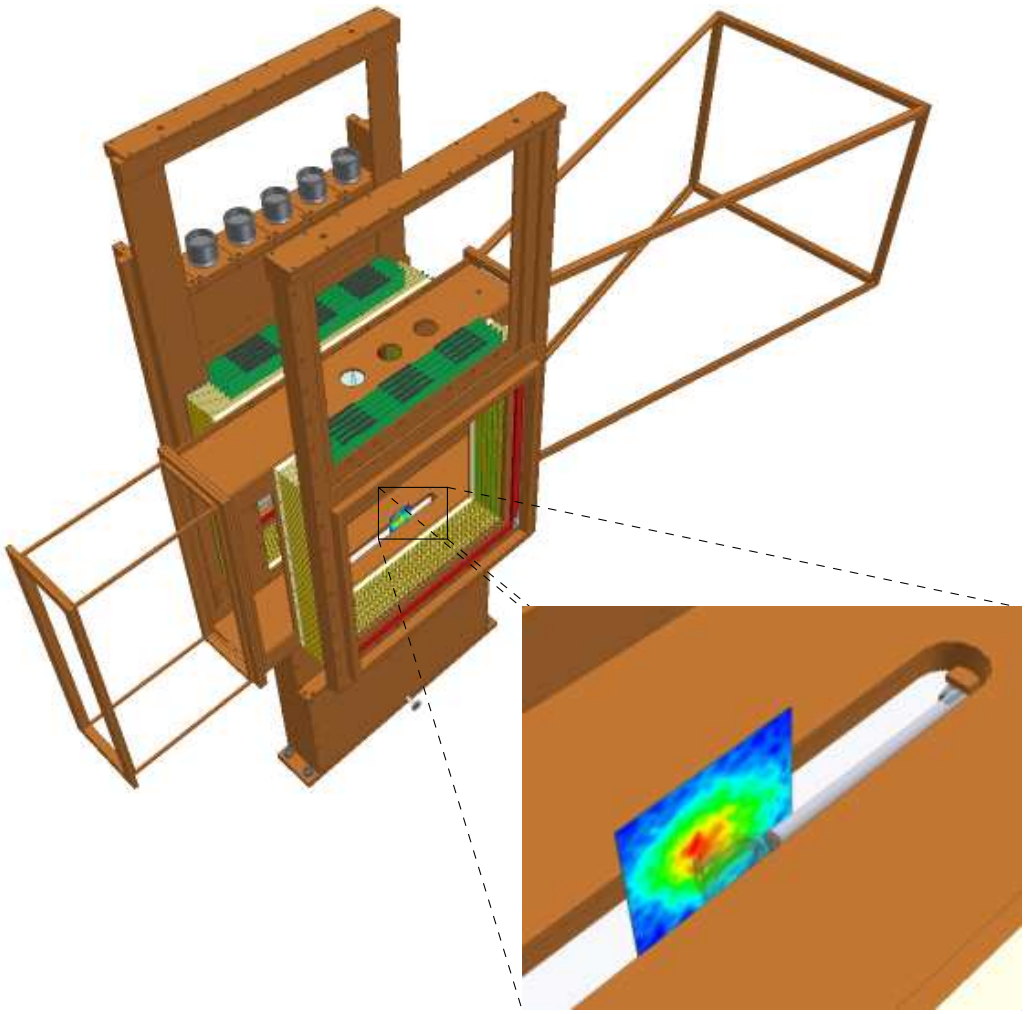

Figure 9.15: Position of the mysterious source. The hodoscope and the Pb-foil of the detector 0 are hidden.

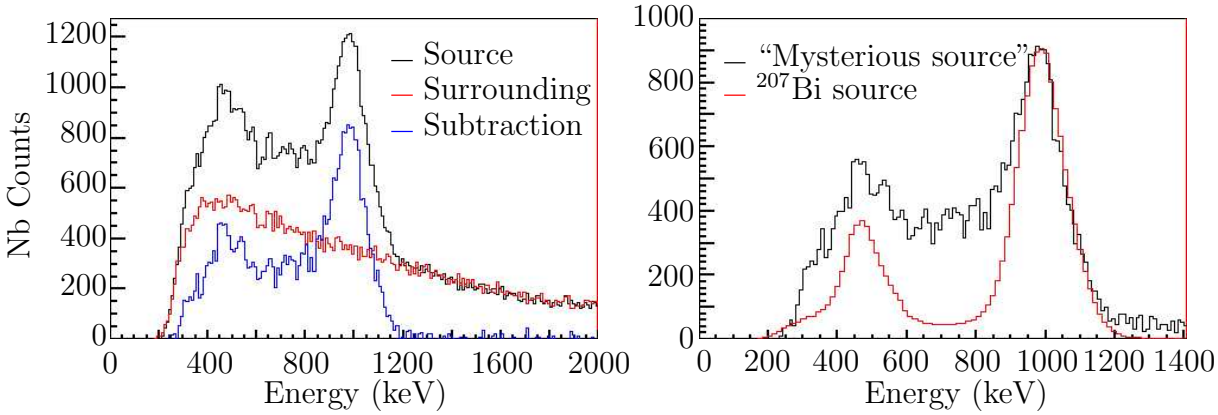

Figure 9.16: Characterization of the energy emitted by the "mysterious source". Left: Comparison between the source spectrum and the surrounding spectrum. Right: Comparison with the ^{270}Bi spectrum.

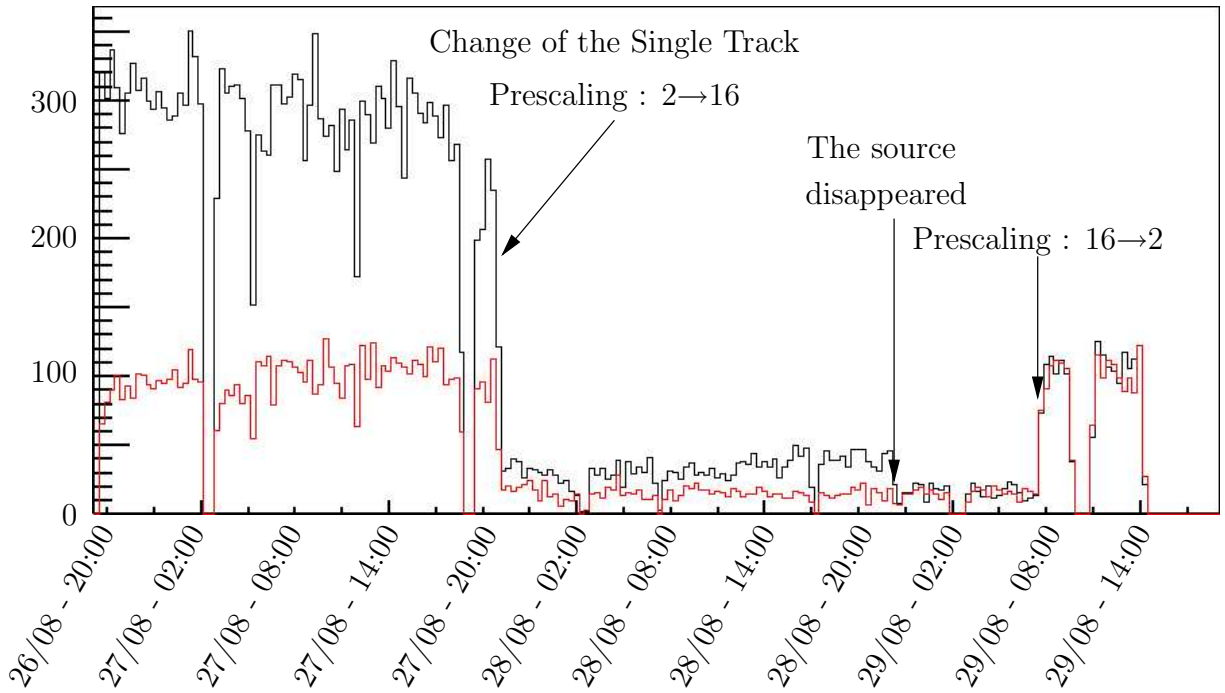

Figure 9.17: Comparison between the rate on the position of the source and a symmetric position with respect to x-axis.

The motions of the calibration are recorded into log files in the slow control system. These files will have to be checked before the next run in order to find the reason of the DMCS behavior.

9.1.7 Conclusion and suggestions for the next run

The effect of the MWPC Veto on the plane $x = 0$ mm for tracks with an energy lower than 1 MeV is shown on Fig. 9.18. Since a large part of the background is emitted from inside of the opposite chamber, the MWPC veto is very efficient for its rejection. However, this veto is limited by the position of the first wires plane. This point could be improved by a reduction of the distance between the side of the HeBox and the first plane of measurement. For instance, the alarm plane could be removed, and the first frame of the chamber could be shortened.

The pieces of ^{6}Li-polymer visible on Fig. 9.8 were placed in 2003 before the commissioning run to absorb the diverging neutrons and to prevent them to enter the MWPC. However, they produce a very disturbing background in addition to absorbing electrons coming from the beam. All in all, it seems worth to careful check their effects before the next run. If they are really useful, then it may be possible to move them farther from the chamber in order to reduce the recorded background. The best would be of course to remove them.

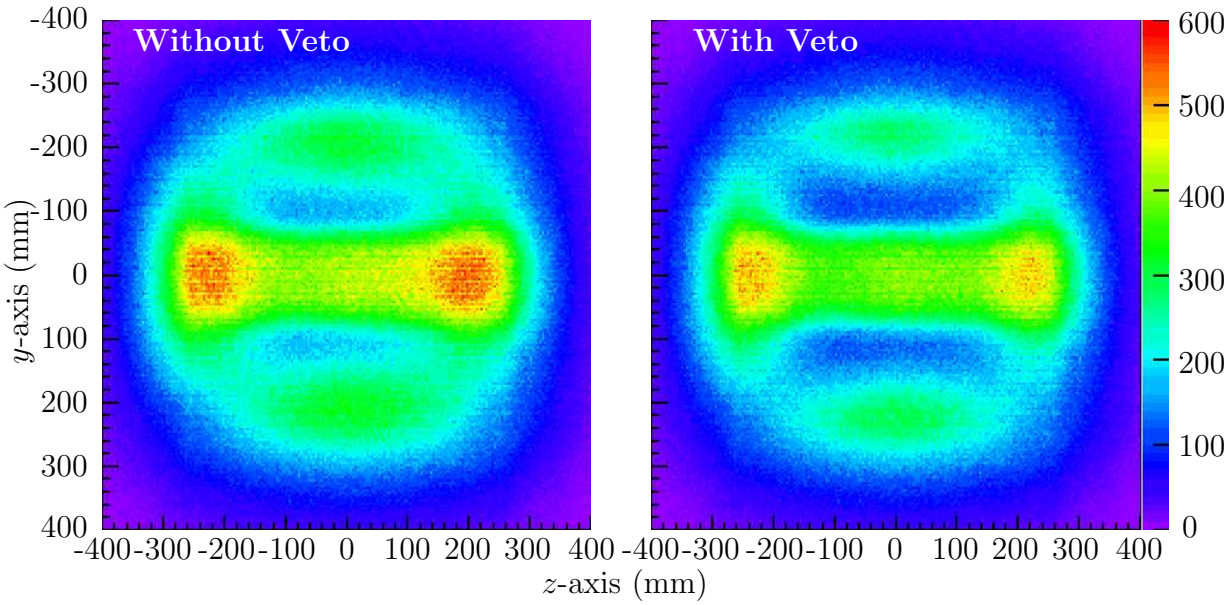

Figure 9.18: Map of the intersection between the tracks ($E < 1MeV$) detected by Det 0 and the plane $x = 0$ mm (center of the beam) without and with activation of the Veto.

9.2 Comparison with the V-Tracks

The background was studied using Single Tracks assuming that the behavior of the V-Tracks was comparable. This assumption has to be checked. Figure 9.19 shows the distribution of the tracks crossing the plane $x = 0$ mm for Single Tracks (left) and V-Tracks (right). The sample used to make the figure with ST corresponds to few hours of data taking whereas threes weeks were necessary to perform the figure with VT. The second interesting point is the respective weight of the beam and the background. For ST, the beam is very visible and its emission rate is about 30% higher than the background. For VT, the beam contribution is very weak, comparable or weaker to the contribution of the background.

The third point to be noticed is that the distribution of the background on the plane $x = 0$ seems to be different for Single Tracks and for V-Tracks.

9.2.0.1 Position of the background

Figure 9.20 shows the intersection between the plane $x = 85$ mm and both the Single Tracks detected in the detector 0 and the V-Tracks scattered by the Pb-Foil 0. The "MWPC Veto" and the "Stesalit Cut" are not applied here not to bias the investigations.

The first observation is the difference in statistics between ST and VT. Three days of data were used to provide the figure with ST whereas 2.5 weeks were necessary for VT.

The second observation is a different localization in the background emission. The Single Tracks come mainly from the inside of the opposite MWPC (top and bottom), preferentially in the middle of the chamber sides ($z \in [-200, 200]$ mm), and also from the Li foils placed as collimator. For V-Tracks, the background comes mainly from outside the chamber and mainly from the corners.

As a third point, one should notice that very few V-Tracks are coming from the middle

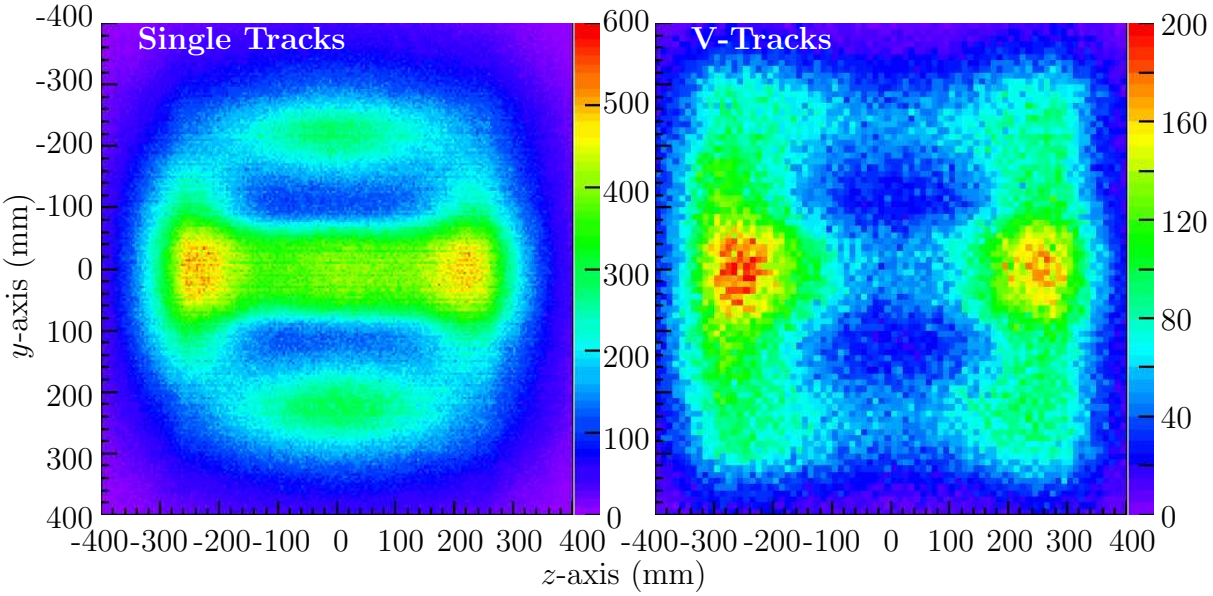

Figure 9.19: Map of emission of the Single Tracks and the V-Tracks in the plane $x = 0$ mm (Low energy). The sample used for the ST is few hours long whereas three weeks were necessary for the VT. The events used are the well reconstructed ones which energy is lower than 850 keV. The Stesalit cut and MWPC veto are applied.

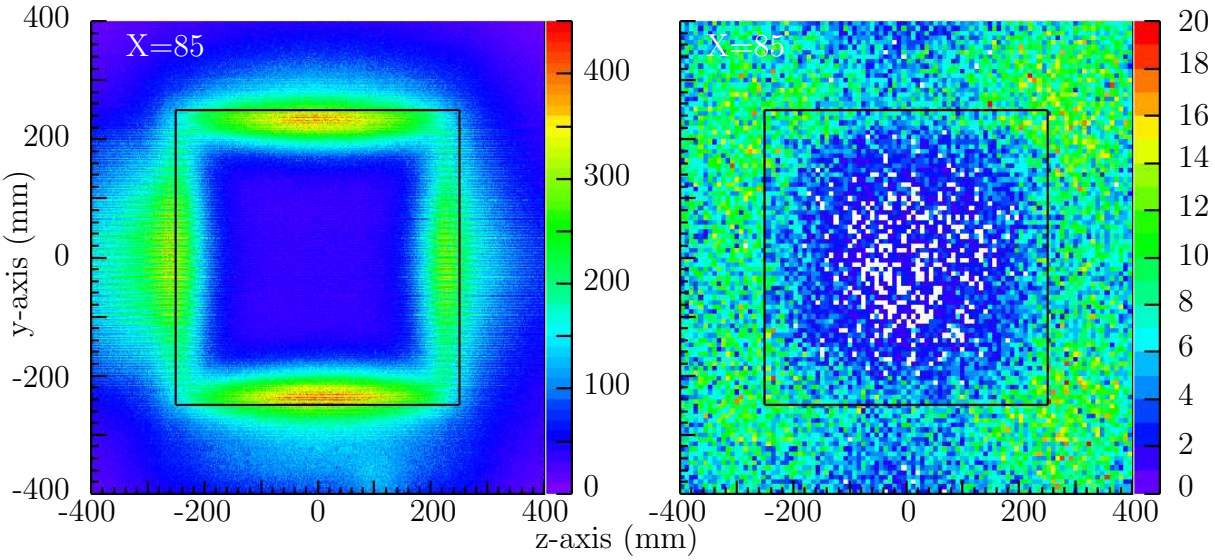

Figure 9.20: Comparison between ST (left) and VT (right) recorded by the detector 0 on the plane $x = 85$ mm ($E > 850$ keV).

of the opposite chamber.

In order to deepen the study, especially about the Li-foils, it is necessary to use the tomography method on the plane $x = 85$ mm (opposite side of the HeBox). Figure 9.21 shows the intersections of the V-Tracks with an energy higher than 850 MeV and the planes $y = \pm 250$mm and $z = \pm 250$ mm.

This figure confirms that very few V-Track come from the side of the opposite chamber

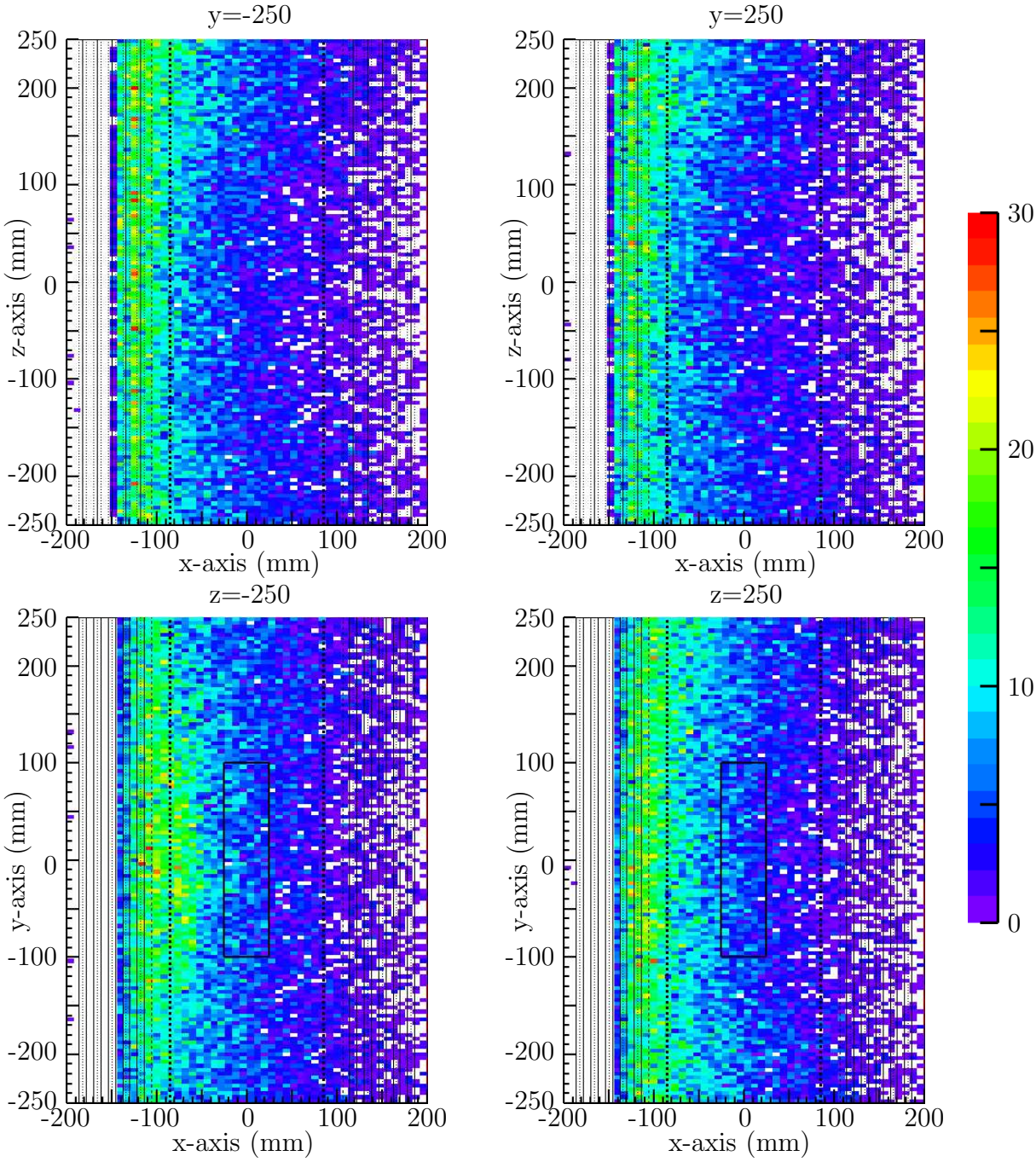

Figure 9.21: Tomography on the planes $y = \pm 250$ mm and the planes $z = \pm 250$ mm with V-Tracks ($E > 850$ MeV).

despite the absence of Veto. The major part of the VT visible on these planes of projection are coming from inside the MWPC on the side of the detection and will be rejected by the Stesalit Cut.

The intersection between the VT and the plane $z = -250$ mm shows the contribution of the Li-foils to the background. However, one can notice that this contribution is very weak.

9.3 Acceptance and Mott scattering cross-section effects

The use of Single Tracks for the background study was mainly chosen because of the very high statistic, compared to the V-Tracks. It was assumed that the source of background for both kinds of events were the same. However, the previous observations weaken this assumptions.

It is known that the scattering modifies the acceptance of the events with respect to the solid angle of the detector: the larger the scattering angle, the weaker the cross-section. Additionally, the detection/reconstruction of very scattered electrons is not possible with our setup and this effect can have a large influence on how the VTracks are detected and reconstructed.

In order to evaluate if these effects can explain the differences observed before, a rough simulation was performed, using a basic C++ code and randomized emission and scattering. No physical effect was taken into account, and the electron trajectories were linear.

9.3.1 Simulation of the background emission

For a given energy, electrons are emitted randomly in three background sources: i) the opposite side of the HeBox, ii) the inside of the opposite MWPC and iii) the piece of ^{6}Li-polymer situated in front of the detector. The relative intensity of the sources are arbitrary chosen. The purpose is to compare qualitatively the behavior of the Single Tracks and the V-Tracks.

For all the sources, the emission direction is randomly drawn in the 2π steradians covering the half-space where the "hodoscope" (ST) or the "Pb-foil" (VT) is located.

9.3.1.1 The opposite side of the HeBox (Bckgd1)

This area follows the geometry of the HeBox: the electrons are emitted *around* the window of the opposite MWPC.

- $x = -85$
- $y \in [-500, -250] \bigcup [250, 500]$ mm
- $z \in [-500, -250] \bigcup [250, 500]$ mm

9.3.1.2 Inside the opposite MWPC (Bckgd2)

This source simulates the sources discovered in the area 1 and 2 (Fig. 9.1). The electrons are emitted in

- $x \in [-185, 85]$ mm
- $y = \pm 250$ mm (top and bottom)
- $z \in [-250, 250]$ mm

9.3.1.3 The piece of ^{6}Li polymer (Bckgd3)

This source simulates the emission of electron from the pieces of ^{6}Li polymer (called Li0 and Li1 in the paragraph 9.1.3). Therefore the coordinates of emission are

- $x \in [-85; -50]$ mm and $x \in [50; 85]$ mm (both pieces of Li are simulated)
- $y \in [-130, 130]$ mm
- $z = -250$ mm

9.3.2 Trajectories and detection

During the simulation, only geometrical limits are accounted for. To be detected, a track has to stay inside the limits of the detector. The positions of the tests are visible on Fig. 9.22.

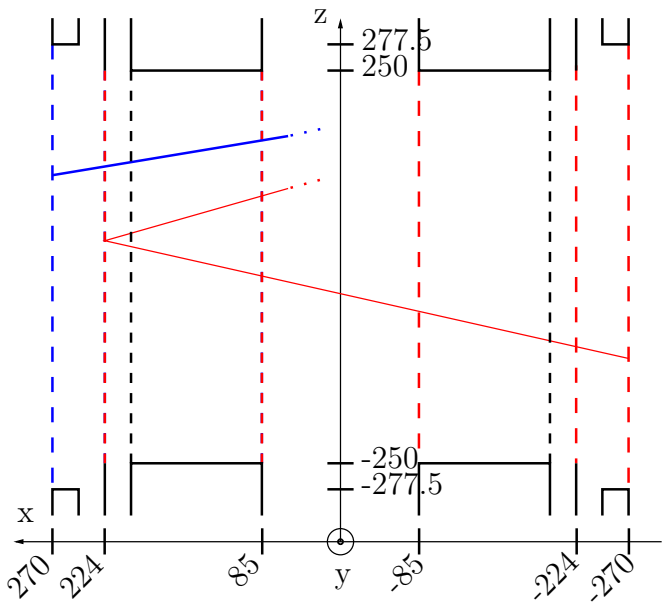

Figure 9.22: Position of the acceptance tests for the Single Tracks (blue) and for the V-Tracks (red).

When VT are simulated, all the tracks reaching the Pb-foil are assumed to be scattered with an angle higher than 60°: the purpose is to compare the relative behavior between the positions of emission and thus all the electrons are back-scattered. The angular distribution of δ (Fig.8.1) is then chosen in order to account for i) the scattering cross section distribution and ii) the difficulties of NPRun to reconstruct V-Track highly scattered (sensitive from $\delta > 120°$). The angle α is chosen randomly.

9.3.3 Results

In order to compare the simulation with the real data, the observation are made on the plane $x = 0$. The intersection between the detected tracks of each sources and this plane is visible on Fig. 9.23.

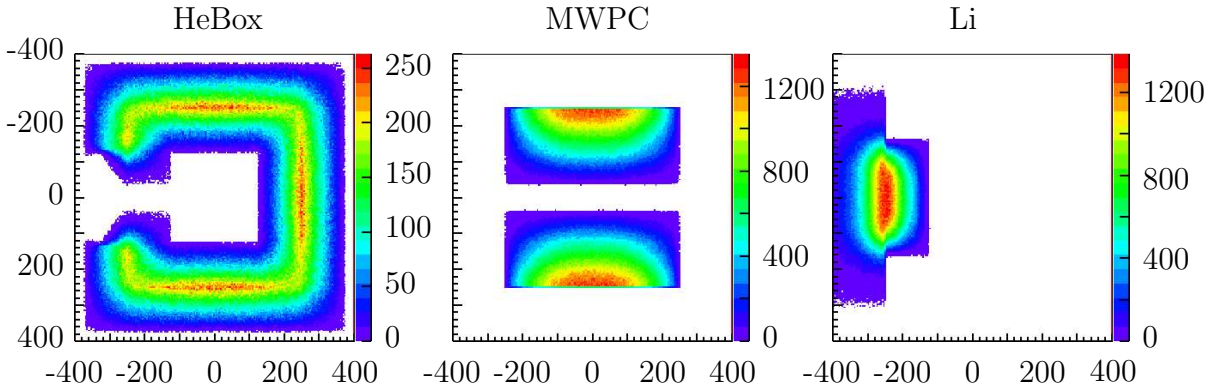

Figure 9.23: Contribution of the three background sources.

The first step is to find a ratio between the different contribution of Single Tracks providing a similar background distribution as the real data on the plane $x = 0$ (Fig. 9.24).

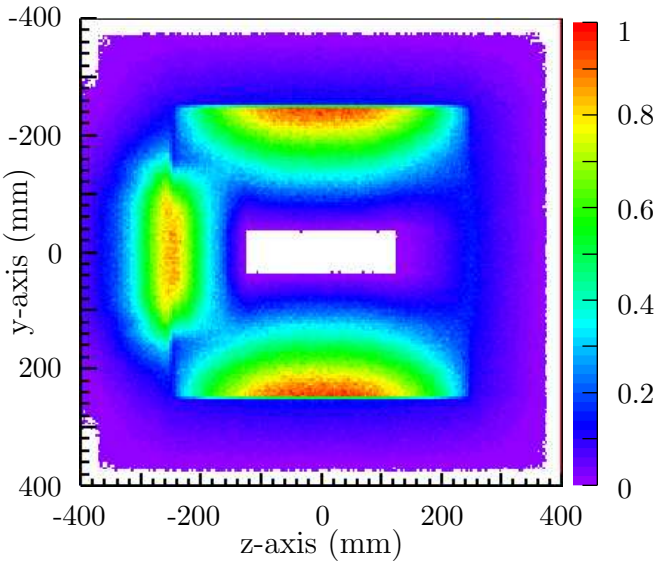

Figure 9.24: Distribution of the intersection between the plane $x = 0$ and the Single Tracks coming from the background source.

These sources are then used to simulate V-Tracks of 1 MeV. The distribution of the recorded tracks on $x = 0$ is shown on Fig. 9.25. According to the simulation, the contribution of the Li foils dominates the other background sources. This is easy to understand since these events are coming on the Pb-foil with a large angle of incidence and the source is close to the foil. They will have a higher probability to be scattered toward the other detector than the events coming from anywhere else in the setup. The second strongest contribution comes from the side of the opposite MWPC and the weakest is provided by the surrounding of the MWPC. The difference is mainly due to their respective weight set before with ST.

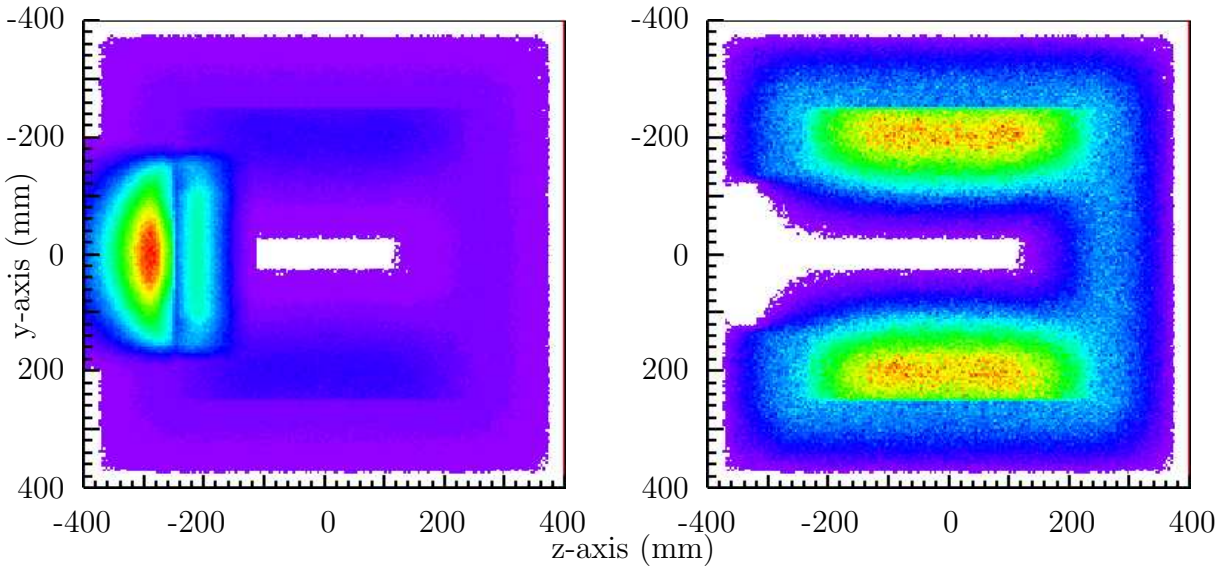

Figure 9.25: Distribution of the intersection between the plane $x = 0$ and the V-Tracks coming from the background source. Left: with the Li collimator contribution. Right: without.

9.3.4 Simulation of the beam

A simulation of the beam is now performed. It is defined by $(x, y, z) \in [-30, 30] \times [-100, 100] \times [-400, 400]$. The position of emission is randomly chosen in this volume. Again, the electrons are emitted in the half-space spanned by the detector and the Pb-foil. The distribution of the recorded tracks on the plane $x = 0$ for ST and VT is shown on Fig. 9.26.

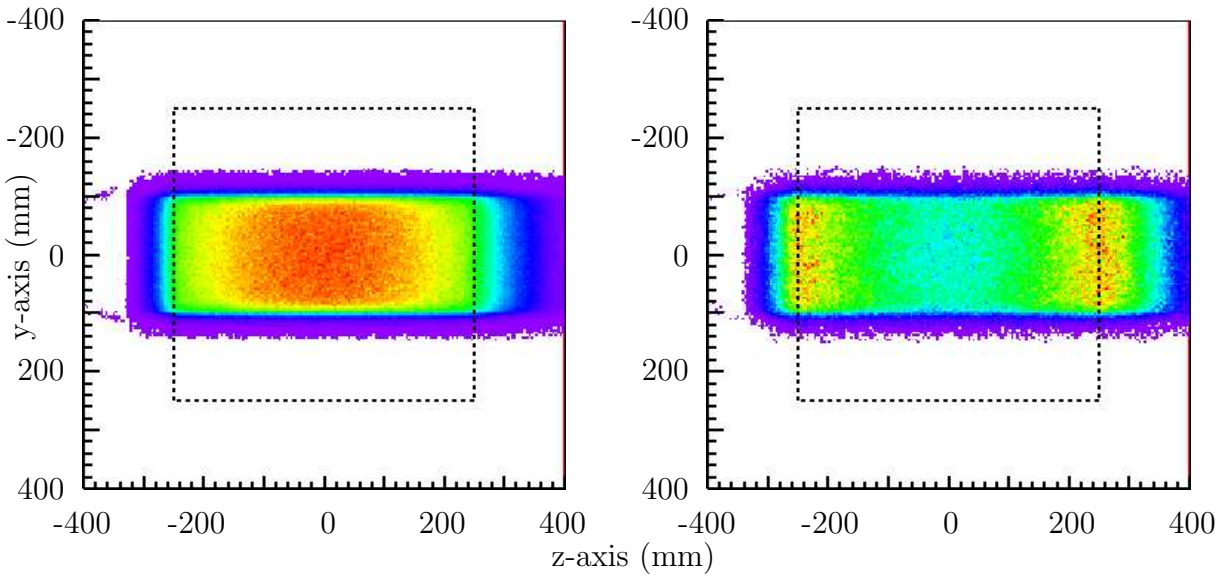

Figure 9.26: Distribution of the intersection between the plane $x = 0$ the events coming from the beam. Left: Single Tracks. Right: V-Tracks

For both figures, it is possible to see that the events are not symmetrically recorded

along the z-axis: the simulation removes the tracks crossing the Li collimator localized on $z = -250$.

For Single Tracks, more events are recorded around the middle of the detector whereas for V-Tracks most events are coming from the side. One can even notice that the middle is depleted. It is the combined effect of the scattering cross section (lower for higher scattering angle) and the difficulties of close tracks reconstruction. Due to the geometry of the beam, this effect is more sensitive with horizontal V-Tracks than with vertical ones.

9.3.5 Conclusion

The information provided by this simulation are mixed. On one hand, they provide an explanation of the deficit of V-Tracks coming from the middle of the detector; due to the difficulties of reconstruction of close Tracks together with the influence of the scattering cross section. On the other hand, they do not explain why the distribution of the background is so much different between Single Tracks and V-Tracks in the real data.

Because of geometry of the beam and of the V-Track depletion in the middle of the detector, the majority of the recorded events are rather horizontal whereas the most interesting events are the vertical ones. This point is intrinsic to the detector design and cannot be improved without major modification.

Chapter 10

Conclusion and Outlook

In the introduction, we have shown the importance of a precise determination of the neutron β-decay correlation coefficients as a probe of the Standard Model parameters. The experiment described in this document aims at the simultaneous measurement of both R and N parameters, defined by Jackson *et al.* for the β-decay of free neutrons. A not zero value of R would mean a Time reversal conservation violation and thus a physic beyond the Standard Model. The measurement of N is a test of the detector sensitivity.

We have then explained the methods used to measure the observables required for the determination of these parameters:

- The neutron polarization
- The electron momentum
- The electron transverse polarization components

The neutron polarization is determined by the measurement of the emission anisotropy with respect to the direction of the neutron polarization (A-correlation). Two detectors are requested to measure the electron momenta. A tracking detector provides the direction or emission and a scintillator gives the energy. The electron transverse polarization component is determined by the use of a Mott polarimeter.

This document provides an overview of the neutron beam line, FUNSPIN, followed by a detailed description of the experimental setup. The polarization of the beam is in average slightly lower than 90%. The neutrons are flying in an He-filled volume and decay in-flight. The tracking detectors consist of two MultiWire Proportional Chambers placed on both side of the beam. They provide information about the track projections on two perpendicular planes. The Mott scatterers are 2.5 μm Mylar foils covered by a 1 μm thick layer of lead. The scintillators are 1 cm thick plastic slabs with a light guide and a photomultiplier at each end.

In this document were explored several possibilities to evaluate the parameters R and N from the events recorded and well reconstructed. Three asymmetries can be built, depending if we consider the neutron spin states and/or the electron scattering direction. Two method of integration were proposed. One divides the experimental setup in a succession of small detectors, and the second considers the detector as a whole. The main difference resides in the management of the detector efficiency. Two aspects are missing in this study. Firstly, the influence of the errors are not evaluated; secondly these methods

were not tested with real data. Therefore, it is not possible to decide now which way is the best to calculate the parameters R and N

A tomography-like method was proposed to localize the electron sources. It was mainly used with Single Tracks to find the background sources in the experimental setup. Some improvements were proposed to decrease the amount of background for the next data taking scheduled in summer 2006. A similar study with V-Tracks showed background sources differently distributed. The simulations performed to find explanations did not provide satisfactory results.

After few months analyzing the data from 2004, I acquired the conviction that the background was not enough under control to trust the background substraction procedures. Therefore, I chose to leave the calculation of the parameters on side and concentrated on the background study. One of the consequences was the discovery of unexpected sources like the ^{6}Li-doped polymer placed as a collimator just before the MultiWire Proportional Chambers. In addition, we determined that the main part of the background was coming from inside the chambers rather than the side of the HeBox as expected. A large part of this background is rejected by the reconstruction algorithm but the remaining is not negligible. Before the next run, efforts must be made to reduce the amount of background emitted, and to increase the efficiency of the veto.

A welcome improvement would be a best reconstruction of V-Tracks with large scattering angle ($\delta > 120$). The statistics, especially for V-Tracks going up and down, would increase. Moreover, these events have the best analyzing power. Unfortunately, this seems difficult to achieve since the problem is not only due to the reconstruction algorithm but also a consequence of the detector geometry. The first point should be to improve the stability of the gas detector, especially by the replacement of the flow-meters by flow-controllers.

List of Figures

Bibliography

[1] T.D. Lee and C. N. Yang. *Phys. Rev.*, 104:254, 1956.

[2] P. Forman. *The Fall of Parity*. The Physics Teacher, 1982.

[3] C.S. Wu, E. Ambler, R.W. Hayward, D.D. Hoppes, and R.P. Hudson. *Phys. Rev.*, 105:1415, 1957.

[4] J.D. Jackson, S.B. Treiman, and H.W. Wyld. *Nucl. Phys.*, 4:206, 1957.

[5] J.H. Christenson, J.W. Cronin, V.L. Fitch, and R. Turlay. *Phys. Rev. Lett.*, 13:138, 1964.

[6] S.L. Glashow, A. Salam, and S. Weinberg. *Nobel Lectures, Physics 1971-1980*. World Scientific Publishing Co., Singapore, 1992.

[7] B.Aubert and et al. (BaBar Collaboration). *Phys. Rev. Lett.*, 87:091801, 2001.

[8] K. Abe and et al. (Belle Collaboration). *Phys. Rev. Lett.*, 87:091802, 2001.

[9] A.D. Sakharov. *JETP Lett.*, 5:24, 1967.

[10] N. Cabibbo. *Phys. Rev. Lett.*, 10:531, 1963.

[11] M. Kobayashi and K. Maskawa. *JETP Lett.*, 5:24, 1967.

[12] G. 't Hooft. *Phys. Rev. Lett.*, 37:8, 1976.

[13] L. Wolfenstein. *Phys. Rev. Lett.*, 13:562, 1964.

[14] R.N. Mohapatra and J.C. Pati. *Phys. Rev. D*, 11:56, 1975.

[15] J.D. Jackson, S.B. Treiman, and H.W. Wyld. *Phys. Rev.*, 106:517, 1957.

[16] L.J. Lising, S.R. Hwang, and et al. *Phys. Rev. C*, 62:055501, 2000.

[17] T. Soldner, L. Beck, C. Plonka, K. Schrekenbach, and O. Zimmer. *Phys. Lett. B*, 581:49, 2004.

[18] M. E. Ebel and G. Feldman. *Nucl. Phys.*, 4:213, 1957.

[19] Particle data group.

[20] R. Huber, K. Bodek, W. Haeberli, St. Kistryn, J. Lang, S. Navert, O. Naviliat-Cuncic, J. Sromicki, E. Stephan, and J. Zejma. *Phys. Rev. Lett.*, 90:202301, 2003.

[21] M.B. Schneider, F.P. Calaprice, A.L. Hallin, D.W. MacArthur, and D.F. Schreiber. *Phys. Rev. Lett.*, 51:1239, 1993.

[22] E.G. Adelberger, C. Ortiz, A. García, H.E. Swanson, M. Beck, O. Tengblad, M.J.G. Borge, and I. Martel. *Phys. Rev. Lett.*, 83:1299, 1999.

[23] A.P. Serebrov, A.V. Aldushchenkov, M.S. Lasakov, I.A. Kuznetsov, and I.V. Stepenko. *Nucl. Instr. Meth. A*, 357:503, 1995.

[24] G. Ban, M. Beck, A. Białek, K. Bodek, P. Gorel, K. Kirch, St. Kistryn, A., Kozela, M. Kuźniak, A. Lindroth, O. Naviliat-Cuncic, J. Pulut, N. Severijns, E.Stephan, and J. Zejma. *Nucl. Instr. Meth. A: to be published.*

[25] N.F. Mott. *Proc. Roy. Soc. A*, 124:424, 1929.

[26] C.G. Shull, C.T. Chase, and F.E. Myers. *Phys. Rev.*, 63:29, 1942.

[27] N.F. Mott. *Proc. Roy. Soc. A*, 135:429, 1932.

[28] N. Sherman. *Phys. Rev.*, 103:1601, 1956.

[29] F.B. Dunning and T.J. Gay. 63:1635, 1992.

[30] L.H. Thomas. *Nature*, 117:514, 1926.

[31] J. Kessler. *Polarized electrons.* Springer-Verlag, Berlin, 1976.

[32] J. Sromicki. *Nucl. Instr. Meth. A*, 440:609, 2000.

[33] D. Conti. *Feasability Study to measure Time reversal Invariance in Polarized Neutron Decay.* PhD thesis, ETH Zurich, 1999.

[34] C. Hilbes. *Towards an Experimental Test of Time Reversal Invariance violation in the decay of Polarized Free Neutrons.* PhD thesis, ETH Zurich, 2002.

[35] *SINQ Webpage.* http://asq.web.psi.ch/ASQ/facilities/SINQSYSTEMS.html.

[36] A. Schebetov, A. Serebrov, V.M. Pusenkov, M.S. Lasakov, P.Böni, M. Lüthy, and J. Sromicki. *Nucl. Instr. Meth. A*, 497:479, 2003.

[37] A.N. Bazhenov, V.M. Lobashev, A.N. Pirozhkov, and V.N. Slusar. *Nucl. Instr. Meth. A*, 3:354, 1993.

[38] *Ingenieurbüro Stronciwilk.* http://stronciwilk.de/.

[39] J. Zejma, G. Ban, M. Beck, A. Białek, K. Bodek, G. Frei, Ch. Hilbes, G. Kügne, P. Gorel, K. Kirch, St. Kistryn, A., Kozela, M. Kuźniak, A. Lindroth, O. Naviliat-Cuncic, J. Pulut, N. Severijns, and E.Stephan. *Nucl. Instr. Meth. A*, 539:622, 2005.

[40] K. Bodek, T. Boehm, D. Conti, N. Danneberg, W. Fetscher, C. Hilbes, M. Janousch, S. Kistryn, K. Köhler, J. Lang, M. Markiewicz, and J. Sromicki. *Nucl. Instr. Meth. A*, 473:326, 2001.

[41] H. M. Neumann and I. Perlman. *Phys. Rev.*, 81:958, 1951.

[42] A. Białek. *Transversal polarisation of electrons emitted in the decay of free neutrons.* PhD thesis, Jagellonian University Krakow, To be defended.

[43] *PSI archive Sytem.* https://archiv.web.psi.ch/docu.php.

[44] *Root: An Oriented-Object Data Analysis Framework.* http://root.cern.ch.

Résumé

Le sujet de ce cette thèse est la mise en oeuvre d'un dispositif expérimental permettant la mesure des paramètres R et N dans la désintégration du neutron polarisé, ainsi que l'analyse des données récoltées. Quatre observables sont nécessaires à cette mesure : la polarisation des neutrons, l'impulsion des électrons et les deux composantes transversales de la polarisation des électrons. Ces deux dernières observables sont mesurées au moyen d'un polarimètre de Mott. Les mêmes détecteurs permettent également de déterminer les autres observables. La précision recherchée sur le paramètre R est de 0,5%. Une valeur non nulle serait la marque d'une violation de la symétrie sous le renversement du temps, non prévue par le Modèle Standard. Ce document décrit dans un premier temps le travail effectué pour préparer et optimiser le dispositif expérimental avant la campagne de mesure qui s'est déroulée à l'été 2004. En particulier, un effort important a été fourni pour améliorer le fonctionnement des murs de scintillateurs utilisés à la fois pour déclencher l'acquisition et pour mesurer l'énergie des électrons. La deuxième partie concerne la mise au point d'une méthode d'extraction des paramètres R et N à partir des données récoltées, et l'étude de l'origine du bruit de fond mesuré simultanément.

Mots-clés

Interactions Faibles (Physique Nucléaire), Symétries Brisées (Physique), Désintégration Beta, Neutrons ** Polarisation.

Abstract

The topic of this thesis is the implementation of an experimental setup designed to measure the R- and N-parameters in polarized neutron decay, together with the data analysis. Four observables are necessary for this measurement: the neutron polarization, the electron momentum and both transverse components of the electron polarization. These last two are measured using a Mott polarimeter. The other observables are determined using the same detectors. The precision to be reached on the R-parameter is 0.5%. A non zero value would sign a time reversal invariance violation and therefore would be a hint of physics beyond the Standard Model. This document firstly presents the work done to prepare and optimize the experimental setup before the data acquisition run performed in 2004. Particular care was taken on the scintillator walls, used to trigger the acquisition and measure the electron energy. The second part concerns the implementation of methods to extract R and N from the data, and the study of the background recorded simultaneously.

Key-words

Weak Interactions (Nuclear Physics), Broken Symmetries (Physics), Beta decay, Neutrons ** Polarization.

Discipline : Physique Nucléaire

Laboratoire de Physique corpusculaire
6, boulevard du Maréchal Juin
14050 Caen CEDEX